Internal and external dynamics of a strongly-coupled atom-cavity system

Dissertation
zur Erlangung des Doktorgrades (Dr. rer. nat.)
der Mathematisch-Naturwissenschaftlichen Fakultät
der Rheinischen Friedrich-Wilhelms-Universität Bonn

vorgelegt von
Sebastian Reick
aus
Geldern

Bonn 2009

Angefertigt mit Genehmigung
der Mathematisch-Naturwissenschaftlichen Fakultät
der Rheinischen Friedrich-Wilhelms-Universität Bonn

1. Gutachter: Prof. Dr. Dieter Meschede
2. Gutachter: Prof. Dr. Martin Weitz

Tag der Promotion: 16. Dezember 2009

Diese Dissertation ist auf dem Hochschulschriftenserver der ULB Bonn
`http://hss.ulb.uni-bonn.de/diss_online/` elektronisch publiziert

Erscheinungsjahr: 2010

Abstract

A system comprised of a small number of neutral atoms coupled to the mode of a high finesse optical resonator is a model system to study light-matter interaction at the quantum level and to explore fundamental effects like the influence of the measurement process on the atomic state. Promising proposals to generate entangled states in such systems are based on the simultaneous coupling of two atoms to one resonator mode.

In chapter 1 of this thesis I shortly summarise the experimental tools to capture, trap, and transport single atoms using a magneto-optical trap and an optical conveyor belt. I discuss theoretical foundations to describe our system and present numerical simulations, the results of which enter the analysis of our experimental data. The average atom-cavity coupling strength is deduced from the measured cavity transmission and compared to a model taking atomic motion into account.

The dynamics of the hyperfine spin state of one and two coupled atoms is the focus of chapter 2. I describe a nondestructive cavity-based state detection method, quantify the state detection fidelity, and identify optimum experimental parameters. This method is then used to record random telegraph signals, exhibiting quantum jumps on a timescale of milliseconds. Telegraph signals for two atoms are analysed employing Bayesian statistics, yielding additional information on the evolution of the hyperfine states.

A good localisation of the atom is necessary to achieve stable coupling to the cavity mode. In chapter 3, I discuss two different aspects of how the motion of the atom can be controlled. Firstly an intracavity dipole trap is characterised and it is shown that it results in improved confinement of the atom. Secondly I examine the dependence of cavity-cooling forces on our experimental parameters and compare two different cooling regimes.

Zusammenfassung

Einige wenige Atome, die an das Feld eines optischen Resonators hoher Finesse gekoppelt sind, stellen ein Modellsystem zur Untersuchung von fundamentalen Prozessen der Licht-Materie-Wechselwirkung dar, wie etwa die Rückwirkung des quantenmechanischen Messprozesses auf den atomaren Zustand. Vielversprechende Vorschläge zur Erzeugung von verschränkten Zuständen in solchen Atom-Resonator-Systemen basieren auf der simultanen Wechselwirkung zweier Atome mit dem Resonatorfeld.

Im ersten Kapitel dieser Arbeit fasse ich die wesentlichen Komponenten des experimentellen Aufbaus zusammen. Theoretische Grundlagen zur Beschreibung

des Systems werden diskutiert, sowie darauf aufbauende numerische Simulationen, deren Ergebnisse in spätere Auswertungen von Messergebnissen eingehen. Den Abschluss des Kapitels bildet eine Bestimmung der mittleren Atom-Resonator-Kopplungsstärke und deren Vergleich mit einem theoretischen Modell, welches die atomare Bewegung berücksichtigt.

Die Dynamik der internen Hyperfein-Spinzustände bildet den Schwerpunkt des zweiten Kapitels. Eine nicht-destruktive Methode zur Messung des Spins mit Hilfe der Cavity wird vorgestellt und charakterisiert; dabei werden optimale experimentelle Parameter identifiziert. Mit Hilfe dieser Methode wurden sog. Telegraphen-Signale aufgenommen, bei denen Quantensprünge auf der Zeitskala einiger Millisekunden beobachtet werden können. Im Falle zweier Atome werden derartige Signale zusätzlich mittels Bayes'scher Statistik analysiert um Informationen über die zeitliche Entwicklung der Spinzustände zu erhalten.

Eine wichtige Voraussetzung für stabile Atom-Resonator-Kopplung ist eine gute Lokalisierung der Atome. Im dritten Kapitel werden zwei Phänomene diskutiert welche die Bewegung der Atome beeinflussen. Zum einen wird gezeigt, wie eine innerhalb des Resonators gebildete zusätzliche Dipolfalle zu einer verbesserten Lokalisierung führt. Des Weiteren wird theoretisch und experimentell untersucht, wie Kühleffekte, die ausschließlich auf der Atom-Resonator-Wechselwirkung basieren, von der Wahl der experimentellen Parameter abhängen.

Contents

Introduction

Since the development of quantum mechanics one century ago, studying quantum physical effects on the single particle level has made the transition from thought experiments to setups in real world laboratories. In this context, small model systems comprised of only a few constituents have always been of special interest for testing and illustrating fundamental quantum-physical concepts.

The elementary system of light-matter interaction consists of a single atom interacting with a single excitation of a mode of the electro-magnetic field, as described by quantum electrodynamics (QED). In free space, the experimental realisation of this system is hardly possible due to the small cross section, but this obstacle can be overcome by confining the light field to a cavity. The interaction of one atom coupled to a single quantised mode of a cavity is one of the building blocks of cavity-QED (CQED) and was investigated theoretically by Jaynes and Cummings in 1963 [1]. In this closed system, energy is coherently exchanged without losses between atom and light field at a rate usually called the coupling strength.

A realistic and more complete picture includes coupling to the environment by two decay channels, namely light leaking out of the cavity and spontaneous emission by the atom. This open quantum system, as discussed in [2], does not only add decoherence, but losses are a necessary means for any observer to study the processes which would otherwise be completely hidden in a perfectly closed system. If the coherent evolution dominates over the aforementioned decay channels, the system is in the so called *strong coupling regime*.

Experimentally, it took several decades of technological advances to realise the conceptually simple arrangement of a single atom and a cavity in the laboratory, because three objectives have to be met: Firstly a single atom has to be cooled and trapped, which became possible with the advent of laser cooling [3]. Secondly, cavities of sufficiently high quality factors had to be manufactured, which was first achieved in the microwave regime [4, 5] and later in the optical regime using miniaturized cavities [6]. Thirdly, one or a small number of atoms has to be inserted into the cavity in a controlled way.

This third aspect is vital for performing deterministic experiments. In the microwave experiments, a stream of Rydberg atoms traverses the cavity, and also the first experiments in the optical domain were performed with an atomic beam [7–9] where one atom was present in the mode volume, but only on average

and for a short time. Two similar techniques were used to trap a *single* atom inside the cavity, namely letting atoms fall from a magneto-optical trap [10] or ejecting them from below the cavity by means of an atomic fountain [11] and capturing them inside the cavity. Exact positioning, however, was realised in our and other research groups using an optical conveyor belt to transport atoms from a trapping region into the cavity [12–14].

A special advantage of the setup developed in our group is that this controlled coupling has been extended to the case of two or more atoms [15], thereby paving the way to experiments studying the simultaneous interaction of a small ensemble of atoms coupled to the same cavity mode. This photon-mediated interaction is the basis for promising proposals to generate entangled states in CQED systems [16–18].

In order to plan and perform such experiments, the properties of the experimental setup and its limitations have to be explored and quantified. This is the focus of this thesis, in which I studied both the internal and external dynamics of one and two caesium atoms coupled to an optical cavity in the strong coupling regime. Caesium, as an alkali atom, has two stable hyperfine ground states, which would be the two qubit states acted on in entanglement generation. Thus it is important to understand why and to which degree these states are influenced by our measurements, and the evolution of these spin states is what I refer to as internal dynamics.

In the strong coupling regime, already a single atom can shift the cavity resonance such that an initially resonant laser is no longer transmitted. Since this shift depends on the hyperfine state, it facilitates a nondestructive state detection technique [19]. It was used in this thesis to observe quantum jumps between hyperfine states for one and two atoms, a phenomenon observed for the fluorescence in trapped ions [20–22] but not yet for neutral atoms.

For all experiments we plan to pursue in our group, a stable strong coupling between atom and cavity mode is important. My analysis of our measurement data shows a considerable variation of the coupling strength, leading to an effectively lower value than theoretically predicted. This variation is mainly attributed to thermal motion. Therefore I investigated two approaches to reduce the external dynamics, firstly by trapping the atom using an intracavity dipole potential [23] and secondly by employing "cavity cooling" [24], where the dissipative role of spontaneous emission in free space Doppler cooling is replaced by the photons emitted from the cavity having a higher energy than the incoming photons.

1 The atom-cavity system

In this chapter I present the set of tools and techniques that are used to perform single-atom cavity-QED experiments. At the beginning of every experimental sequence, a controlled number of atoms is trapped and loaded into a standing wave dipole trap. Subsequently, the atoms are transported into a high-finesse optical resonator, which is probed by a weak laser. The time-dependent transmission signal is the main source of data which we use to study the atom-cavity system.

The setup has evolved for several years and is described in detail in former theses [15, 25–30]. In the following, I will therefore only give a short summary of the main components of our apparatus. Subsequently, I will present some theoretical background on cavity QED as well as simulation results relevant for this work.

1.1 Trapping and transporting single atoms

1.1.1 Magneto-optical trap

Neutral caesium atoms are trapped from the background gas in a magneto-optical-trap (MOT) [3]. The transitions for cooling and repumping are shown in fig. 1.1. The MOT is operated in two different regimes: If the magnetic field gradient is high (300 Gs/cm), the MOT is "closed" and almost no atoms are captured. To load new atoms, the gradient is reduced to 30 Gs/cm for a variable time of several 10 ms, which is adjusted such that the average number of loaded atoms is suitable for the experiment. In the context of this thesis, this means either one or two atoms.

The number of atoms in the MOT is determined by measuring the fluorescence with a single-photon counter (EG&G SPCM-200). Using computer control and feedback, the MOT loading process is repeated until the desired number of atoms is captured. Using this technique, we only transfer atoms from the MOT into the dipole trap and continue the experimental sequence if the number of atoms equals the desired one [31].

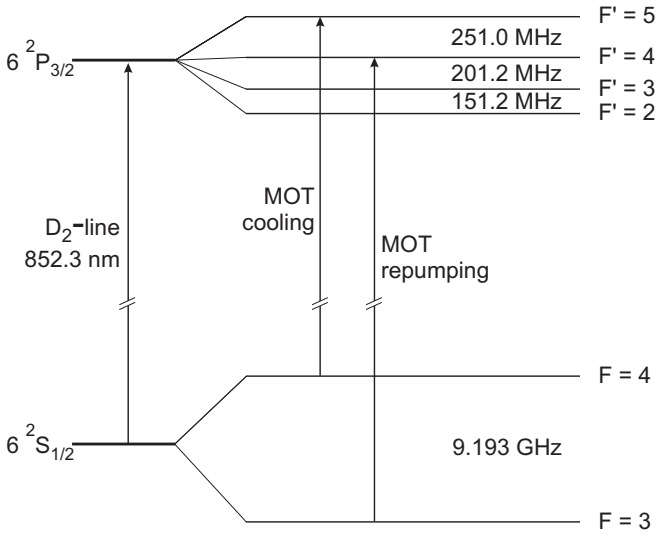

Figure 1.1: Relevant Cs-levels and MOT lasers.

1.1.2 Optical conveyor belt

From the MOT, the atoms are transferred into a standing wave far-off-resonant dipole trap (FORT) [32]. This trap is formed by two counter-propagating laser beams at $\lambda_{\mathrm{FORT}} = 1030$ nm, delivered by an Yb:YAG-Laser (ELS Versa Disk 1030), see fig. 1.2. For mode cleaning and to improve the pointing stability, high-power single mode optical fibres are used along the optical path. For a detailed description and characterisation of this fibre-setup see [15]. Both beams are focussed to a beam waist of $w_{\mathrm{FORT},0} = 34\,\mu\mathrm{m}$, located 3 mm away from the MOT-position and 1.6 mm away from the cavity. The beam radius at the cavity position is therefore $w_{\mathrm{FORT,cav}} = 37\,\mu\mathrm{m}$. With typically 1.8 W per beam, this results in a trap depth of

$$U_{\mathrm{FORT}} = \frac{3\pi c^2 I \Gamma}{2\omega_0^2 \Delta_{\mathrm{eff}}} = 1\,\mathrm{mK}\ , \tag{1.1}$$

where $\Gamma = 2\pi \times 5.22\,\mathrm{MHz}$ and the effective detuning Δ_{eff} takes into account contributions from both the D_1 and D_2 line, see e.g. [26, 27].

The transport of atoms is realised by inducing a time-dependent phase shift between the two counter-propagating laser beams, which causes the whole interference pattern to move, acting as an optical conveyor belt [33]. This is achieved with two acousto-optical modulators (AOMs) driven by a custom-build dual frequency driver (DFD 100, APE Berlin). With this setup, atoms can be transported over several mm within a few ms with sub-micrometer precision [34]. In order to transport the atoms to a predetermined position, e.g. exactly into the

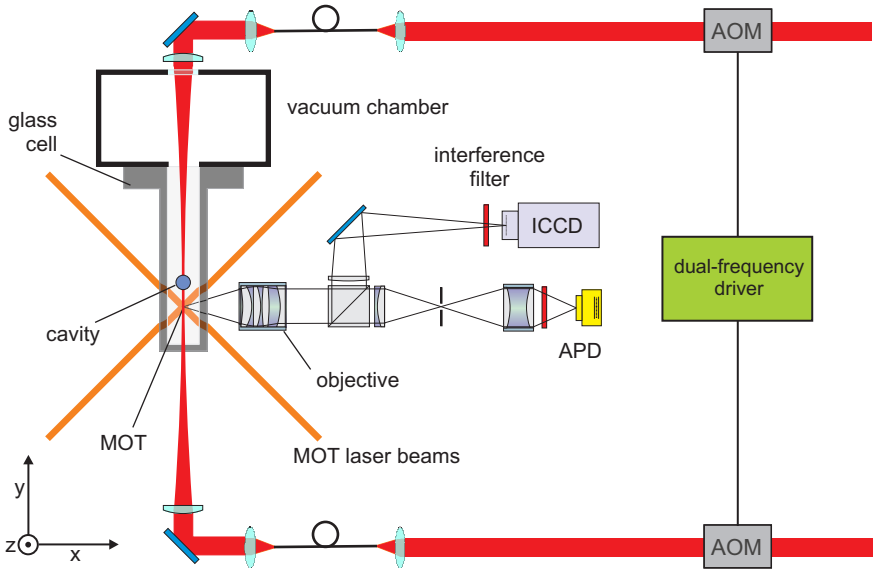

Figure 1.2: Schematic setup of MOT, optical conveyor belt and imaging optics.

cavity centre, their initial position is determined by fluorescence imaging. Atoms stored in the dipole trap are illuminated for 1 second with the MOT-molasses and imaged with an intensified CCD-camera (ICCD, Roper Scientific PI-MAX). Having done distance-calibration measurements before, the pixel coordinate of an imaged atom can then be translated into the required transportation distance, e.g. from the atomic position to the cavity-centre. Figure 1.2 shows the main components of our setup to capture, count, image, and transport single atoms.

1.2 Two-level atoms in a cavity

1.2.1 Cavity field and output power

Before treating the atom-field interaction, I will summarise relations between the cavity output and the intracavity field. The probe laser power P_{out} , transmitted by the cavity, is our main source of experimental information. In analytical expressions and numerical simulations, the mean intracavity photon number $n_p = \langle a^\dagger a \rangle$, where $a^\dagger$ is the photon creation operator, and the local intensity are usually used. Therefore it is required to relate those quantities including all experimental losses and imperfections.

The electric field operator for one cavity mode is given by [35]

$$\mathbf{E}_c(\mathbf{r}) = E_0 \mathbf{e}_c \psi(\mathbf{r})(a + a^\dagger) \,, \tag{1.2}$$

where $\mathbf{e}_c$ is the unit polarisation vector,

$$E_0 = \sqrt{\frac{\hbar\omega}{2\epsilon_0 V}} \tag{1.3}$$

is the r.m.s. electric field amplitude of the vacuum in the mode and ψ is the spatial amplitude mode function, which in our case is always the fundamental Gaussian mode TEM_{00}. Neglecting the divergence of the Gaussian mode, which is justified for a cavity much shorter than the Rayleigh length, the mode function is given by

$$\psi(\mathbf{r}) = \sin(kz)\exp\left(-\frac{x^2+y^2}{w_{\mathrm{cav},0}^2}\right) , \tag{1.4}$$

i.e. the mode function is normalised to $|\psi(\mathbf{r})| = 1$ at its maximum. The mode volume V is

$$V = \int |\psi(\mathbf{r})|^2 d^3r = \frac{\pi w_{\mathrm{cav},0}^2}{4} L , \tag{1.5}$$

where L is the length of the mode and $w_{\mathrm{cav},0}$ its waist. On resonance, input, circulating and output power are related according to [36]

$$P_{\mathrm{circ}} = \eta_{\mathrm{mode}}\, P_{\mathrm{in}}\, \frac{1}{\mathcal{T}} \left(\frac{\mathcal{T}}{\mathcal{T}+\mathcal{A}}\right)^2 , \; P_{\mathrm{out}} = \mathcal{T}\, P_{\mathrm{circ}} , \tag{1.6}$$

where η_{mode} is the mode matching efficiency and $\mathcal{T}$ and $\mathcal{A}$ are the intensity transmission and absorption coefficients of each mirror, respectively (see table 1.1 for the measured values), for which $\mathcal{A}+\mathcal{R}+\mathcal{T} = 1$ holds. With the round trip time $\tau_r = 2L/c$, the circulating power can be written in terms of the mean photon number n_p as

$$P_{\mathrm{circ}} = n_p \frac{\hbar\omega}{\tau_r} . \tag{1.7}$$

For the output power transmitted through *one* mirror we thus have

$$P_{\mathrm{out}} = P_{\mathrm{circ}}\, \mathcal{T} = n_p \frac{\hbar\omega}{\tau_r} \mathcal{T} . \tag{1.8}$$

This expression can be re-formulated to obtain a more compact form containing the commonly used cavity field decay rate κ, which is the half-width-half-maximum (HWHM)-linewidth of the cavity, using the relation

$$\kappa\tau_r = \frac{\pi}{\mathcal{F}} , \; \mathcal{F} = \frac{\pi\sqrt{\mathcal{R}}}{1-\mathcal{R}} \overset{\mathcal{R}\approx 1}{\approx} \frac{\pi}{\mathcal{T}+\mathcal{A}} \Rightarrow \frac{1}{\tau_r} = \frac{\kappa}{\mathcal{T}+\mathcal{A}} , \tag{1.9}$$

where the finesse $\mathcal{F}$ was introduced. The expression for the output power thus reads

$$P_{\text{out}} = \kappa n_p \hbar\omega \frac{\mathcal{T}}{\mathcal{T}+\mathcal{A}} = \kappa n_p \hbar\omega \eta_{\text{cav}} \ , \tag{1.10}$$

where

$$\eta_{\text{cav}} = \frac{\mathcal{T}}{\mathcal{T}+\mathcal{A}} \tag{1.11}$$

is the ratio of losses due to mirror transmission to total losses. In the experiment, we do not measure the transmitted power but the photon flux, which is

$$\Phi_{\text{out}} = \frac{P_{\text{out}}}{\hbar\omega} = \kappa n_p \eta_{\text{cav}} \ . \tag{1.12}$$

Photon flux Φ_{out} and output power P_{out} always refer to the light transmitted through *one* mirror; we do not measure the reflected probe laser light. In terms of the measured flux, the circulating power and the mean photon number are thus

$$P_{\text{circ}} = \hbar\omega \frac{\Phi_{\text{out}}}{\mathcal{T}} \ , \ n_p = \tau_r \frac{\Phi_{\text{out}}}{\mathcal{T}} = \frac{\Phi_{\text{out}}}{\kappa\eta_{\text{cav}}} \ . \tag{1.13}$$

The circulating intensity I_{circ} is connected to the circulating power P_{circ} by

$$I_{\text{circ}} = \frac{2P_{\text{circ}}}{\pi w_{\text{cav},0}^2} = \frac{1}{4}\frac{c}{V}\hbar\omega n_p \ , \tag{1.14}$$

where (1.5) for the mode-volume was inserted. The local intensity of the standing wave is given by

$$I_{\text{sw}}(\mathbf{r}) = 4 I_{\text{circ}} |\psi(\mathbf{r})|^2 \ , \tag{1.15}$$

so at the antinode we have the maximum intensity of

$$I_{\text{sw,max}} = \frac{c}{V}\hbar\omega n_p = \frac{8P_{\text{circ}}}{\pi w_{0,\text{cav}}^2} \ . \tag{1.16}$$

The second expression on the right hand site reflects the analogy to the free space case of a standing wave formed by *two* beams each with a power P_{circ} , so that in the familiar expression $I_{\text{sw,max}} = 4P_{\text{total}}/(\pi w_0^2)$ one has to replace P_{total} by $2P_{\text{circ}}$.

1.2.2 Dressed states and the master equation

The interaction of a single atom with the mode of an optical resonator is a textbook example of cavity quantum electrodynamics (CQED) [37–39]. The closed system of a two-level atom interacting with the field is described by the Jaynes-Cummings model [1].

The single-excitation Rabi-frequency is $2g$, where g is called the coupling strength which is given by

$$g(\mathbf{r}) = \frac{\mathbf{d}\cdot\mathbf{E}_c}{\hbar} = d\sqrt{\frac{\omega}{2\hbar\epsilon_0 V}}\psi(\mathbf{r}) \ . \tag{1.17}$$

Here $\mathbf{d}$ is the atomic dipole and d is the matrix element of the corresponding $|F, m_F\rangle \rightarrow |F', m_F'\rangle$ transition. An avoided crossing between the atomic and cavity energy levels leads to the formation of new eigenstates, which on resonance are spaced by $2g$. The lowest two dressed states above the ground state $|g, 0\rangle$ are given by

$$|+\rangle = \sin\theta\,|g,1\rangle + \cos\theta\,|e,0\rangle \tag{1.18a}$$
$$|-\rangle = \cos\theta\,|g,1\rangle - \sin\theta\,|e,0\rangle \ , \tag{1.18b}$$

where $|g(e), n\rangle$ is the state of the atom in the ground (excited) state with n photons in the cavity and θ is the mixing angle defined by

$$\tan 2\theta = -2g/(\omega_c - \omega_a) \ , \tag{1.19}$$

with ω_c and ω_a being the cavity and atomic resonance frequencies, respectively.

In a real world situation the atom-cavity system is always coupled to the environment, which is included into the formal description by two dissipation channels, namely light leaking from the cavity, described by κ as explained above, and spontaneous emission by the atom. The latter is characterised by $\Gamma = 1/\tau_e = 2\pi \times 5.22\,\mathrm{MHz}$, where $\tau_e = 30\,\mathrm{ns}$ is the lifetime of the excited state, i.e. Γ is the population decay rate. Often also $\gamma = \Gamma/2$ is used, meaning the dipole decay rate. A system is in the *strong-coupling regime*, if the coherent interaction g is larger than the two dissipation channels, i.e. $g > (\kappa, \gamma)$ [35]. Three dimensionless parameters that are often used to characterise cavity-QED systems are the single-atom cooperativity C_1, the critical photon number n_{cr} , and the critical atom number N_{cr} , defined as

$$C_1 = \frac{g^2}{2\kappa\gamma} \ , \ n_{\mathrm{cr}} = \frac{\gamma^2}{2g^2} \ , \ N_{\mathrm{cr}} = \frac{2\kappa\gamma}{g^2} = \frac{1}{C_1} \ . \tag{1.20}$$

For strongly coupled systems, $C_1 > 1$ and $N_{\rm cr} < 1$, which means that already a single atom changes the cavity response. $n_{\rm cr}$ is the intracavity photon number for which the atom is saturated and is < 1 for typical systems in the strong coupling regime. The dissipative processes are included into the description using a master-equation [2], which in a frame rotating with the probe laser frequency ω_p can be written as

$$\begin{aligned}\dot{\rho} = -\frac{i}{\hbar}[H_{\rm JC}\,,\rho] - \frac{i}{\hbar}[H_{\rm P}\,,\rho] \;&+\; \gamma(2\sigma\rho\sigma^\dagger - \sigma^\dagger\sigma\rho - \rho\sigma^\dagger\sigma) \\ &+\; \kappa(2a\rho a^\dagger - a^\dagger a\rho - \rho a^\dagger a)\;, \end{aligned} \tag{1.21}$$

where

$$H_{\rm JC} = -\hbar\Delta_{pa}\sigma^\dagger\sigma - \hbar\Delta_{pc}a^\dagger a + \hbar g(a\sigma^\dagger + \sigma a^\dagger) \tag{1.22}$$

is the Jaynes-Cummings Hamiltonian, $\sigma = |g\rangle\langle e|$ is the atomic lowering operator, and the detunings are defined as

$$\Delta_{pa} = \omega_p - \omega_a\;,\;\; \Delta_{pc} = \omega_p - \omega_c\;, \tag{1.23}$$

i.e. probe-atom and probe-cavity detuning. It is useful to define the cavity-atom detuning as

$$\Delta_{ca} = \omega_c - \omega_a = \Delta_{pa} - \Delta_{pc}\;, \tag{1.24}$$

because in the laboratory we usually first set Δ_{ca} and then vary Δ_{pc}. Cavity driving by the probe laser with frequency ω_p is described by

$$H_{\rm P} = -i\hbar\varepsilon(a + a^\dagger)\;, \tag{1.25}$$

where ε is the *driving strength*[1]. For an ideal empty cavity on resonance, i.e. without mirror losses, and assuming perfect mode matching, the driving strength is connected to the intracavity photon number $n_p = \langle a^\dagger a\rangle$ by

$$n_{p,0} = n_p(\omega_c = \omega_p = \omega_a, g = 0) = \frac{\varepsilon^2}{\kappa^2}\;, \tag{1.26}$$

where $n_{p,0}$ is the photon number for an empty cavity on resonance.

[1]The symbol varies throughout the literature, also η is often used

1.2.3 Equations of motion for weak driving

In the following I will summarise some outcomes of [24] relevant for our system.[2] The derivation is based on the assumption of a weakly driven cavity, i.e. only the states $|g,0\rangle$, $|g,1\rangle$, and $|e,0\rangle$ contribute to the system dynamics. In this case, equations of motion for the expectation values of the operators a and σ can be obtained:

$$\langle \dot{\mathbf{Y}} \rangle = \mathbf{A}\langle \mathbf{Y} \rangle + \mathbf{Z}_\varepsilon \ , \tag{1.27}$$

where

$$\mathbf{Y} = \begin{pmatrix} a \\ \sigma \end{pmatrix}, \quad \mathbf{A} = \begin{pmatrix} i\Delta_{pc} - \kappa & -ig \\ -ig & i\Delta_{pa} - \gamma \end{pmatrix}, \quad \mathbf{Z}_\varepsilon = \begin{pmatrix} \varepsilon \\ 0 \end{pmatrix} \ , \tag{1.28}$$

For the description of interaction, photon number, and excited state population we need a similar expression for the corresponding operator products, which reads

$$\langle \dot{\mathbf{X}} \rangle = \mathbf{B}\langle \mathbf{X} \rangle + \varepsilon \langle \mathbf{I} \rangle \ , \tag{1.29}$$

with

$$\mathbf{X} = \begin{pmatrix} a^\dagger\sigma + \sigma^\dagger a \\ -i\left(a^\dagger\sigma - \sigma^\dagger a\right) \\ a^\dagger a \\ \sigma^\dagger\sigma \end{pmatrix}, \quad \mathbf{B} = \begin{pmatrix} -\tilde{\gamma} & -\Delta_{ca} & 0 & 0 \\ \Delta_{ca} & -\tilde{\gamma} & -2g & 2g \\ 0 & g & -2\kappa & 0 \\ 0 & -g & 0 & -2\gamma \end{pmatrix} \tag{1.30}$$

$$\mathbf{I} = \begin{pmatrix} \sigma + \sigma^\dagger \\ -i\left(\sigma - \sigma^\dagger\right) \\ a + a^\dagger \\ 0 \end{pmatrix}, \quad \tilde{\gamma} = \gamma + \kappa \ , \Delta_{ca} = \Delta_{pa} - \Delta_{pc} = \omega_c - \omega_a \ .$$

Steady state solution for an atom at rest

Solving $\langle \dot{\mathbf{X}} \rangle = 0$ yields the expectation values for a motionless atom at steady state:

[2] In the cited article, the decay rate Γ is the dipole decay rate, which is labelled γ in this thesis

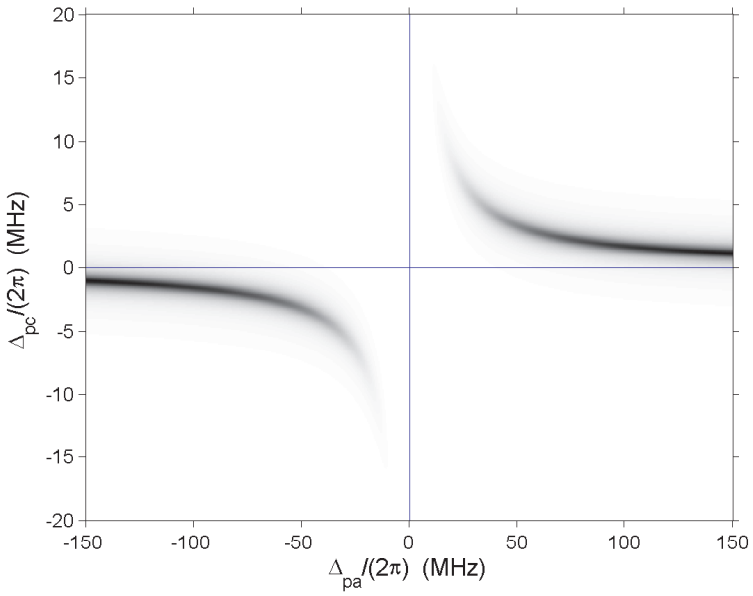

Figure 1.3: Cavity transmission spectrum calculated according to (1.33) with parameters $(g, \kappa, \gamma)/2\pi = (13.1, 0.4, 2.6)$ MHz. White = no transmission, black = maximum transmission.

$$\langle \mathbf{X} \rangle^{(0)} = \frac{\varepsilon^2}{|\det(\mathbf{A})|^2} \begin{pmatrix} 2\Delta_{pa} g \\ -2g\gamma \\ \Delta_{pa}^2 + \gamma^2 \\ g^2 \end{pmatrix} , \tag{1.31}$$

where the superscript (0) indicates the steady state solution and the determinant of $\mathbf{A}$ is given by

$$\det(\mathbf{A}) = \gamma\kappa + g^2 - \Delta_{pa}\Delta_{pc} - i(\Delta_{pc}\gamma + \Delta_{pa}\kappa) . \tag{1.32}$$

One important result is an analytical expression for the average intracavity photon number, $\langle X_3 \rangle^{(0)} = \langle a^\dagger a \rangle$, which is

$$\begin{aligned} n_p(\Delta_{pa}, \Delta_{pc}, g) &= n_{p,0} \frac{\kappa^2(\Delta_{pa}^2 + \gamma^2)}{(\gamma\kappa + g^2 - \Delta_{pa}\Delta_{pc})^2 + (\Delta_{pa}\kappa + \Delta_{pc}\gamma)^2} \\ &= n_{p,0} \bar{T}(\Delta_{pa}, \Delta_{pc}, g) , \end{aligned} \tag{1.33}$$

where the normalised transmission $\bar{T}$ was introduced and $n_{p,0}$ is the photon number for an empty cavity on resonance. Fig. 1.3 shows a plot of $\bar{T}$ for our

parameters. For all data presented in chapter 2, the probe laser is initially resonant with the cavity, i.e. $\Delta_{pc} = 0$. For this case, $\Delta_{pa} = \Delta_{ca}$ and the expression for the normalised transmission simplifies to

$$\bar{T}^{(\Delta_{\mathrm{pc}}=0)}(\Delta_{ca}, g) = \frac{\kappa^2(\Delta_{ca}^2 + \gamma^2)}{(\gamma\kappa + g^2)^2 + (\Delta_{ca}\kappa)^2} \,. \tag{1.34}$$

For large cavity-atom detunings $\Delta_{ca} \gg \gamma$ the expression for the normalised transmission reads

$$\bar{T}^{(\Delta_{\mathrm{pc}}=0)}(\Delta_{ca} \gg \gamma, g) = \frac{\kappa^2}{\kappa^2 + \left(\frac{|g|^2}{\Delta_{ca}}\right)^2} \,, \tag{1.35}$$

which is a Lorentzian lineshape with a HWHM-linewidth of κ. So in the dispersive regime the resonance-splitting of the coupled atom-cavity system passes into a shift of the cavity resonance frequency by g^2/Δ_{ca}.

1.3 Cavity setup and characteristics

The high-finesse cavity was integrated into the existing single-atom setup containing the MOT-optics, dipole trap etc. by means of a holder that allows 3-D positioning of the cavity. Details of the cavity setup and on characterisation measurements are discussed in [14,15,29,30]. Here I summarise the main parameters in table 1.1.

Because of the very small cavity linewidth, stabilising the cavity is a very important and demanding aspect of our experimental setup. In addition to the probe laser, an additional stabilisation laser (referred to as "lock laser" from now on) is coupled into the cavity. From its reflected light field an error signal is generated using the Pound-Drever-Hall (PDH) method [40]. The cavity length is controlled by piezo-electric shear actuators to which the mirror substrates are glued, see fig. 1.4.

The lock laser wavelength for the experiments covered in chapter 2 is $\lambda_{\mathrm{lock}} = 845\,\mathrm{nm}$, i.e. blue detuned from the atomic resonance. In chapter 3 I will present results on using a red-detuned lock laser at 857 nm. The lock laser is stabilised to a transfer-cavity with good passive stability, which in turn is locked to the probe laser. Using this "locking-chain", it is possible to set the cavity-length such that both probe and lock laser are resonant with the cavity at the same time. Using AOMs, the detunings Δ_{ca} and Δ_{pc} can be controlled independently over a wide range. This allows us to perform experiments in very different regimes, from resonant to far dispersive and either blue- or red-detuned.

Parameter		Value
mirror distance*	L	158.5µm
mode waist	$w_{0,\mathrm{cav}}$	23.15 µm
free spectral range	$\omega_{\mathrm{FSR}} = 2\pi c/(2L)$	$2\pi \times 946\,\mathrm{GHz}$
cavity field decay rate†	κ	$2\pi \times (0.40 \pm 0.02)$ MHz
cavity linewidth (FWHM)	$\omega_{\mathrm{FWHM}} = 2\kappa$	$2\pi \times (0.80 \pm 0.04)$ MHz
birefringent splitting	$\Delta\omega_{br}$	$2\pi \times 3.9\,\mathrm{MHz}$
finesse†	$\mathcal{F} = c\pi/(2L\kappa)$	$(1.2 \pm 0.1) \times 10^6$
mirror transmission†	$\mathcal{T}$	(0.6 ± 0.1) ppm
mirror absorption†	$\mathcal{A}$	(2.0 ± 0.2) ppm
maximum coupling strength	$g_{\max}$	$2\pi \times 13.1\,\mathrm{MHz}$
atomic dipole decay rate	γ	$2\pi \times 2.6\,\mathrm{MHz}$
cooperativity parameter	$C_1 = g_{\max}^2/(2\kappa\gamma)$	82
critical photon number	$n_{\mathrm{cr}} = 2g_{\max}^2/\gamma$	0.020
critical atom number	$N_{\mathrm{cr}} = 1/C_1$	0.012

Table 1.1: Summary of some important cavity and coupling parameters. The value of the maximum coupling $g_{\max}$ is explained later. * The mirror distance is given for typical experimental conditions, including heating effects by the YAG laser. This explains the difference to the cavity length given in [29], which is valid for a "cold" cavity. † See [30] for details on the measurement.

As mentioned already, the transmitted probe laser light is our main source of experimental information. However, the transmitted lock laser co-propagates in the same transversal mode with its power being around 6 orders of magnitude higher (a typical lock laser power coupled into the cavity is $P_{\mathrm{lock}} \approx 1\,\mu\mathrm{W}$). Since the two signals have to be detected separately the lock laser must be filtered out to a high degree to facilitate detection of the probe-light on a single-photon level. The two fields are orthogonally polarised, and in a first step most of the lock laser light is reflected and send to an APD by a Glan-Taylor polariser. Behind the polariser, an interference filter is used to further reduce the amount of lock laser light. The probe light is then guided to a sealed box on an optical table via a single-mode fibre, thereby making sure that no stray light is detected. Inside the box, the light is reflected by a volume holographic grating (company ONDAX, for details see [30]), filtering the remaining lock laser light, and is finally detected by a single-photon APD (Perkin Elmer SPCM-AQRH-13).

1.3.1 Detection efficiency

Losses along the optical path are due to various optical components (glass cell, lenses, half- and quarter wave plate), leading to a transmission coefficient of

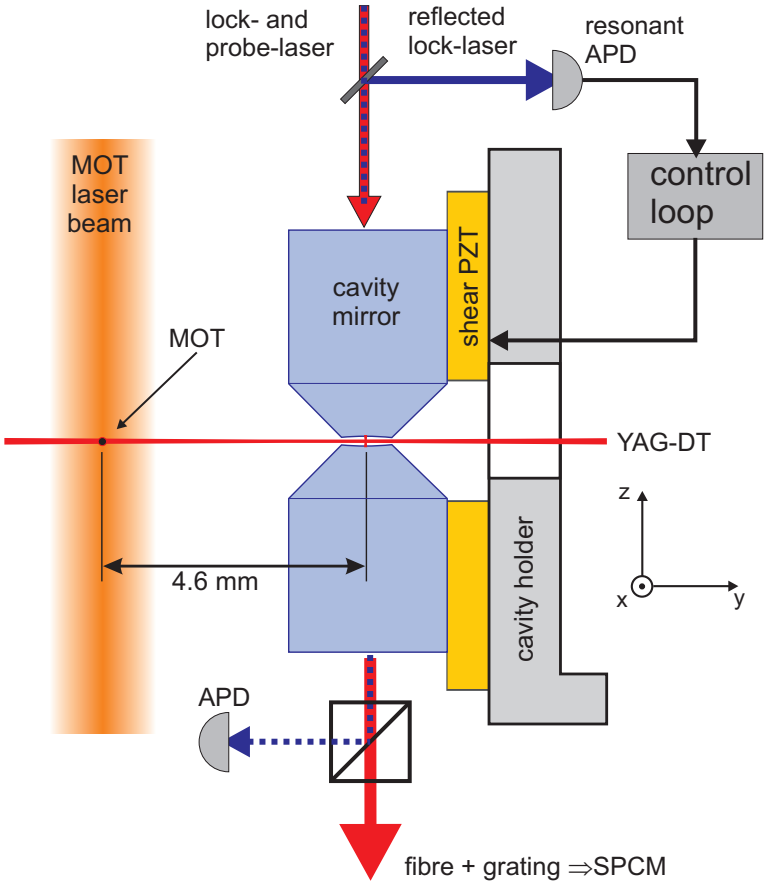

Figure 1.4: Sketch of the cavity setup showing MOT beams, dipole trap beams and cavity mirrors approximately up to scale. For details on the probe-detection setup, see [30]. The APD is used to detect the lock laser transmission.

$\eta_{\mathrm{opt}} = 0.82$. The interference filter has a transmission of $\eta_{\mathrm{IF}} = 0.77$ and the coupling efficiency into the single-mode fibre is $\eta_{\mathrm{fibre}} = 0.66$. The volume holographic grating's reflectivity at the probe laser wavelength is $\eta_{\mathrm{VHG}} = 0.93$ and the quantum efficiency of the SPCM at 852 nm is $\eta_{\mathrm{SPCM}} = 0.49$. This leads to a detection efficiency of

$$\eta_{\mathrm{det}} = \eta_{\mathrm{opt}}\,\eta_{\mathrm{IF}}\,\eta_{\mathrm{fibre}}\,\eta_{\mathrm{VHG}}\,\eta_{\mathrm{SPCM}} = 0.19\,. \tag{1.36}$$

Compared to the detection setup presented in [15], the detection efficiency could be improved by more than a factor of three. Knowing the overall detection efficiency, we can infer the average intracavity photon number n_p or the intracavity intensity from the actual SPCM count rate R_{D} . The detector count rate R_{D} is equal to the photon flux directly behind the cavity, reduced by the aforementioned losses:

$$R_{\mathrm{D}} = \Phi_{\mathrm{out}} \cdot \eta_{\mathrm{det}} \tag{1.37}$$

The expressions derived in section 1.2.1 are extended to include the detection efficiency and now read

$$P_{\mathrm{circ}} = \hbar\omega \frac{R_{\mathrm{D}}}{\eta_{\mathrm{det}}\,\mathcal{T}} , \tag{1.38}$$

$$n_p = \tau_r \frac{R_{\mathrm{D}}}{\eta_{\mathrm{det}}\,\mathcal{T}} = \frac{R_{\mathrm{D}}}{\kappa\eta_{\mathrm{det}}\,\eta_{\mathrm{cav}}} = \frac{R_{\mathrm{D}}}{\kappa\eta} , \tag{1.39}$$

$$I_{\mathrm{sw,max}} = \frac{8P_{\mathrm{circ}}}{\pi w_{0,\mathrm{cav}}^2} , \tag{1.40}$$

where the total efficiency $\eta = \eta_{\mathrm{det}}\,\eta_{\mathrm{cav}}$ was introduced. With the measured values for $\mathcal{T}$ and $\mathcal{A}$, we get $\eta_{\mathrm{cav}} = 0.23$ and $\eta = 0.044$. Since all quantities are proportional to R_{D} (typically 20 to 30 ms^{-1}) and contain otherwise only constants and experimental parameters which do not change, their numerical values are calculated for $\omega = \omega_p = 2\pi \times 351.7\,\mathrm{THz}$ to be

$$P_{\mathrm{circ}} = \frac{R_{\mathrm{D}}}{1\,\mathrm{ms}^{-1}} \cdot 2.0\,\mathrm{nW} , \tag{1.41}$$

$$n_p = \frac{R_{\mathrm{D}}}{1\,\mathrm{ms}^{-1}} \cdot 0.009 , \tag{1.42}$$

$$I_{\mathrm{sw,max}} = \frac{R_{\mathrm{D}}}{1\,\mathrm{ms}^{-1}} \cdot 9.7\,\mathrm{W\,m}^{-2} . \tag{1.43}$$

1.3.2 Confinement and beat length

An atom inside the cavity is subject to two dipole potentials: firstly the conveyor-belt created by the YAG laser (FORT), and secondly the potential which results from the lock laser. In the experiments discussed in chapters 1 and 2, the lock laser wavelength is $\lambda_{\mathrm{lock}} = 845\,\mathrm{nm}$, i.e. 3 cavity free spectral ranges blue detuned from the atomic transition. In this case the dipole potential is repulsive, thus not forming potential wells but "walls". An atom is therefore confined along the cavity axis (z-axis) to a node of the lock laser standing wave. In the direction along the conveyor belt (y-axis), it is trapped at an anti-node with a small oscillation radius, since $\lambda_{\mathrm{FORT}}/2 = 515\,\mathrm{nm}$. Along x, the atom can move over several µm, because the beam radius of the dipole trap at this point is

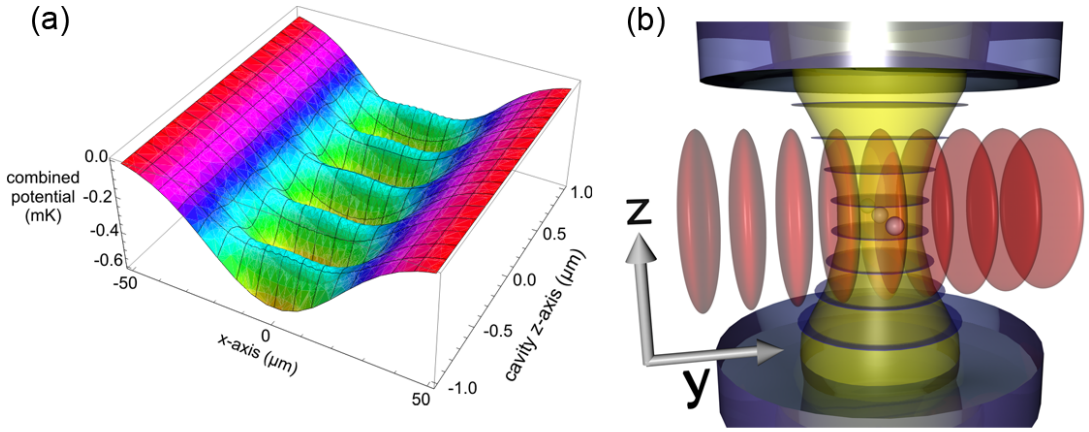

Figure 1.5: Effect of a blue-detuned lock laser. (a) Combined potential of the YAG-dipole trap and the potential "walls" of a blue detuned laser. (b) Schematic drawing of the confinement by the lock laser, which is symbolised as blue disks in this images. The standing-wave nature of the probe laser (yellow) is not shown. This drawing is meant to be descriptive and is not based on actual physical length scales, lock laser powers etc.

$w_{\mathrm{FORT,cav}} = 37\,\mu\mathrm{m}$ and thus the dipole potential in this radial direction is very shallow. This situation is schematically depicted in fig. 1.5 in a sketch of the cavity and the combined potential.

The lack of a strong confinement along one axis is clearly a disadvantage in terms of good localisation and therefore strong coupling. Notwithstanding this fact, the main reason to use a blue-detuned laser is that the atoms are located at the intensity minima, where the scattering rate and the absolute AC-Stark shift are lowest. In contrast, for a red-detuned laser where the atoms are trapped at the intensity *maxima*, the atoms will be affected by photon scattering to a higher degree. In chapter 3 I will present experiments making use of a red-detuned lock laser.

Beating between probe and lock laser

Due to the lock laser potential, the z-position of the atoms is restricted to an equally spaced series of trapping sites, namely the nodes of the lock laser standing wave, separated by $\lambda_{\mathrm{lock}}/2$. Since the probe laser has a different wavelength λ_{probe}, there is a beating between these two different standing waves. If we choose the z axis coordinate such that for $z = 0$ node and antinode of lock and probe laser, respectively, coincide, the intensities are written as

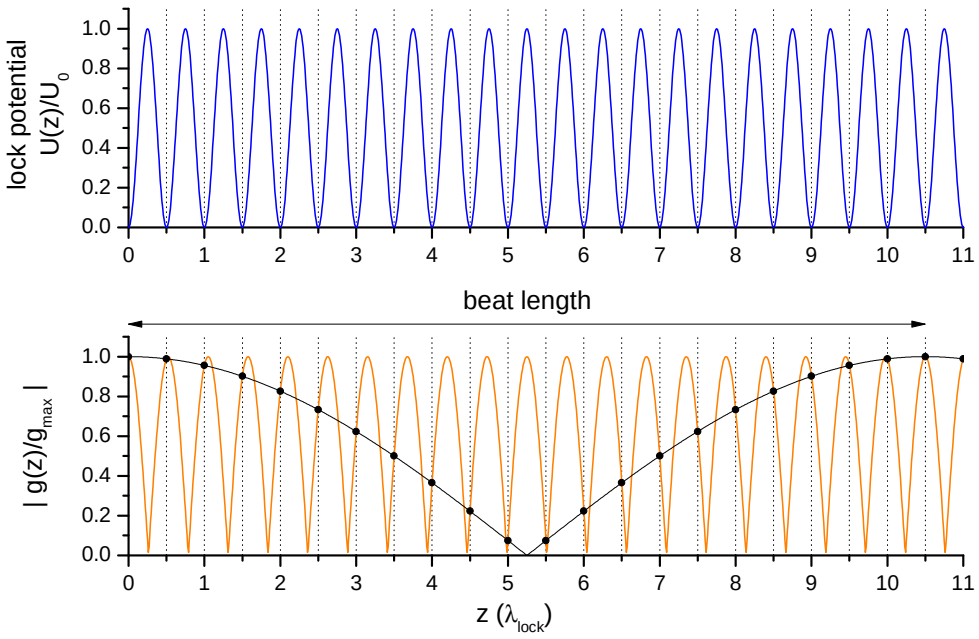

Figure 1.6: Beating between probe and lock laser standing wave. For illustrative purposes, here $\lambda_{\text{probe}} = 1.05\lambda_{\text{lock}}$, yielding $d_{\text{beat}} = 10.5\lambda_{\text{lock}}$. The dotted vertical lines mark the trapping sites given by lock laser nodes, indicated also in the lower graph by the black dots. The solid black line in the lower graph is the continuous expression for $|g(z)/g_{\max}|$.

$$I_{\text{lock}}(z) = I_{l,0}\sin^2\left(\frac{2\pi}{\lambda_{\text{lock}}}z\right) \ , \ I_{\text{probe}}(z) = I_{p,0}\cos^2\left(\frac{2\pi}{\lambda_{\text{probe}}}z\right) \tag{1.44}$$

The beat length d_{beat} , defined as the distance between places of the same phase, i.e. the envelope of $I_{\text{lock}}(z) + I_{\text{probe}}(z)$, is given by

$$\frac{2\pi}{\lambda_{\text{lock}}}d_{\text{beat}} = \frac{2\pi}{\lambda_{\text{probe}}}d_{\text{beat}} + \pi \Rightarrow d_{\text{beat}} = \frac{\lambda_{\text{probe}}\,\lambda_{\text{lock}}}{2|\lambda_{\text{probe}} - \lambda_{\text{lock}}|} \ . \tag{1.45}$$

The beating leads to a position-dependent maximum coupling strength as depicted in fig. 1.6. At the trapping sites, the local coupling strength is given by

$$g_{\max,\text{local}}(z) = g_{\max,0}\cos\left(\frac{2\pi}{\lambda_{\text{probe}}}z\right) \text{ for } z = n\frac{\lambda_{\text{lock}}}{2} \ , n = 0, 1, 2, 3, \ldots \ , \tag{1.46}$$

which is a discrete expression for g only valid at the trapping sites, plotted as black dots in fig. 1.6. A continuous expression for $g(z)$, which describes the envelope of $g(z)$ and not the oscillations on the lengthscale of λ_{probe} , reads

$$g(z) = g_{\max,0} \left| \cos\left(\frac{\pi}{d_{\text{beat}}} z\right) \right| \tag{1.47}$$

and is shown in fig. 1.6 as the black solid line. This expression will be used later in a numerical simulation describing the effect of thermal motion of the atom.

In the experiment, we want the trapping site located at the centre of the cavity (halfway between the mirrors) to coincide with a probe laser antinode, because this is the position where the atoms are most likely to be inserted by the optical conveyor belt. Expressing the cavity length as $L = m_p \lambda_{\text{probe}}/2 = m_l \lambda_{\text{lock}}/2$, this is achieved if $\Delta_{lp} = m_l - m_p = 1, 3, 5, ...$ for $\lambda_{\text{lock}} < \lambda_{\text{probe}}$. Likewise, $\Delta_{lp} = -2, -4, -6, ...$ for $\lambda_{\text{lock}} > \lambda_{\text{probe}}$. For the two cases relevant to this thesis, the magnitude of the beat length is

$$d_{\text{beat}} = \begin{cases} 51.4\,\mu\text{m} & \text{for} \quad \lambda_{\text{lock}} = 845\,\text{nm}, \Delta_{lp} = 3\ , \\ 73.0\,\mu\text{m} & \text{for} \quad \lambda_{\text{lock}} = 857\,\text{nm}, \Delta_{lp} = -2\ . \end{cases} \tag{1.48}$$

When the atoms are transported into the cavity, they randomly enter one of the possible trapping sites along the cavity axis because of their thermal oscillation. The magnitude of those oscillations and the beat length determine to which extend this effects reduces the ensemble-averaged coupling strength.

Obviously the issue of insertion into different positions along the cavity axis is less critical for a larger beat length, i.e. if the lock laser wavelength is close to the probe wavelength. On the other hand, being detuned by only one free spectral range has the drawback that the separation of probe and lock laser using interference filter and grating is more difficult, owing to the finite bandwidth of the optical components. Empirically we found out that being blue detuned by three free spectral ranges, i.e. $\lambda_{\text{lock}} = 845\,\text{nm}$, is a good compromise.

1.4 Optical pumping

In the theory outlined in section 1.2.2 the atom was treated as a two-level system, but in our experimental setting there is no closed transition we can use. This is because of the birefringent splitting of the cavity resonances, which has the effect that the cavity supports only linearly polarised modes. Depending on the direction of the quantization axis (**QA**), the interaction of the probe laser with the atom can thus either by described by π-transitions (for $\mathbf{E}_p \parallel \mathbf{QA}$) or simultaneous σ_+ and σ_- transitions (for $\mathbf{E}_p \perp \mathbf{QA}$), referred to as $\sigma_\pm$ from now

on. The atom can be off-resonantly excited to $|F' = 4\rangle$ and decay to the other ground state $|F = 3\rangle$. Therefore a repumping laser (short: repumper) resonant with the $|F = 3\rangle \rightarrow |F' = 4\rangle$ transition is applied along the dipole trap to bring the atom back to $|F = 4\rangle$.

Assuming the repumper is sufficiently strong, I will neglect optical pumping to the state $|F = 3\rangle$ in this section and will only consider the two manifolds $|F = 4\rangle$ and $|F' = 5\rangle$. Hyperfine-state-changing scattering will be treated in section 1.5.2.

Excitation by the probe laser leads to a specific population distribution of the m_F groundstates $P(m_F)$, depending on the orientation of the electric field and the quantization axis. A distribution over many Zeeman levels implies that there is not a single, well defined coupling strength g, but different $g(m_F, q)$, where q is $-1, 0, 1$ for σ_+, π, and σ_- transitions, respectively. In the following, I will first consider free space optical pumping using an analytical solution of the density matrix equation. To include the effects of the cavity and evaluate to which degree the results are different, a master equation including the m_F sublevels is formulated and solved numerically.

1.4.1 Free space optical pumping: Analytical expressions

The effect of Zeeman degeneracy on the steady-state of an atom was studied theoretically in a series of papers by Bo Gao [41–43]. In the limit of weak pumping and for a coordinate system where $\mathbf{E}_p \parallel \mathbf{QA}$, the analytical result for the steady-state population of state $|F, m\rangle$ for a transition from a ground-state $|F\rangle$ to an excited-state $|F'\rangle$ is given by

$$P(m_F) = \langle F, m|\rho^{SS}|F, m\rangle = \frac{\chi_m}{\sum_{i=-F}^{F} \chi_i} , \tag{1.49}$$

where ρ^{SS} is the steady-state density matrix, and χ_m is defined by

$$\chi_m = \left(\prod_{i=-m+1}^{F} f_i^2 h_i^2 \right) \left(\prod_{j=m+1}^{F} f_j^2 h_j^2 \right) , \tag{1.50}$$

and

$$f_k = (-1)^{F'-k} \begin{pmatrix} F' & 1 & F \\ -k & 1 & k-1 \end{pmatrix} , \; h_k = (-1)^{F'-k} \begin{pmatrix} F' & 1 & F \\ -k & 0 & k \end{pmatrix} , \tag{1.51}$$

where the parentheses are Wigner $3j$-symbols. A general theoretical outcome is that for this choice of a coordinate system all coherences vanish. For $\sigma_\pm$ pumping, no analytical formula is given in the cited article, but the density

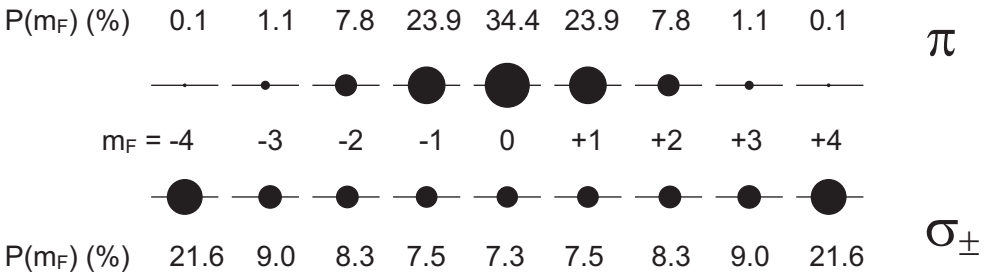

Figure 1.7: Ground state population for π and $\sigma_\pm$ pumping without taking any cavity effects into account. The area of the dots is proportional to the probability that the m_F sublevel is occupied.

matrix $\rho(\sigma_\pm)$ can be obtained from the diagonal density matrix $\rho(\pi)$, which contains only the populations. Since the physical situation is the same for both cases, i.e. a linearly polarised laser interacting with an ensemble of atoms, $\rho(\sigma_\pm)$ can be calculated by a rotation of the coordinate system of the form

$$\rho(\sigma_\pm) = D(0, \pi/2, 0)\rho(\pi)D(0, \pi/2, 0)^T \,, \tag{1.52}$$

where $D(\alpha, \beta, \gamma)$ is the Wigner-D-matrix [44] (or Wigner rotation matrix) as a function of the Euler angles α, β, γ. The diagonal elements (populations) of $\rho(\pi)$ and $\rho(\sigma_\pm)$ are shown in fig. 1.7. In contrast to $\rho(\pi)$, the rotated matrix $\rho(\sigma_\pm)$ contains also nonzero off-diagonal elements (coherences).

1.4.2 Optical pumping in the cavity: Numerical calculation

In the free space calculations above, the light intensity was assumed to be small and constant, but from (1.34) it is clear that in the cavity the intensity depends on m_F due to $g(m_F, q)$. To answer the question, to which extend the results of the free space calculations are still valid, the master equation for a multi-level atom is solved numerically.

Any expectation value, e.g. the intracavity photon number or the population of a certain state, can be calculated from the steady-state density matrix ρ^{SS} of the system. The following formulation of the Hamiltonian including the Zeeman-sublevels, and the numerical implementation in MATLAB with the Quantum Optics Toolbox [45] are based on [46, 47].

A dipole transition operator for the $|F = 4\rangle \rightarrow |F' = 5\rangle$ transition is defined as

$$D_q = \sum_{m_F=-4}^{4} |F=4, m_F\rangle \langle F=4, m_F| \, d_q \, |F'=5, m_F+q\rangle \langle F'=5, m_F+q| \ , \tag{1.53}$$

where $q = \{-1, 0, 1\}$ and d_q is the dipole operator for $\{\sigma_-, \pi, \sigma_+\}$ transitions, respectively. The normalisation is such that $\langle 4, 4| \, d_1 \, |5', 5'\rangle = 1$. The Hamiltonian is

$$H = -\hbar\Delta_{pa} \sum_{m'_F=-5}^{5} |F'=5', m'_F\rangle \langle F'=5', m'_F| \ - \ \hbar\Delta_{pc} a^\dagger a + \hbar\varepsilon(a + a^\dagger) + H_{\text{int}} \ , \tag{1.54}$$

where the interaction Hamiltonian depends on the transitions q:

$$H_{\text{int}}^{(q)} = \hbar g(a^\dagger D_q + D_q^\dagger a) \ , \tag{1.55}$$

when q is either -1,0, or 1. For the case of simultaneous σ_- and σ_+ coupling, the interaction Hamiltonian is given by

$$H_{\text{int}}^{(\pm 1)} = \hbar g \left(a^\dagger \left(\frac{1}{\sqrt{2}}(D_{-1} + D_{+1}) \right) + \left(\frac{1}{\sqrt{2}}(D_{-1} + D_{+1}) \right)^\dagger a \right) \ . \tag{1.56}$$

The master equation for the system is

$$\dot{\rho} = \mathcal{L}\rho = -\frac{i}{\hbar}[H, \rho] + \kappa\mathcal{D}[a]\rho + \gamma \sum_{q=-1}^{1} \mathcal{D}[D_q]\rho \ , \tag{1.57}$$

where the decay operator $\mathcal{D}$ for any operator c is defined as

$$\mathcal{D}[c]\rho = 2c\rho c^\dagger - c^\dagger c\rho - \rho c^\dagger c \ . \tag{1.58}$$

The steady state solution can be obtained numerically by setting $\dot{\rho} = 0$.

Results of the numerical simulation – ground state population

I considered the special case $\Delta_{pc} = 0$, which is the usual setting for our experiments. I calculated the steady state density matrix ρ^{SS} for different detunings Δ_{ca} and for both optical pumping settings discussed so far. The pumping strength ε is set to a value fulfilling the weak excitation limit. The results for the ground state populations $\langle F=4, m| \, \rho^{SS} \, |F=4, m\rangle$ are summarised in table

m_F-state	detuning $\Delta_{ca}/2\pi$ (MHz)				
	50	100	200	500	1000
0	38	37.9	37.4	35.9	34.9
±1	24.4	24.3	24.3	24.1	24.0
±2	6.12	6.2	6.4	7.1	7.5
±3	0.51	0.53	0.61	0.84	1
±4	0.01	0.01	0.02	0.03	0.05

Table 1.2: Ground state population $P(m_F)$ in % for π-pumping by the probe laser for different detunings Δ_{ca}.

1.2 for different detunings Δ_{ca} and the case of π-pumping. For large detunings, $P(m_F)$ approaches the result of the free-space calculation, cf. fig. 1.7. Closer to resonance, the population is more centred around $|F = 4, m_F = 0\rangle$.

For simultaneous σ_- and σ_+ coupling, the variation in the population distribution is less than 1 % for a range of $\Delta_{ca}/(2\pi) = 50$ to 500 MHz and agrees with the free-space result presented above. In summary, for both cases the modification of $P(m_F)$ compared to free space optical pumping due to the m_F dependent intracavity power is rather small.

Results of the numerical simulation – transmission

The main source of information in our system is the transmission of the probe laser through the cavity. A time-averaged transmission signal allows us to infer the average coupling strength and to compare it with theoretical predictions, see section 1.6 at the end of this chapter.

Using the formalism explained above, the normalised transmission for different detunings Δ_{ca} and with $\Delta_{pc} = 0$ was calculated for different polarisation settings ($q = 0$, $q = +1$, $q = \pm1$) from the steady-state density matrix. Figure 1.8 shows that $\bar{T}_\rho^{(\Delta_{pc}=0)}(\Delta_{ca}, q)$ is *exactly* the same for $q = 0$ and $q = \pm1$, i.e. the intra cavity photon number does not depend on the orientation of the quantisation axis. For $q = 1$ the transmission is lower, which is to be expected because the coupling is strongest for the cycling transition $|4, 4\rangle \rightarrow |5', 5'\rangle$.

In the the two-level model $\bar{T}_{\mathrm{2L}}^{(\Delta_{pc}=0)}(\Delta_{ca}, g)$, cf. (1.33), g is a free parameter. With a least squares method, a value of $g/(2\pi) = 13.1$ MHz was determined which provides the best agreement with the density-matrix curve for $q = 0$. Hence our system can – in terms of cavity transmission – be described as a two-level atom interacting with the cavity. This value of 13.1 MHz is given in table 1.1 as $g_{\max}$.

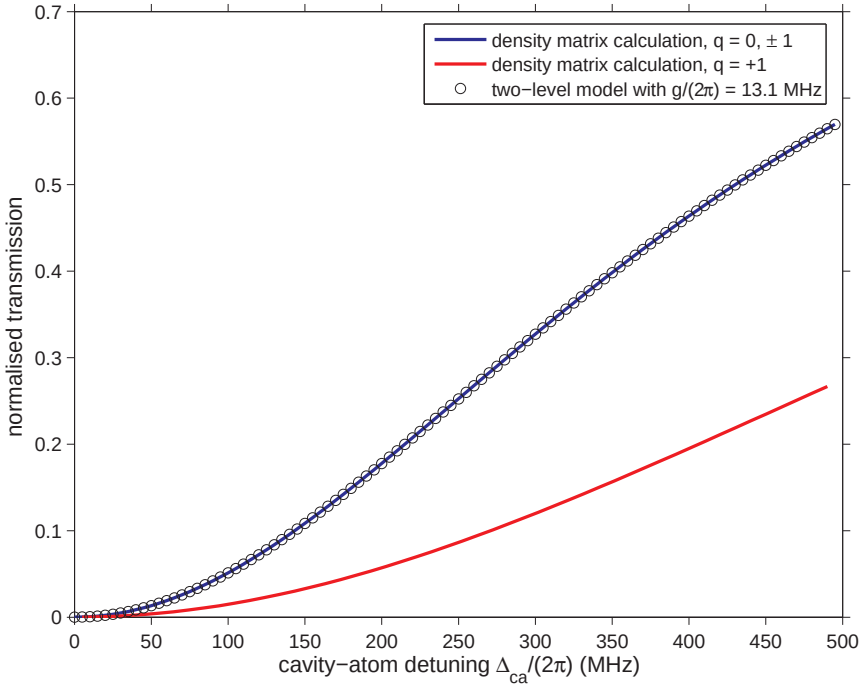

Figure 1.8: Normalised transmission of the probe laser through the cavity, $\bar{T}(\Delta_{ca})$. The blue solid line shows the result of the density-matrix calculation for the case of π-transitions ($q = 0$) and simultaneous σ_+ and σ_- transitions ($q = \pm 1$), which coincide exactly. The red line is the case of pure σ_+ pumping, corresponding to a coupling of $g = 2\pi \times 18\,\mathrm{MHz}$, which is not realised in the experiment. The circles are the best-fit with g as a fitting parameter for the two-level model.

Results of the numerical simulation – time dependence

With the Quantum Optics Toolbox, also the time dependence of observables can be computed by integrating the master equation, yielding an array of density matrices for successive time-steps. Using this method, I calculated how the population of the m_F states evolves from an initial equal distribution to the steady-state result presented above. Assuming realistic experimental parameters, it turns out that it takes a few milliseconds until the steady-state is reached, for both orientations of the quantization axis, see fig 1.9 (a) and (b). The transmission also changes because the initial average coupling is lower than the steady state value. This is an important insight, the implications of which will be discussed in conjunction with nondestructive state measurements in chapter 2.

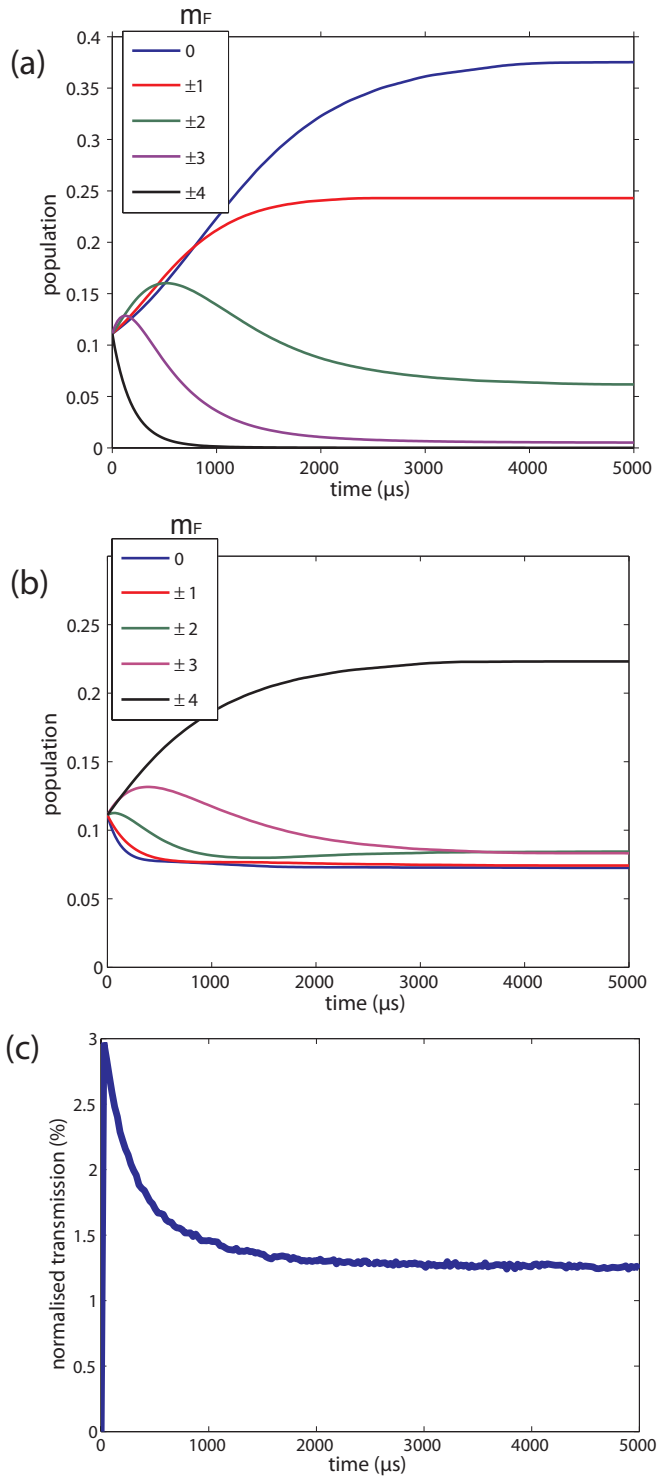

Figure 1.9: Results of a numerical density matrix simulation yielding $\rho(t)$, from which the time-dependent expectation values $\langle F = 4, m_F | \, \rho(t) \, | F = 4, m_F \rangle$ are obtained. The detuning is $\Delta_{ca}/(2\pi) = 50\,\mathrm{MHz}$ for all graphs, the intracavity intensity was calculated for an empty cavity photon number of $n_{p,0} = 0.1$. (a) and (b): Time-dependent m_F distribution for π and $\sigma_\pm$ transitions, respectively. (c): Normalised transmission curve, which is identical for both polarisation settings.

1.5 Total and hyperfine state changing photon scattering

In the last section, I assumed that a sufficiently strong repumper is applied at all times, justifying a treatment of the $|F = 4\rangle$ and $|F' = 5\rangle$ manifolds only. In chapter 2, I will present quantum-nondemolition (QND) measurements [48–50] of the atomic hyperfine state utilising the cavity transmission. For this state detection a repumper must not be applied and I will discuss that the "quality" of the QND-measurement is limited by state-changing photon scattering, because after a finite time of some milliseconds the atomic state is changed due to our measurement. In this section, I will discuss how the rate of total and hyperfine-state-changing scattering is determined.

1.5.1 Total scattering

One of the long-term goals pursued in this experiment is the creation of entangled states of two atoms simultaneously coupled to the cavity field. In this context, the total scattering rate should be as low as possible to avoid decoherence. Photon scattering also plays a role for cavity-cooling and -heating (see chapter 3).

In general, the scattering rate for a two-level system is given by

$$R_{\text{scatt}} = 2\gamma\rho_{ee} \,, \tag{1.59}$$

where ρ_{ee} is the excited state population. Let us first consider the result for ρ_{ee} for a two-level atom in free space obtained from the optical Bloch equations, which is [51]

$$\rho_{ee} = \frac{(\Omega/(2\gamma))^2}{1 + 4(\Delta/(2\gamma))^2 + 2(\Omega/(2\gamma))^2} \,, \tag{1.60}$$

where Ω is the Rabi-frequency for the incident light. Making the substitutions $\Omega \to 2g\sqrt{n_p}$ and $\Delta \to \Delta_{pa}$ we have

$$\rho_{ee} = \frac{g^2}{\gamma^2 + \Delta_{pa}^2 + 2g^2 n_p}\, n_p \,. \tag{1.61}$$

In the weak excitation regime, the third term of the denominator can be neglected, thus the excited state population is

$$\rho_{ee} = \frac{g^2}{\gamma^2 + \Delta_{pa}^2}\, n_p \,. \tag{1.62}$$

The excited state population $\rho_{ee} = \langle \sigma^\dagger \sigma \rangle$ in the weak excitation regime can also be directly inferred from (1.31):

$$\rho_{ee} = \langle \sigma^\dagger \sigma \rangle = \langle X_4 \rangle^{(0)} = \frac{g^2}{\gamma^2 + \Delta_{pa}^2}\, n_p \,. \tag{1.63}$$

The total scattering rate thus reads

$$R_{\text{scatt,tot}} = \frac{2g^2\gamma}{\gamma^2 + \Delta_{pa}^2} n_p \,. \tag{1.64}$$

With the substitution $\Omega \to 2g\sqrt{n_p}$, also the saturation parameter, defined as $S = I/I_{\text{sat}} = \Omega^2/(2\gamma^2)$, can be formulated in terms of the intracavity photon number, namely

$$S = \frac{2g^2}{\gamma^2}\, n_p = \frac{n_p}{n_{\text{cr}}} \,. \tag{1.65}$$

So for $n_p = n_{\text{cr}}$, the saturation parameter is equal to one, but (1.63) and (1.64) are only valid for $S \ll 1$. To estimate the total photon scattering rate from a measured count rate R_{D} in an experiment, n_p can be inferred according to (1.39).

For measurements where the detuning Δ_{ca} is varied, we usually keep the count rate $R_{\text{D},0}$ for the empty cavity on resonance and thus $n_{p,0}$ constant.[3] To assess the dependence of $R_{\text{scatt,tot}}$ on the detuning for this special case, n_p can be replaced by $\bar{T}\, n_{p,0}$. The analytical expression for the usual case that the probe laser is resonant with the empty cavity, i.e. $\Delta_{pc} = 0 \Rightarrow \Delta_{pa} = \Delta_{ca}$, is then given by

$$\begin{aligned} R_{\text{scatt,tot}}^{\Delta_{pc}=0}(\Delta_{ca}, g) &= \frac{2g^2\gamma}{\gamma^2 + \Delta_{ca}^2} \bar{T}^{\Delta_{pc}=0}(\Delta_{ca}, g)\, n_{p,0} \\ &\overset{(1.34)}{=} \frac{2g^2/\gamma}{[1 + g^2/(\kappa\gamma)]^2 + (\Delta_{ca}/\gamma)^2}\, n_{p,0} \\ &= \frac{4\kappa C_1}{(1 + 2C_1)^2 + (\Delta_{ca}/\gamma)^2}\, n_{p,0} \,. \end{aligned} \tag{1.66}$$

Fig. 1.10 shows the total scattering rate as a function of detuning for our experimental parameters. Compared to the situation in free space, the scattering rate decreases only very slowly with increasing detuning. This is due to two competing effects: The scattering rate decreases with $1/\Delta^2$ for a fixed intensity,

[3] In this context the index "0" always indicates a quantity for an empty cavity ($g = 0$) and $\omega_p = \omega_c$.

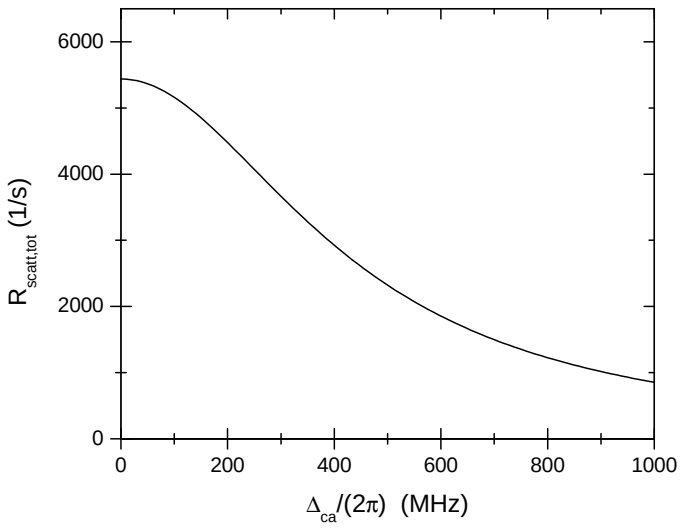

Figure 1.10: Total scattering rate as a function of detuning Δ_{ca} calculated for an empty cavity count rate of $R_{D,0} = 20\,\mathrm{ms}^{-1}$, corresponding to $n_{p,0} = 0.18$, and $(g, \kappa, \gamma)/(2\pi) = (13.1, 0.4, 2.6)$ MHz.

but the intracavity intensity approaches the empty cavity level for increasing detuning and is strongly suppressed for $\Delta_{ca} \to 0$.

The expression for the total scattering rate (1.64) is based on a two-level model. Close to resonance, this is justified because the contribution of the $|F = 4\rangle \to |F' = 4\rangle$ transition is much smaller than that of the $|F = 4\rangle \to |F' = 5\rangle$ transition because of the $1/\Delta_{ca}^2$ dependence of the scattering rate. But for $\Delta_{ca} = \Delta_{pa} = 2\pi \times 500\,\mathrm{MHz}$, a detuning of $\omega_p - \omega_{4,4'} = 2\pi \times 750\,\mathrm{MHz}$ means that scattering from this channel is almost half as likely, since $(500\,\mathrm{MHz}/750\,\mathrm{MHz})^2 = 0.44$. Therefore the real total scattering rate is underestimated by the two level approximation for large detunings.

For planned experiments involving the creation of entangled states, the probability p_{scatt} to scatter a photon during the measurement time Δt_m is an important quantity, since photon scattering is a cause of decoherence. From fig. 1.10 one might conclude that going to a higher detuning is advantageous to minimise p_{scatt} . The implications of the total scattering in terms of decoherence in a probabilistic entanglement scheme [17] are discussed in detail in [30]. An important outcome is that for $\Delta_{pa} \gg \gamma$ the signal to noise ratio for a QND measurement of the atomic state, as presented in chapter 2, is connected to the scattering probability by

$$\mathrm{SNR}^2 = \alpha p_{\mathrm{scatt}} \ , \alpha = \frac{\eta g^2}{2\kappa\gamma} = \eta C_1 = C_{1,\mathrm{eff}} \ , \tag{1.67}$$

where $\eta := \eta_{\mathrm{det}}\,\eta_{\mathrm{cav}}$ and $C_{1,\mathrm{eff}}$ is the effective one-atom cooperativity, including experimental imperfections. So for a fixed SNR, the scattering probability p_{scatt} is *independent* of Δ_{pa}. This is because for higher detunings, the number of detected photons must be increased accordingly to obtain the same signal to noise ratio.

1.5.2 Inelastic Raman scattering

For the processes studied in chapter 2, the relevant quantity is not the total scattering rate, but the rate of hyperfine state changing scattering events which causes the atom's state to change from $|F=4\rangle$ to $|F=3\rangle$ via an excited state. Thus in the following I will discuss how to calculate this rate taking multiple excited levels into account.

Off-resonant spontaneous scattering is a two-photon process, after which the atom can either be in the same or a different internal state, corresponding to elastic Rayleigh or inelastic Raman scattering, respectively. This process is of general interest in terms of hyperfine coherence [52] and the scattering rate can be calculated using the Kramers-Heisenberg formula, see e.g. [51]. Hyperfine-state relaxation for Rubidium was treated in [53], and I will follow the notation used in that reference. In this section, inelastic scattering always refers to a hyperfine state changing transition from $|F=4\rangle$ to $|F=3\rangle$.

Kramers-Heisenberg-formula

The rate of spontaneous Raman transitions from one hyperfine ground state $|F, m_F\rangle$ to another ground state $|F'', m_F''\rangle$ via a number of intermediate states $|F', m_F'\rangle$ is given by

$$\Gamma_{F,m_F\to F'',m_F''} = \frac{3\pi c^2\omega_L^3 I}{2\hbar d_{4,5'}^4}\left|\frac{a^{(1/2)}_{F,m_F\to F'',m_F''}}{\Delta_{1/2}} + \frac{a^{(3/2)}_{F,m_F\to F'',m_F''}}{\Delta_{3/2}}\right|^2 , \tag{1.68}$$

where $\Delta_{J'} = \omega_L - \omega_{J'}$ and

$$a^{(J')}_{F,m_F\to F'',m_F''} = \frac{\Gamma_{J'}}{\omega_{J'}^3}\sum_{q,F',m_F'}\langle F'', m_F''|d_q|F', m_F'\rangle\langle F', m_F'|\mathbf{d}\cdot\mathbf{e}_L|F, m_F\rangle \ . \tag{1.69}$$

Here $\mathbf{d}$ is the electric dipole operator, d_q are its spherical components with $q = -1, 0, 1$ for σ_-, π, and σ_+ transitions, respectively, $\mathbf{e}_L$ is the unit polarisation vector of the incident light and ω_L its frequency, $\omega_{J'}$ and $\Gamma_{J'}$ are the transition frequencies and spontaneous decay rates of the corresponding $6^2P_{J'}$ states, and $d_{4,5'}$ is the dipole matrix element for the strongest transition, i.e. $d_{4,5'} = \langle F = 4, m_F = 4|d_1|F' = 5, m'_F = 5\rangle$.

In our case, the laser causing the scattering is the probe laser, so $\omega_L = \omega_p$, which is close to resonance with the Cs D_2 line within one GHz. Thus $\Delta_{1/2} \gg \Delta_{3/2}$, which means the first term in the sum can be neglected. Because of the relatively small detuning Δ_{pa} of at most a few hundred MHz, we can set $\omega_p = \omega_{3/2} = \omega_{D_2} = 2\pi \times 351.7\,\mathrm{THz}$ in the prefactor. In (1.68), the detuning in the numerator depends only on J', but since in our case the detuning is comparable to the hyperfine splitting of the excited states, the expression is extended to contain the F'-dependent detunings $\omega_p - \omega_{F'}$ and reads

$$\Gamma_{F,m_F\to F'',m''_F} = \frac{3\pi c^2 I_p \Gamma_{3/2}^2}{2\hbar d_{4,5'}^4 \omega_{D_2}^3} \left| \sum_{q,F',m'_F} \frac{\langle F'', m''_F|d_q|F', m'_F\rangle\langle F', m'_F|\mathbf{d}\cdot\mathbf{e}_p|F, m_F\rangle}{\omega_p - \omega_{F'}} \right|^2 . \tag{1.70}$$

Another form is also often found, which results from the replacement

$$\Gamma = \frac{d_{4,5'}^2 \omega_{D_2}^3}{3\pi\varepsilon_0\hbar c^3} , \tag{1.71}$$

where $\Gamma \equiv \Gamma_{3/2} = 2\pi \times 5.22\,\mathrm{MHz}$, yielding

$$\Gamma_{F,m_F\to F'',m''_F} = \frac{I_p \Gamma}{2\hbar^2 c\varepsilon_0 d_{4,5'}^2} \left| \sum_{q,F',m'_F} \frac{\langle F'', m''_F|d_q|F', m'_F\rangle\langle F', m'_F|\mathbf{d}\cdot\mathbf{e}_p|F, m_F\rangle}{\omega_p - \omega_{F'}} \right|^2 . \tag{1.72}$$

In calculating absolute numbers for scattering rates, one has to take care of the definition and normalisation of the matrix elements $d_{4,5'}$ and d_q. D.A. Steck [54] defines the matrix elements as multiples of the so called reduced matrix element $\langle J = 1/2|\,|er|\,|J' = 3/2\rangle = 4.484ea_0$, and with this normalisation the matrix element for the cycling transition is $\langle 4, 4|\,d_{+1}\,|5', 5'\rangle = d_{4,5'} = \sqrt{1/2} \times 4.484ea_0$. On the other hand, the matrix elements are often used as dimensionless numbers with $\langle 4, 4|\,d_{+1}\,|5', 5'\rangle = 1$, cf. section 1.4.2. The form (1.70) has the advantage that matrix elements in the pre-factor and the sum appear at the same power, so both conventions work if they are used consistently.

Calculation for our experimental parameters

The Kramers-Heisenberg formula as presented above in (1.68) describes the scattering process from *one* initial state to *one* final state. In our case, we are interested in the rate of transitions from *any* sublevel within the $|F = 4\rangle$ manifold into the $|F'' = 3\rangle$ manifold.[4] The total *inelastic* scattering rate is therefore

$$R_{\text{scatt,inel}} = \sum_{m_F=-4}^{4} P(m_F) \cdot \Gamma_{4,m_F \to 3'',m''_F} \,, \tag{1.73}$$

where the distribution over the m_F states $P(m_F)$ was calculated in section 1.4. The physical process of Raman scattering is independent of how a quantisation axis is chosen and I will describe the problem in a coordinate system where $\mathbf{E}_p \parallel \mathbf{QA}$, i.e. the probe laser induces π transitions. The transition rate from one initial state $|F = 4, m_F\rangle$ into the $|F'' = 3\rangle$ manifold is given by

$$\Gamma_{4,m_F \to 3'',m''_F} = A \sum_{q=-1}^{1} \left| \sum_{F'=3,4} M(q, F') \right|^2 \,, \tag{1.74}$$

$$M(q, F') = \frac{\langle 3, m''_F |\, d_q \,| F', m'_F \rangle \;\langle F', m'_F |\, d_0 \,| 4, m_F \rangle}{\omega_p - \omega_{F'}} \,, \tag{1.75}$$

where $m'_F = m_F$ (π-excitation), $m''_F = m'_F + q$, and q parameterises the polarisation of the scattered photon, thus paths leading to the same final state $|F'' = 3, m''_F\rangle$ are added up coherently. The amplitude A was derived to be

$$A = \frac{3\pi c^2 \Gamma^2}{2\hbar d_{4,5'}^4 \omega_{D_2}^3} I_p \,. \tag{1.76}$$

For the usual case of the probe laser being initially resonant with the cavity ($\Delta_{pc} = 0$), the intensity I_p is calculated as

$$I_p(\Delta_{ca}) = I_{p,0}\, \bar{T}^{\Delta_{pc}=0}(\Delta_{ca}, g_{\max}) \,, \tag{1.77}$$

i.e. using the two-level result (1.34) with $g_{\max} = 2\pi \times 13.1\,\text{MHz}$. I assume that the atom is located at an antinode of the standing wave, thus the intensity for the empty cavity $I_{p,0} = I_{\text{sw,max}}$ is related to the corresponding count rate $R_{\text{D},0}$ by (1.40).

Fig. 1.11 shows the state changing scattering rate as a function of detuning. The striking difference compared to the total scattering in fig. 1.10 is that

[4] The notation F'' for the lower ground state is only used in the context of this section. Otherwise the two ground states are labelled by $|F = 3\rangle$ and $|F = 4\rangle$, respectively

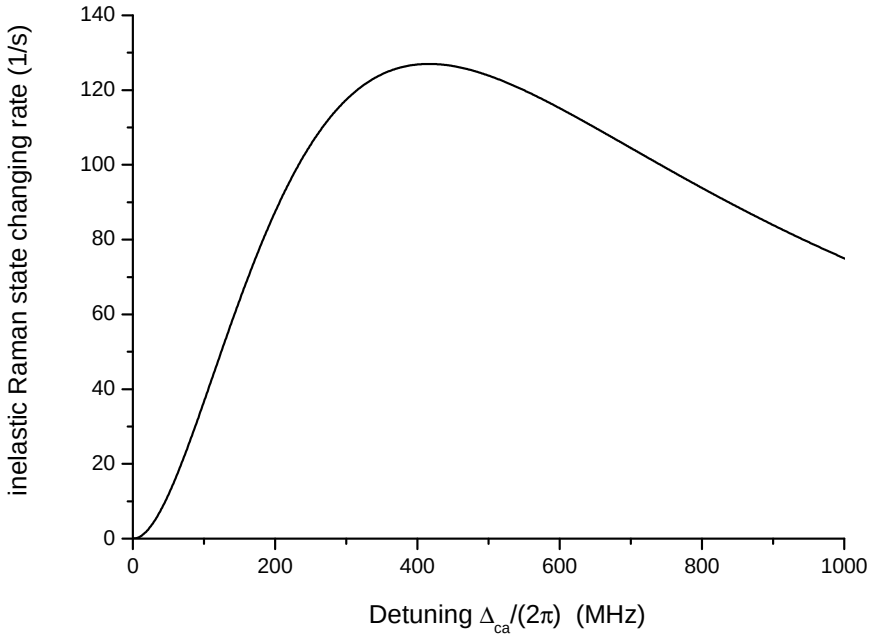

Figure 1.11: Inelastic hyperfine state changing scattering rate as a function of detuning Δ_{pa} calculated for $R_{\mathrm{D},0} = 20/\mathrm{ms}$ and $(g, \kappa, \gamma)/(2\pi) = (13.1, 0.4, 2.6)\,\mathrm{MHz}$. Δ_{ca} is the detuning from the $|F = 4\rangle \rightarrow |F' = 5\rangle$ transition.

it approaches zero towards smaller detunings. Close to resonance, mainly the $|F' = 5\rangle$ state is excited, but from there decay to the lower ground state $|F = 3\rangle$ is not possible, thus the *total* scattering rate has its maximum for $\Delta_{ca} = 0$ and falls off slowly for higher detunings, but the *state changing* scattering rate rises to a maximum at around $\Delta_{ca} = 2\pi \times 420\,\mathrm{MHz}$ for our parameters and then also falls off. In chapter 2 I will show that this prediction was also observed experimentally and I will discuss the implications on measuring the atomic state.

The outcome of the theoretical considerations in this and the preceding section as well as the numerical simulations provide an understanding of the physical effects and deliver reasonable estimates on the ground state population, the timescale of probe laser induced optical pumping and the scattering rates. I will conclude this chapter by presenting a measurement of the effective coupling strength, which is inferred from the averaged normalised transmission.

1.6 Effective atom-cavity coupling

As can be seen from (1.33), for fixed and known detunings the transmission level is determined by the coupling strength g. So by measuring $\bar{T}(t)$, we obtain information about both the average coupling strength and its variation.

1.6.1 Single atom transmission signal

To measure the transmission, we first prepare a single atom in the dipole trap using the number-locked loading technique [31]. After determining the position of the atom from an image, the atom is transported into the cavity centre. The probe laser is switched on before the transport and the transmission level for the empty cavity is set to a predetermined count rate at the detector $R_{\mathrm{D},0}$ of typically 20 to 30 counts/ms by a computer-controlled Pockels-cell as a part of the optical path of the probe laser beam. In all the measurements presented here and in chapter 2 the probe laser is in resonance with the empty cavity, i.e. $\Delta_{pc} = 0 \Rightarrow \Delta_{ca} = \Delta_{pa}$. As the atom enters the cavity, the transmission drops because the probe laser is no longer resonant with the dressed states. After a fixed time of usually several hundred milliseconds the atom is removed from the cavity and the transmission rises to its initial value.

Figure 1.12 shows a typical transmission trace for one atom coupled to the cavity. The photon counts are binned in 1 ms time intervals, which is a compromise between having a sufficient signal-to-noise ratio and being able to observe dynamical processes. The graph shows that the transmission is obviously suppressed, but the fluctuations in the count rate exceed shot noise. Since the detunings are fixed, this can be attributed to a variation of the coupling strength g, caused by motion of the atom. In chapter 3 I will discuss approaches to improve the localisation and thereby the coupling stability.

1.6.2 Transmission level as a function of cavity-atom detuning

The average transmission level was measured for a wide range of detunings Δ_{ca}, see fig. 1.13. The data shows the count rate with an atom coupled to the cavity normalised to the empty-cavity signal:

$$\bar{T}_{\mathrm{av}}^{(\mathrm{exp})}(\Delta_{ca}) = \frac{R_{\mathrm{D}}\left(\Delta_{ca}, g\right)}{R_{\mathrm{D},0}} \,, \tag{1.78}$$

where $R_{\mathrm{D},0} = 30\,/\mathrm{ms}$ was fixed for all detunings. The atomic frequency ω_a is always meant to be $\omega_{4\to 5'}$, and the detunings also refer to this transition, including the AC-Stark shift caused by the YAG-laser. The measured data can

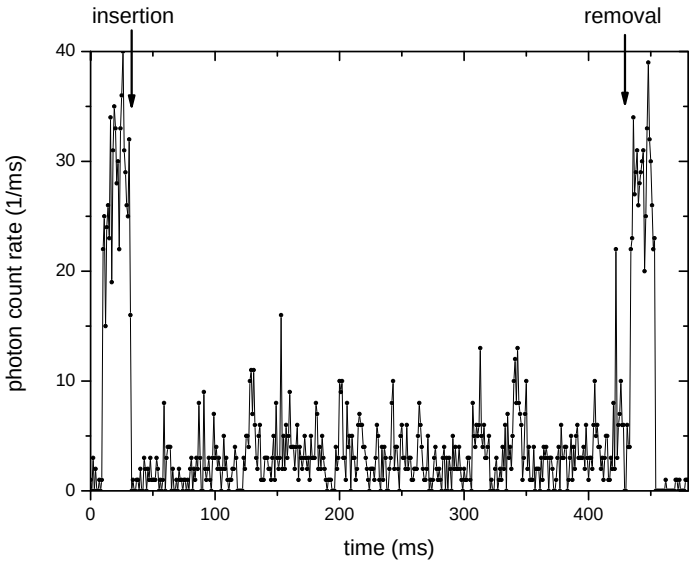

Figure 1.12: Probe laser transmission signal for one atom coupled to the cavity for 400 ms. The arrows indicate the points in time of insertion and removal, respectively. The photon counts are binned in 1 ms time intervals. The cavity-atom detuning is $\Delta_{ca} = 2\pi \times 34\,\mathrm{MHz}$.

be compared to the theoretical model of the normalised transmission for $\Delta_{pc} = 0$, see (1.34). In section 1.4.2 it was shown that irrespective of the polarisation setting, the two-level formula for the transmission dependence is still valid with a coupling strength of $g_{\max} = 2\pi \times 13.1\,\mathrm{MHz}$.

For detunings $\Delta_{ca}/(2\pi) \gtrsim 200\,\mathrm{MHz}$, the data points are well described by an effective coupling strength $g_{\mathrm{eff}}/(2\pi) \approx 9\,\mathrm{MHz}$, whereas for $\Delta_{ca}/(2\pi) \lesssim 100\,\mathrm{MHz}$ the data suggest a smaller coupling strength. The lack of data points in the range of detunings from 100 to 160 MHz is owing to strongly fluctuating transmission signals, which prohibited a reliable value for the average transmission to be determined. This behaviour was observed repeatedly in this detuning range.

The main reason for the coupling to be lower than the calculated maximum of $g_{\max} = 2\pi \times 13.1\,\mathrm{MHz}$ is the atomic motion, because averaging due to different Zeeman-levels is already included in this value of g. The coupling strength $g(\mathbf{r})$ follows the mode function, see (1.17), so when the atom moves, $g(\mathbf{r})$ changes and so does the transmission. The output flux $\Phi_{\mathrm{out}}(t)$ follows the coupling variation on the timescale of the photon lifetime $\tau_{\mathrm{cav}} = 1/(2\kappa) = 200\,\mathrm{ns}$, which can be considered instantaneous for our purposes, but the measured transmission $\bar{T}$ is the result of two averaging processes. From many single-shot traces like the one

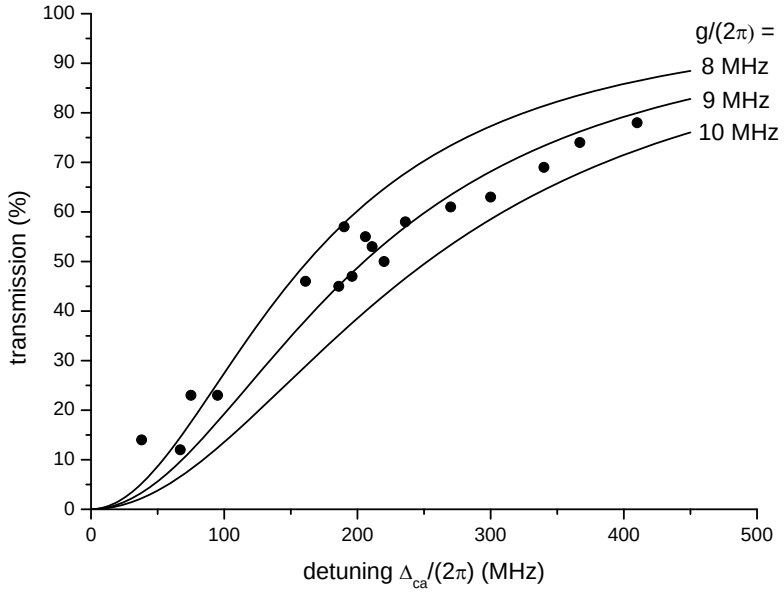

Figure 1.13: Normalised averaged transmission for one atom coupled to the cavity as a function of cavity-atom detuning Δ_{ca}. The solid lines are calculated according to (1.34) for different values of g.

shown in fig. 1.12 we get an ensemble-average, the mean value of which, averaged over the time of the whole trace (400 ms), is the transmission data shown in fig. 1.13.

The theoretical two-level model for $\bar{T}$, cf. (1.34), only deals with a constant coupling g. So in saying the data can be described by an *effective* coupling strength of $g_{\text{eff}}/(2\pi) \approx 9\,\text{MHz}$, this means means a stationary atom experiencing a coupling g_{eff} would result in the same normalised transmission level we obtain after the two averaging processes:

$$\bar{T}(g_{\text{eff}}) = \left\langle \left\langle \bar{T}\big(g(\mathbf{r}(t))\big) \right\rangle_{\text{ensemble}} \right\rangle_{\text{time}} =: \bar{T}_{\text{av}} \tag{1.79}$$

So far it was not possible to improve the effective coupling strength g_{eff} by changing experimental conditions, so $2\pi \times 9\,\text{MHz}$ will be used as a realistic estimate for g_{eff} henceforth. The value g_{eff} contains no information about the physical processes leading to this reduction in coupling strength, it subsumes all possible effects that could lead to a lower coupling. In the following, I will discuss a physical model taking the limited confinement of the atom into account.

1.6.3 Effect of thermal motion on the averaged transmission

As discussed in section 1.3.2, in the direction perpendicular to the cavity axis and the conveyor belt, i.e. along x, the atom is only weakly confined by the relatively shallow FORT, whereas motion along the conveyor belt axis can be neglected. Along the cavity axis (z), the atom can be inserted into different trapping sites for each realisation of an experimental sequence. The local coupling strength is therefore

$$g(x,z) = g_{\max} \exp\left(-\frac{x^2}{w_{0,\mathrm{cav}}^2}\right)\left|\cos\left(\frac{\pi}{d_{\mathrm{beat}}}z\right)\right| , \tag{1.80}$$

where here the variation of $g(z)$ is expressed as a continuous function for the purpose of uniform numerical implementation, see (1.47). The position of the atom is assumed to follow a 2-D Gaussian probability density function in the $x-z$-plane of the form

$$f(x,z,\sigma_x,\sigma_z) = \frac{1}{2\pi\sigma_x\sigma_z}\exp\left(-\frac{x^2}{2\sigma_x^2}-\frac{z^2}{2\sigma_z^2}\right). \tag{1.81}$$

The averaged normalised transmission is then given by

$$\bar{T}_{\mathrm{av}}\left(\Delta_{ca},\sigma_x,\sigma_z\right) = \iint_{-\infty}^{+\infty} \frac{\kappa^2(\Delta_{ca}^2+\gamma^2)}{(\gamma\kappa+g(x,z)^2)^2+(\Delta_{ca}\kappa)^2} f(x,z,\sigma_x,\sigma_z)dx\,dz\ . \tag{1.82}$$

In figure 1.14 the measured data points $\bar{T}_{\mathrm{av}}^{(\mathrm{exp})}(\Delta_{ca})$ are presented again, along with the numerical integration of $\bar{T}_{\mathrm{av}}\left(\Delta_{ca},\sigma_x,\sigma_z\right)$ for a maximum coupling of $g_{\max} = 2\pi \times 13.1\,\mathrm{MHz}$, and Gaussian widths of $\sigma_x = 11.7\,\mu\mathrm{m}$ and $\sigma_z = 9.5\,\mu\mathrm{m}$, which were determined from a least-squares fit to the data. Both parameters were varied independently, because σ_z characterises the distribution before the atoms are inserted, given by the temperature in the conveyor belt at the end of the transport, whereas σ_x is given by a potentially different equilibrium temperature inside the cavity. To illustrate how a different value of σ_x and σ_z affects $\bar{T}_{\mathrm{av}}\left(\Delta_{ca},\sigma_x,\sigma_z\right)$, also curves for a width of $\sigma_{x,z} \pm 1\,\mu\mathrm{m}$ are plotted in fig. 1.14. Since all except of two data points are within this range, $\pm 1\,\mu\mathrm{m}$ is a reasonable estimate for the accuracy of the values for $\sigma_{x,y}$ determined by the least squares fit.

If the radial oscillation frequency Ω_{rad} in the dipole trap and the width of the spatial distribution σ are known, the temperature is given by [26]

$$T = \frac{m_{\mathrm{Cs}}\,\Omega_{\mathrm{rad}}^2\,\sigma^2}{k_B}\ . \tag{1.83}$$

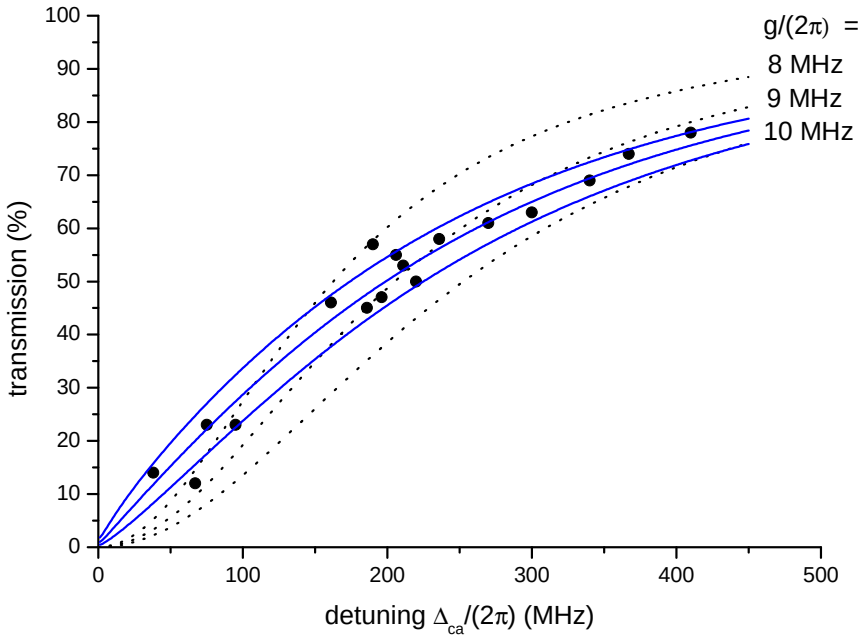

Figure 1.14: Measured averaged transmission (black dots) as a function of detuning, showing the same data as fig. 1.13. The black dotted lines are calculated according to (1.34) for different values of g_{eff} for an atom at rest. The blue solid lines show the averaged transmission $\bar{T}_{\text{av}}(\Delta_{ca}, \sigma_x, \sigma_z)$, where the centre line is calculated for the fit results $\sigma_x = 11.7\,\mu\text{m}$ and $\sigma_z = 9.5\,\mu\text{m}$ for $g_{\max} = 2\pi \times 13.1\,\text{MHz}$, and the upper (lower) curve corresponds to a larger (smaller) spatial width of $\sigma_{x,z} + (-)1\,\mu\text{m}$.

In [15], $\Omega_{\text{rad}}/(2\pi)$ was measured to be 1.6 kHz, thus yielding here temperatures of $T_{\text{z}} = 145\,\mu\text{K}$ and $T_{\text{x}} = 220\,\mu\text{K}$ for $\sigma = \sigma_z$ and $\sigma = \sigma_x$, respectively. These temperatures are higher than previously measured temperatures of atoms stored in the FORT and seem unrealistically high. One reason is that here the observed transmission is solely attributed to thermal motion, thereby including also other possible effects which could lead to a lower coupling strength.

However, a higher average temperature inside the cavity is conceivable and could be due to parametric heating by the lock laser. Residual fluctuations of the cavity resonance frequency with respect to the lock laser frequency translate into intensity variations of the intra cavity lock laser light and thus its dipole potential. This assumption is confirmed by our experience that the settings of the control loop used to stabilise the cavity onto the lock laser are critical for the lifetime of atoms coupled to the cavity.

Fig. 1.14 shows that two different models can be utilised to describe the measured data reasonably well, namely the two-level model for a stationary atom with a reduced coupling strength g_{eff} and the thermal model with the theoretically determined maximum coupling strength $g_{\max}$ and a Gaussian spatial distribution for the motion along x and z. Using g_{eff} allows us to draw upon results derived for an ideal two-level system, e.g. when doing first estimates of the feasibility of entanglement schemes, without taking the motion of the atom into account. The second model provides additional physical insight, but it attributes the fact, that the transmission is higher than for the ideal case, to one effect only.

In chapter 3 I will come back to the question of how to control the external dynamics. There I will also explain the process of *cavity cooling* which is the reason why we can observe an atom coupled to the cavity for several hundred milliseconds at all.

2 Internal spin-dynamics of one and two atoms

In this chapter I will explain how the atom-cavity interaction can be used to nondestructively measure the spin-state of the atom. This technique is used to study quantum jumps of one and two atoms.

2.1 Nondestructive state detection

The nondestructive detection of the internal state of an atom is of general interest for all our current and planned experiments, especially for creating entangled states. In the terminology of quantum information, in our system the two long-lived groundstates $|F = 3\rangle$ and $|F = 4\rangle$ serve as qubit states, cf. the work on realising a quantum register in [27,55]. In order to detect the state, a "push-out" technique was successfully applied in our group in past experiments where the atoms were stored and manipulated in the dipole trap. There a laser resonant with the $|F = 4\rangle \rightarrow |F' = 5\rangle$ transition was applied to an array of atoms, removing atoms in $|F = 4\rangle$ from the trap, without affecting atoms in $|F = 3\rangle$. Taking an ICCD image of the remaining atoms and comparing it with an earlier image of all atoms, it was then possible to spatially detect the state of each atom. This method has the obvious disadvantage that it is "destructive" in the sense that atoms in $|F = 4\rangle$ are lost.

For the coupled atom-cavity system we detect the atomic state by tuning the cavity close to the $|F = 4\rangle \rightarrow |F' = 5\rangle$ transition, where only an atom in the $|F = 4\rangle$ state changes the transmission, while an atom in $|F = 3\rangle$ is so far detuned (around 9.2 GHz) that it effectively decouples from the system and does not influence the cavity transmission [19], see fig. 2.1. If the probe laser was tuned to resonance with the empty cavity before, an atom in $|F = 4\rangle$ inserted into the cavity causes a reduction in the transmission, see fig. 1.12. This state detection technique works only if there is no repumper applied, which would always bring an atom in $|F = 3\rangle$ back to the $|F = 4\rangle \rightarrow |F' = 5\rangle$ cycle.

Clearly this state detection method relies on the fact that the change in transmission is detectable. So if the detuning is too large, the signal to noise ratio gets worse because the transmission change gets smaller, see fig. 1.13. Likewise the coupling g has to be sufficiently strong, because from the transmission the

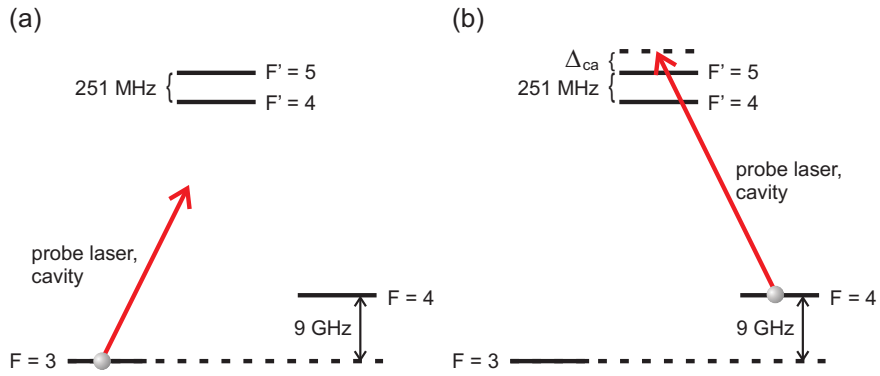

Figure 2.1: Simplified Cs level scheme. (a) An atom in $|F = 3\rangle$ is so far detuned from the cavity resonance that it does not alter its transmission. (b) If the atom is in $|F = 4\rangle$, it changes the transmission, depending on Δ_{ca} and g.

situation $g = 0$ can not be distinguished from an atom in $|F = 3\rangle$ or no atom in the cavity at all. To experimentally check whether an atom is in $|F = 3\rangle$ or it was lost from the trap, we can always switch the repumper on again. If these conditions are met and one coupled atom reduces the transmission sufficiently, the atomic hyperfine spin state can be deduced from the transmission within 1 ms. This measurement is nondestructive in the sense, that the atom remains in the dipole trap irrespective of its state.

If the state detection technique described above gave the same result for an unlimited series of state measurements, it would be a perfect projective quantum nondemolition (QND) measurement [48–50]. However, in our situation the same laser that we use to detect the atomic state (the probe laser) can change it via inelastic Raman scattering, see section 1.5.2. The experimental challenge is to measure the state faster than $R^{-1}_{\mathrm{scatt,inel}}$ with a high fidelity.

2.2 Single atom quantum jumps

2.2.1 Measurement technique

To experimentally determine $R_{\mathrm{scatt,inel}}$, compare it with the theoretical results obtained in section 1.5.2, and identify optimum experimental conditions, we performed the following measurement: An atom, optically pumped into $|F = 4\rangle$ by switching the MOT repumper off after the MOT cooling laser, is transported into the cavity centre. The probe laser is initially set to be resonant with the cavity, but in contrast to the continuous observation presented in fig. 1.12, in this case *no repumper* is applied. Therefore, after some ms the atom undergoes a spontaneous Raman transition to $|F = 3\rangle$, causing an instantaneous rise in

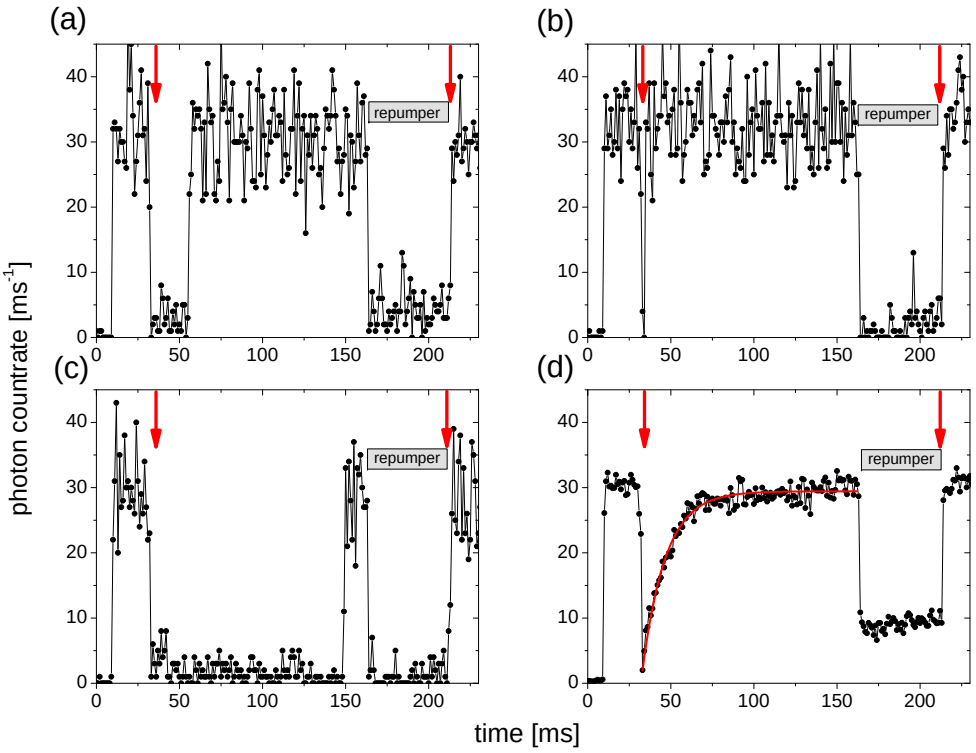

Figure 2.2: (a) to (c): Single traces of quantum jump measurements. The arrows indicate insertion and removal of an atom. At the end of the sequence, the repumper is switched on again to check that the atom was not lost. (d): Ensemble average over 31 single traces. The time R_{43}^{-1} is obtained from the exponential fit.

transmission back to the empty cavity level. This *quantum jump* was observed in trapped ions before [20–22, 56], but not in single neutral atoms. To check whether the rise in transmission is really due to a quantum jump and not caused by the atom being lost, the repumper is switched on at the end of the sequence.

Fig. 2.2 (a) to (c) show three different experimental traces. The jump occurs at a random point in time, but the jump rate is time independent. So for an ensemble average, we obtain the expected exponential curve, fig. 2.2 (d). The averaged transmission level at the end of the sequence, when the repumper is switched on, is higher than the initial drop. We attribute this to increased thermal motion, which leads to a lower effective coupling strength. This could be because the atom is not cooled by the probe laser while it is in $|F = 3\rangle$.

The time constant extracted from the exponential fit is the inverse inelastic Raman scattering rate

$$R_{43} = R_{\text{scatt,inel}} \quad , \tag{2.1}$$

where the terminology R_{43} was introduced for the rate of quantum jumps from $|F=4\rangle$ to $|F=3\rangle$. The probability that such a jump occurs during a measurement time Δt_m is given by

$$p_{\mathrm{j},4,3} = 1 - e^{-\Delta t_m R_{43}} \; . \tag{2.2}$$

We have analysed how the jump rate R_{43} depends on the cavity-atom detuning to find an optimum setting for our experiments.

2.2.2 Influence of the detuning

The scattering time R_{43}^{-1} was measured as a function of the detuning Δ_{ca} for a fixed detector count rate of $R_{\mathrm{D},0} = 20\,\mathrm{ms}^{-1}$, corresponding to a maximum intensity at the probe anti-node of $I_{\mathrm{sw,max}} = 194\,\mathrm{W\,m}^{-2}$, see (1.40). The measured data is compared with results of a calculation based on the theory presented in chapter 1, cf. (1.73) with the steady state distribution $P(m_F)$, see fig. 1.7, leading to an equivalent maximum coupling strength for a two-level model of $g_{\max} = 2\pi \times 13.1\,\mathrm{MHz}$.

A coupling strength g_{eff} smaller than $g_{\max}$, as deduced from the averaged transmission in section 1.6.3, is attributed to thermal motion of the atom. Therefore the probe laser intensity relevant for calculating the scattering rate is not $I_{\mathrm{sw,max}}\, \bar{T}^{\Delta_{pc}=0}(\Delta_{ca}, g_{\max})$, but it is subject to a spatial modulation as well. I will apply the 2D-model developed in section 1.6.3 to take this effect into account. The spatial distribution of the atom leads to a position dependent normalised transmission of the form

$$\bar{T}^{\Delta_{pc}=0}(\Delta_{ca}, x, z) = \frac{\kappa^2(\Delta_{ca}^2 + \gamma^2)}{(\gamma\kappa + g(x,z)^2)^2 + (\Delta_{ca}\kappa)^2} \; , \tag{2.3}$$

where $g(x,z)$ was defined in (1.80). In addition, the intensity for the empty cavity $I_{p,0}$ also follows the Gaussian mode profile, and since $I \propto E^2 \propto g^2$, we have

$$\frac{I_{p,0}(x,z)}{I_{\mathrm{sw,max}}} = \left(\frac{g(x,z)}{g_{\max}}\right)^2 \; , \tag{2.4}$$

leading to a spatially dependent probe intensity with one coupled atom of

$$I_p(x,z) = I_{\mathrm{sw,max}} \left(\frac{g(x,z)}{g_{\max}}\right)^2 \bar{T}^{\Delta_{pc}=0}(\Delta_{ca}, x, z) \; . \tag{2.5}$$

The averaged probe laser intensity I_{av} reads

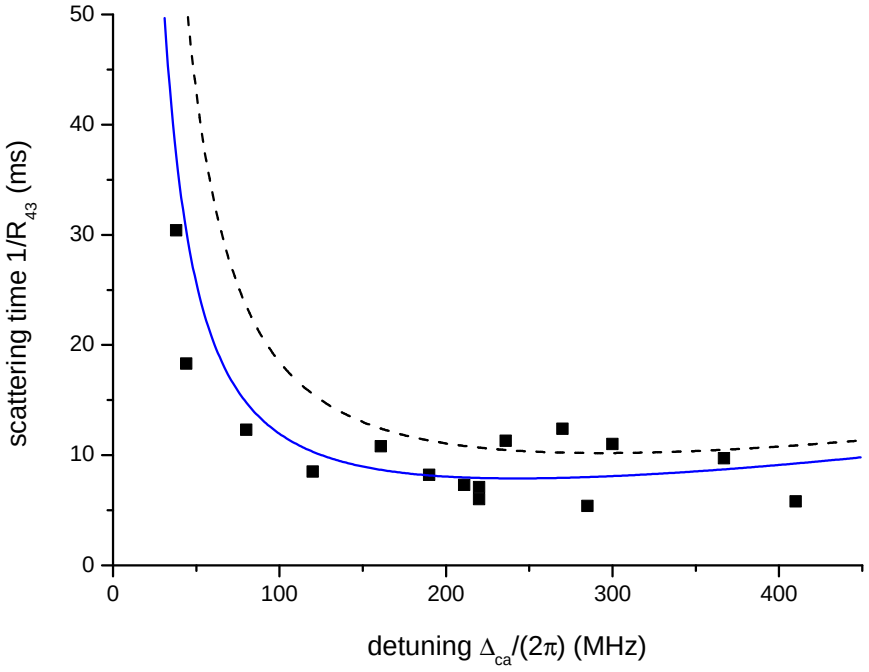

Figure 2.3: Measured scattering time R_{43}^{-1} as a function of detuning Δ_{ca} for a constant count rate $R_{\mathrm{D},0} = 20\,\mathrm{ms}^{-1}$ and with the guiding field applied perpendicular to the probe laser field. The dashed black and solid blue curves are the result of a numerical calculation with $g_{\max}/(2\pi) = 13.1\,\mathrm{MHz}$ and 11.2 MHz, respectively.

$$I_{\mathrm{p,av}}\left(\Delta_{ca}, \sigma_x, \sigma_z\right) = \int_{-\infty}^{+\infty}\!\!\int I_p(x,z) f(x,z,\sigma_x,\sigma_z) dx dz \;, \tag{2.6}$$

which is used as I_p in the factor A of the inelastic Raman scattering rate, see (1.76). In figure 2.3, the measured scattering times $R_{43}^{-1}(\Delta_{ca})$ are compared with the theoretical calculation for two different cases. The black dashed line is based on the same parameters obtained from the least squares fit in section 1.6.3, i.e. $\sigma_x = 11.7\,\mu\mathrm{m}$ and $\sigma_z = 9.5\,\mu\mathrm{m}$, and the maximum coupling was assumed to be $g_{\max} = 2\pi \times 13.1\,\mathrm{MHz}$.

The measured scattering times are mostly lower than theoretically predicted by this model. One possible reason is that the value of $g_{\max}$ is based on the equilibrium distribution $P(m_F)$, which is a result of optical pumping by the probe laser. But this pumping takes place on a millisecond timescale, see fig.

1.9, i.e. on the same order of magnitude as the quantum jump process. It is important to note that in this measurement the repumper is off already when the atoms are inserted into the cavity. Since we have no knowledge about the m_F distribution prior to the insertion into the cavity, I calculated $R_{43}^{-1}(\Delta_{ca})$ with the same values for σ_x and σ_z, but with a lower value of $\tilde{g}_{\max} = 2\pi \times 11.2\,\mathrm{MHz}$, corresponding to an equal distribution over all m_F states. The result, shown as the blue solid curve in fig. 2.3, agrees much better with the measured data.

The general tendency predicted by the theory is confirmed in both cases, i.e. the scattering time R_{43}^{-1} rises steeply for lower detunings and is almost flat for higher detunings. But especially for detunings $\Delta_{ca} > 2\pi \times 200\,\mathrm{MHz}$ the variation in the measured data is quite strong, in contrast to the transmission measurement (fig. 1.13). There are several possible explanations for this observation:

One reason ist that the analysis of the scattering time measurements depends more critical on sufficient statistics, compared to the transmission measurements, as the exponential fit only gives a reliably outcome if the ensemble-average is composed of enough single shots. Another reason could be non-optimal fibre-coupling to the detection setup. In this case the same count rate at the detector would be compatible with different intracavity intensities, which affect the jump rate directly. A third possible reason is that the cooling and heating processes vary during one measurement day and on a day-to-day basis, e.g. because of electronic noise in the servo-loop stabilising the cavity frequency. This leads to a variation in temperature and thermal motion.

Despite the variations, the values and the general characteristics of $R_{43}^{-1}(\Delta_{ca})$ predicted by theory are confirmed by the data. It shows that in this configuration of the experiment the best regime for a projective QND-measurement is close to resonance, where the scattering time is longest. A practical limitation is that stable coupling was never observed for detunings $\Delta_{ca} \lesssim 2\pi \times 30\,\mathrm{MHz}$.

2.2.3 Random telegraph signal for a single atom

In the preceding section it was shown that the probe laser transmission facilitates a nondestructive state detection method if the repumper is switched off. Finally a quantum jump from $|F = 4\rangle$ to $|F = 3\rangle$ occurs, causing the transmission to rise. In the experimental data presented in fig. 2.2, a strong repumper was switched on a the end of the sequence to check whether the atom is still present. When during this time the atom undergoes inelastic Raman transitions to $|F = 3\rangle$, it is pumped back so quickly by the repumper that this spin change is not visible at the 1 ms time resolution set by the binning time.

If the repumper is deliberately attenuated to a level at which the repumping rate R_{34} from $|F = 3\rangle$ to $|F = 4\rangle$ is comparable to R_{43}, jumps in both direction occur on a timescale of milliseconds and are thus detectable as a random

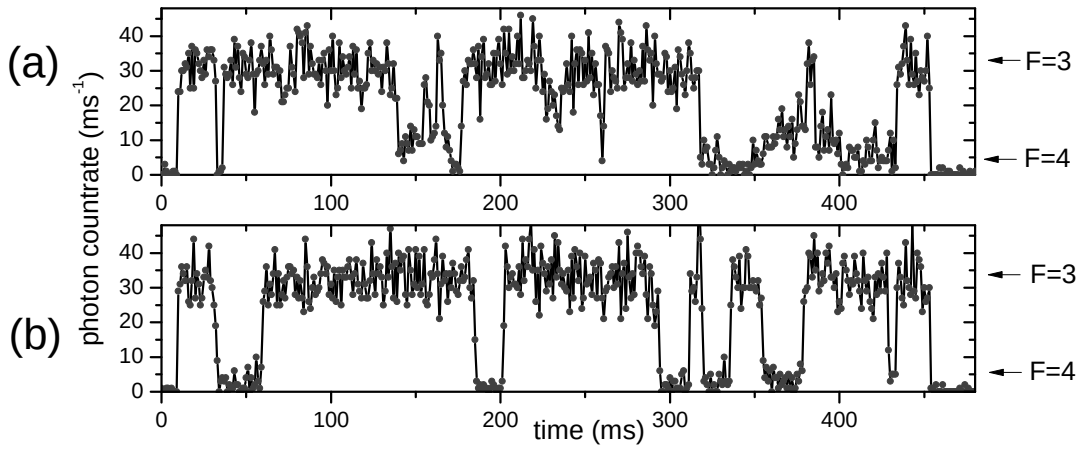

Figure 2.4: Example traces of random telegraph signals. (a) Most traces show variations of the lower transmission level. (b) In 27 out of those 348 traces, for which the atom survived the whole 400 ms observation time, the reduced transmission for an atom in $|F = 4\rangle$ remains fairly constant. The detuning is $\Delta_{ca} = 2\pi \times 38\,\mathrm{MHz}$ and the guiding magnetic field is applied along the cavity axis.

telegraph signal [20–22, 56–58].

Several hundred telegraph signals of 400 ms duration each were recorded in order to study the dynamics of quantum jumps. Two example traces are shown in fig. 2.4, differing in the variation of the lower transmission level. For most traces, the lower transmission level shows significant variations, by far exceeding the shot noise. This is due to changes in the coupling strength, which in turn are caused by thermal motion.

As will be explained in chapter 3, the probe laser itself provides cavity cooling, but an atom in $|F = 3\rangle$ is effectively decoupled from the cavity and thereby not cooled, but it is still affected by lock-laser-induced heating. It is therefore likely that after spending several milliseconds in $|F = 3\rangle$, the atom will "heat up". In less than 10% of the measured data (27 out of 348 traces), however, the observed variation of the coupling is very small. These signals show how important a stable and strong coupling is and how it directly affects the quality of our measurement.

2.2.4 State detection fidelity

To quantify how well the atomic state can be deduced from the transmission signal, two sources of errors have to be taken into account. If the two transmission levels are not well separated, an atom being in $|F = 4\rangle$ will occasionally lead to a count rate compatible with $|F = 3\rangle$ and vice versa. The other source of a measurement error occurs if the atom undergoes a quantum jump during

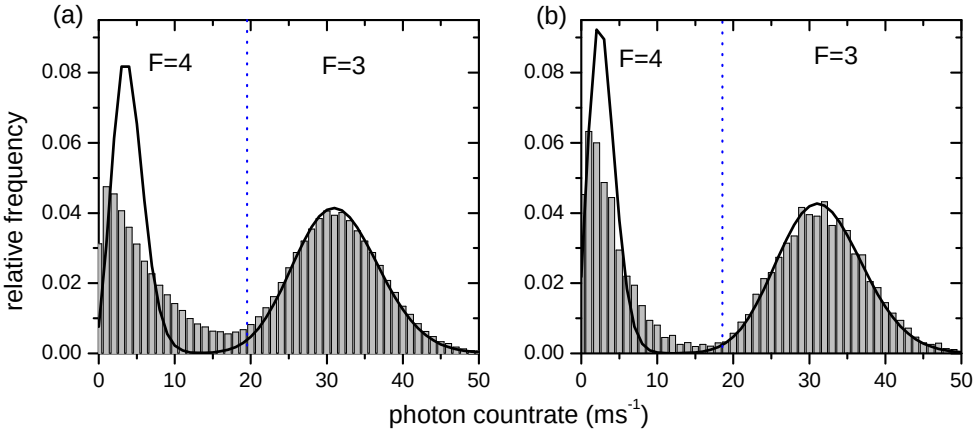

Figure 2.5: Histogram of photon counts obtained from (a) all random telegraph signals and (b) the same subset of 27 best selected shots referred to in fig. 2.4 (b). The solid lines are Poissonian fits. The vertical dashed line is a threshold minimising the overlap.

the measurement time, here 1 ms. In the following I will address both issues.

Count rate overlap

To quantify the count rate overlap, a histogram of the photon count rate is extracted from all transmission traces, see fig. 2.5 (a), and for the selected group with a small variation of the low transmission level, see (b). If the atom is in $|F = 3\rangle$, the transmission is the same as for an empty cavity and its variation is given by the photon shot noise. This can be seen by fitting the right peak of the histogram with a Poissonian distribution, which describes the data accurately.

Subtracting these counts from the total histogram results in the distribution of the photon count rate for an atom in $|F = 4\rangle$, which can again be fitted with a Poissonian distribution. The analysis of all traces shows that the left peak is significantly broader than the fit, whereas for the selected group of traces the histogram is closer to the shot noise limit. Thus the variation of g is the dominating effect that limits the signal to noise ratio.

A threshold between the count rate assigned to $|F = 3\rangle$ and $|F = 4\rangle$ is set such that the overlap between the two measured histogram peaks is minimised, see fig. 2.5. The overlap of 2.4 % in case (a) and 1.3 % in case (b) determines the probability p_{cr} of a false state detection caused by a wrong interpretation of the measured count rate. Compared to the results presented in [59], the overlap

could be reduced by about a factor of two owing to a more stable coupling and an improved detection efficiency. The latter means that the same empty cavity count rate $R_{\mathrm{D},0}$ corresponds to a lower intracavity power and thus a lower jump rate.

Jump rates

The random telegraph signals can be digitised applying the threshold obtained from the histogram, yielding a binary signal $F(t)$ where F is either 3 or 4. For the following discussion in this and the next section I introduce the notation N_4 for the number of atoms in $|F = 4\rangle$. This notation might not be obvious at this point when describing the processes involving only one atom and N_4 is either 0 or 1, but the usefulness of this terminology will become apparent when the dynamics of two atoms are discussed later in this chapter.

Let p_0 be the probability that *no* atom is in the state $|F = 4\rangle$, i.e. for the one-atom case discussed here $p_0 = 1$ means the atom is in $|F = 3\rangle$. Likewise, p_1 is the probability for an atom to be in $|F = 4\rangle$. With this notation, the rate of jumps from $|F = 4\rangle$ to $|F = 3\rangle$, labelled by R_{43} so far, is then written as R_{10} and the repumping rate R_{34} corresponds to R_{01}. The dynamics of the quantum jumps are them described by the following rate equations [56]:

$$\frac{dp_0(t)}{dt} = -R_{01}p_0(t) + R_{10}p_1(t) \tag{2.7a}$$

$$\frac{dp_1(t)}{dt} = -R_{10}p_1(t) + R_{01}p_0(t) = -\frac{dp_0(t)}{dt} \tag{2.7b}$$

The average probabilities $\bar{p}_0$ and $\bar{p}_1$ for timescales much longer than the inverse jump rates, obtained by setting $\frac{dp_0(t)}{dt} = \frac{dp_1(t)}{dt} = 0$ and using $\bar{p}_0 + \bar{p}_1 = 1$, are related to the jumprates by

$$\bar{p}_0 = \frac{R_{10}}{R_{10} + R_{01}} \tag{2.8a}$$

$$\bar{p}_1 = \frac{R_{01}}{R_{10} + R_{01}}\ . \tag{2.8b}$$

The values of $\bar{p}_0 = 58\%$ and $\bar{p}_1 = 42\%$ are extracted from the area of the right and left histogram peak, respectively (fig. 2.5 (b)). These averaged values are determined by the ratio between the rates, not by their absolute values.

To obtain R_{10} and R_{01} from the digitised random telegraph signal, the relative frequency of the dwell times T_d is analysed. The dwell times $T_{d,0}$ are the lengths of the time intervals between two quantum jumps for which $N_4 = 0$, i.e. the

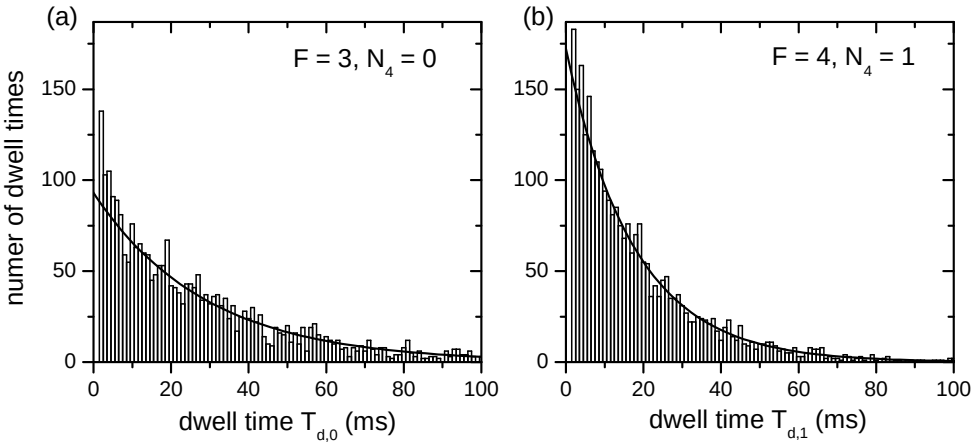

Figure 2.6: Histogram of dwell times for the atom being in (a) $|F = 3\rangle$ and (b) $|F = 4\rangle$, obtained from digitised telegraph signals of all 348 traces.

atom is in $|F = 3\rangle$ and the transmission is constantly high, and $T_{d,1}$ are the durations between two quantum jumps for which $N_4 = 1$. Assuming an atom is in $|F = 4\rangle$ at $t = 0$, i.e. $p_1(0) = 1$, the probability that no quantum jump to $|F = 3\rangle$ occurs during the time T is given by

$$p_{\mathrm{nj},1,0}\,(T) = \exp(-R_{10}T)\;, \tag{2.9}$$

where nj,1,0 means no quantum jump ("nj") from $N_4 = 1$ to $N_4 = 0$. The dwell times $T_{d,1}$, corresponding to a low transmission level, are therefore exponentially distributed with a probability density of [56]:

$$p(T_{d,1}) \propto \exp(-R_{10}T_{d,1}) \tag{2.10}$$

In analogy, the probability density of the dwell times $T_{d,0}$, when the atom is in $|F = 3\rangle$ and the transmission is high, is given by

$$p(T_{d,0}) \propto \exp(-R_{01}T_{d,0})\;. \tag{2.11}$$

The histograms of the dwell times for low and high transmission levels, computed from the digitised signals, are shown in fig. 2.6. The result of the exponential fit depends strongly on the starting point of the fitting range, but the fitted rate remains fairly constant for a lower limit of $T_d > 6\,\mathrm{ms}$, therefore shorter dwell times are excluded from the analysis. Comparing the histogram with the fit shows that the number of short dwell times is "too high", which

could be caused by measurement errors, if a change in transmission is regarded as a quantum jump, although it is only noise. The rates obtained from the fit are

$$R_{10} = (57 \pm 1)\,\mathrm{s}^{-1}\ ,\ R_{01} = (35 \pm 1)\,\mathrm{s}^{-1}\ , \tag{2.12}$$

which are confirmed by analysing the second-order correlation function of the telegraph signals, see [30]. The probabilities that state changing scattering happens during a 1 ms interval is thus

$$p_{\mathrm{j},1,0}\,(1\,\mathrm{ms}) = 1 - p_{\mathrm{nj},1,0}\,(1\,\mathrm{ms}) = 5.5\% \tag{2.13a}$$
$$p_{\mathrm{j},0,1}\,(1\,\mathrm{ms}) = 1 - p_{\mathrm{nj},0,1}\,(1\,\mathrm{ms}) = 3.4\%\ , \tag{2.13b}$$

which gives a total error probability, including the peak overlap of the count rate histogram, of

$$p_{\mathrm{err}} = \bar{p}_{\mathrm{j}} + p_{\mathrm{cr}} - \bar{p}_{\mathrm{j}}\,p_{\mathrm{cr}} = 0.069\ , \tag{2.14}$$

where the weighted jump probability $\bar{p}_{\mathrm{j}} = \bar{p}_1 p_{\mathrm{j},1,0} + \bar{p}_0 p_{\mathrm{j},0,1} = 4.6\%$ was used. The overlap error $p_{\mathrm{cr}} = 2.4\%$ was determined before from all telegraph signals. The fidelity of the state detection for a binning time of 1 ms is thus

$$F_{\mathrm{SD}}\,(1\,\mathrm{ms}) = 1 - p_{\mathrm{err}} = 93.1\%\ . \tag{2.15}$$

2.3 Spin dynamics of two atoms

So far I have presented experiments revealing the internal spin dynamics of one atom coupled to the cavity mode. Placing two atoms into the resonator leads to an effective interaction between them, mediated by the cavity field [59]. Detecting the number of atoms being in a particular state is the basis for a promising theoretical proposal on entanglement generation in CQED-systems [16, 17]. In free space, the internal atomic state evolution of a dipole-trapped ensemble of cold atoms was inferred from the phase shift of a far detuned laser beam [50], where the large number of atoms yielded a sufficiently strong signal. In a CQED experiment, already a single atom can cause a significant phase shift, if the system is in the strong coupling regime.

In the following, I will present experiments on the spin dynamics of two atoms. The state detection is again based on cavity transmission, using a variation of the method discussed in the previous section. Because the photon scattering rate during our detection time is too high, these measurements are not compatible

with entanglement generation, but they are an important step in this direction and they allow us to quantify the parameters and explore the limits of our system.

2.3.1 Counting the number of coupled atoms

In the previous section it was shown that it is possible to determine if an atom is in $|F = 3\rangle$ or $|F = 4\rangle$ based on the probe laser transmission. Without changing the experimental settings, this is not directly possible for two atoms coupled to the resonator. Both atoms in $|F = 3\rangle$, i.e. $N_4 = 0$, will lead to a transmission level $\bar{T}_0 = 1$ equal to the empty-cavity case. One atom in $|F = 4\rangle$ and one in $|F = 3\rangle$ ($N_4 = 1$) will cause the transmission $\bar{T}_1$ to drop almost to zero, cf. the one-atom case in fig. 2.4, which implies that $N_4 = 2$ is indistinguishable from $N_4 = 1$. To deduce $N_4 = 0, 1, 2$ from the corresponding transmission levels $\bar{T}_0, \bar{T}_1, \bar{T}_2$, the experimental settings have to be chosen such that one atom alone does not block the cavity transmission completely. A higher detuning Δ_{ca} causes a higher transmission $\bar{T}_1$, cf. fig. 1.13 and equation (1.34).

Variation of the detuning

In the weak excitation limit, two atoms at rest coupled with the same strength g can be theoretically described as a single atom experiencing a coupling strength $g_2 = \sqrt{2}g$ [16,17]. In the dispersive limit ($\Delta_{ca} \gg \gamma$), the transmission levels are then given by (1.35)

$$\bar{T}_1 = \frac{1}{1 + \left(\frac{g^2}{\kappa\Delta_{ca}}\right)^2}\ ,\ \bar{T}_2 = \frac{1}{1 + \left(\frac{2g^2}{\kappa\Delta_{ca}}\right)^2}\ , \tag{2.16}$$

and the level difference $\Delta\bar{T}_{12} = \bar{T}_1 - \bar{T}_2$ reaches its maximum value of 33% for $g^2/(\kappa\Delta_{ca}) = 1/\sqrt{2}$, when $\bar{T}_0$, $\bar{T}_1$, and $\bar{T}_2$ are equally spaced. The average normalised transmission $\bar{T}_2$ for two atoms coupled to the cavity was measured alongside the data already presented in fig. 1.13 for detunings $\Delta_{ca}/(2\pi) > 160\,\mathrm{MHz}$. Figure 2.7 shows that for two atoms the transmission is lower, but instead of the theoretically expected value of $\sqrt{2} \times 9\,\mathrm{MHz} = 12.7\,\mathrm{MHz}$, it is compatible with an effective coupling of $g_{\mathrm{eff}} \approx 2\pi \times 11\,\mathrm{MHz}$, i.e. about 15% less. Here 9 MHz is the effective two-level coupling strength for an atom at rest which best describes the one-atom transmission data, i.e. I do not consider the model of thermal atomic motion in this discussion.

One contribution to this discrepancy is the variation of the atomic position. In the case of one atom, the fitting-routine implemented in the image acquisition software is used to determine the initial position of the atom, which is then used to transport the atom to the cavity centre using the optical conveyor belt. The

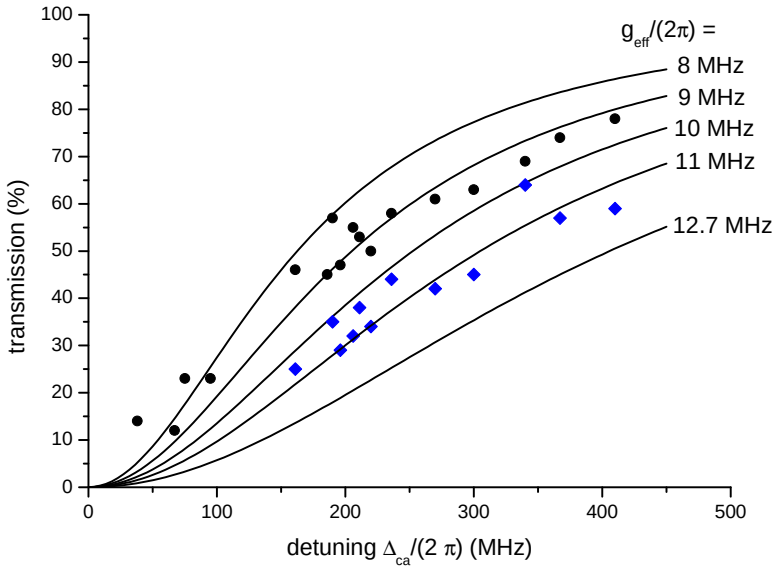

Figure 2.7: Normalised transmission $\bar{T}_1$ (black dots) and $\bar{T}_2$ (blue diamonds) for one and two atoms, respectively. The solid lines are calculated according to the effective two-level model (1.34) for one atom at rest with different values for g_{eff} . The one-atom data is the same as in fig. 1.13.

distance between two atoms loaded from the MOT into the YAG-dipole trap is distributed according to the size of the MOT, which is about 20 µm. For the presented measurement, those single shots were postselected for which the distance between two atoms was less than 10 µm, and the transport is performed such that both atoms have the same distance from the cavity centre. If both atoms are 5 µm away from the cavity centre, each one-atom coupling strength is reduced to $g(r)/g(0) = \psi(z = 0, r = 5\,\mu\text{m}) = \exp(-5^2/23^2) = 0.95$. Equation (1.33) is still valid for many atoms, if g^2 is replaced by [16]

$$g_{\text{tot}}^2 = \sum_i g_i^2 \,, \tag{2.17}$$

where g_i is the one-atom coupling strength for atom i. So even for two atoms maximally separated by 10 µm, assuming $g_1(r = 0) = g_2(r = 0) = 2\pi \times 9\,\text{MHz}$, the expected total coupling strength is still $g_{\text{tot}} = 2\pi \times 12.1\,\text{MHz}$. Other averaging effects due to thermal motion are already included in the *effective* one-atom coupling strength of 9 MHz. It remains unclear why the transmission for the case of two atoms is significantly higher, thus the combined coupling lower than expected.

An important consequence of this measurement is that the predicted maximum level separation of $\Delta\bar{T}_{12} = 33\%$ is never obtained for any detuning Δ_{ca}. The maximum difference is $\Delta\bar{T}_{12} = 19\%$ at $\Delta_{ca} = 2\pi \times 270\,\mathrm{MHz}$, where $\bar{T}_1 = 61\%$ and $\bar{T}_2 = 42\%$. Assuming an empty-cavity count rate of $R_{\mathrm{D},0} = 30\,\mathrm{ms}^{-1}$, the shot noise is comparable with the difference in counts for N_1 and N_2, making it almost impossible to deduce the number of atoms in $|F = 4\rangle$ from the measured transmission within 1 ms.

We can use the position of the atoms as another degree of freedom in our system to achieve a good distinction between $\bar{T}_1$ and $\bar{T}_2$, while at the same time working close to resonance.

Variation of the atomic position

A detuning of Δ_{ca} in the range of 200 to 300 MHz has two disadvantages for studying the spin-dynamics of two coupled atoms. Firstly, the difference in count rate is too small, and secondly, the scattering time R_{43}^{-1} is almost constant at its minimum value for $\Delta_{ca} > 2\pi \times 150\,\mathrm{MHz}$, with a very shallow slope towards higher detunings. Closer to resonance, the rate of inelastic Raman scattering R_{43} is lower, but if two atoms are at the cavity centre, the transmission levels $\bar{T}_1$ and $\bar{T}_2$ are almost indistinguishable.

The level difference $\Delta\bar{T}_{12}$ can, however, be controlled for a constant detuning Δ_{ca} by changing g_{eff} . This is possible by means of our optical conveyor belt, which allows us to transport atoms not only exactly into the cavity centre, but also to stop the transport at a predetermined distance Δy away from it. For the following discussion I will neglect the radial oscillation and the issue of insertion into different trapping sites, cf. section 1.6.3, and instead use the phenomenological parameter $g_0 = g_{\mathrm{eff}}\,(y = 0) = 2\pi \times 9\,\mathrm{MHz}$ for the coupling strength in the cavity centre. Thus the coupling strength as a function of position along the conveyor belt axis reads

$$g_{\mathrm{eff}}\,(\Delta y) = g_0 \exp\left(-\frac{\Delta y^2}{w_{0,\mathrm{cav}}^2}\right) . \tag{2.18}$$

As mentioned above, the level difference $\Delta\bar{T}_{12}$ has its maximum value for $g^2/(\kappa\Delta_{ca}) = 1/\sqrt{2}$. With $g = g_{\mathrm{eff}}\,(\Delta y)$, for each detuning $\Delta_{ca} < 2\pi \times 280\,\mathrm{MHz}$, a distance $\Delta y \neq 0$, given by

$$|\Delta y(\Delta_{ca})| = w_{0,\mathrm{cav}} \sqrt{\frac{1}{2}\ln\left(\frac{\sqrt{2}g_0^2}{\Delta_{ca}\kappa}\right)} , \tag{2.19}$$

yields $\Delta\bar{T}_{12} = 0.33$. For $\Delta_{ca} > 2\pi \times 280\,\mathrm{MHz}$, $\Delta\bar{T}_{12}$ is always at maximum for $\Delta y = 0$, i.e. at the cavity centre.

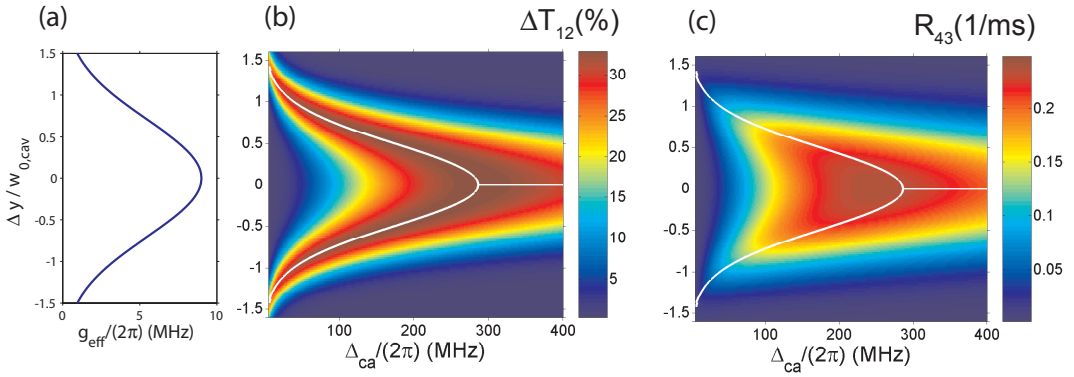

Figure 2.8: (a) Effective coupling as a function of distance Δy from the cavity centre. (b) Transmission level difference $\Delta\bar{T}_{12}$, (c) scattering rate R_{43} as a function of detuning Δ_{ca} and distance Δy. The white solid lines are points of maximum $\Delta\bar{T}_{12}$ calculated according to (2.19).

Figure 2.8 shows the level difference $\Delta\bar{T}_{12}$ (b) and the inelastic Raman scattering rate R_{43} (c) as a function of detuning Δ_{ca} and distance from the cavity centre Δy. By choosing a lower detuning, the scattering rate R_{43} is reduced, and it is still possible to obtain optimal distinction $\Delta\bar{T}_{12}$ by positioning the atoms away from the cavity centre. Empirically we found that a detuning of $\Delta_{ca} = 2\pi \times 38\,\mathrm{MHz}$ yields rather stable transmission traces and a distance of $\Delta y = 21\,\mu\mathrm{m}$ was adjusted for optimum distinction of one and two atoms.

2.3.2 Two-atom random telegraph signals

The experimental procedure described in section 2.2.3 was extended to the case of two atoms, which were positioned at $\Delta y = 21\,\mu\mathrm{m}$. At this position of around one cavity-waist away from the mode centre, the coupling strength depends more critical on the exact position. Two atoms loaded into the FORT were therefore only transported if the inter-atomic spacing was $\leq 2\,\mu\mathrm{m}$, which allowed us to easily select useful data. As for the one-atom case, the repumper was attenuated to a level at which it induced quantum jumps from $|F = 3\rangle$ to $|F = 4\rangle$ at a rate comparable with the probe laser induced jumps.

Figure 2.9 (a) shows an example single trace of a two-atom telegraph signal. For $t \approx 200...300$ ms, steps corresponding to $N_4 = 2$ (low transmission), $N_4 = 1$ (intermediate level), and $N_4 = 0$ (empty cavity level) are discernible, but in general the distinction between the levels is not as clear as for the one-atom case, cf. fig. 2.4. The quality of the level separation can be deduced from a histogram extracted from several hundred telegraph signals, see fig. 2.9 (b).

The normalised histogram does obviously not show a three-peak structure.

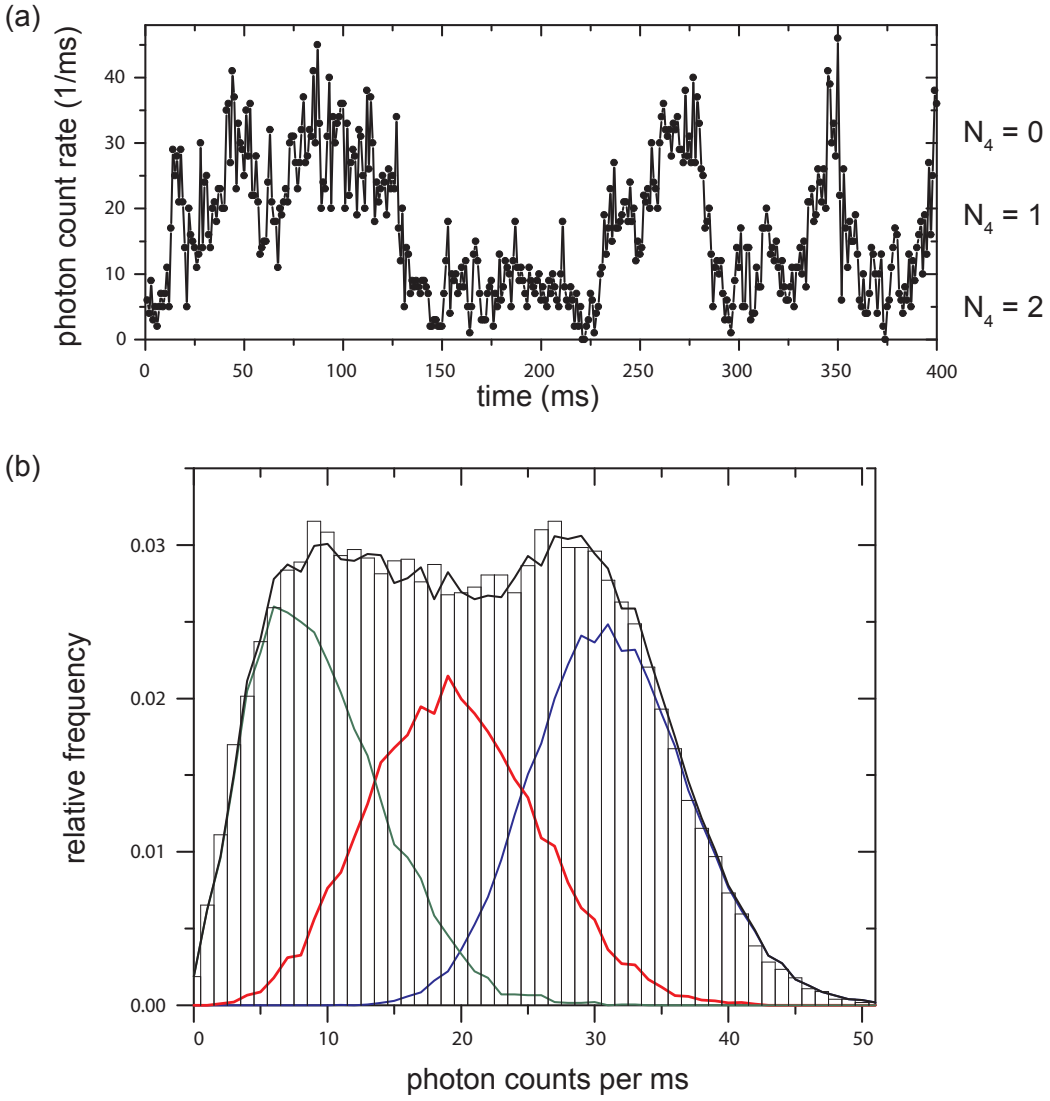

Figure 2.9: (a) Example trace of a random telegraph signal for two atoms placed $\Delta y = 21\,\mu\text{m}$ away from the cavity centre. The cavity-atom detuning is $\Delta_{ca} = 2\pi \times 38\,\text{MHz}$. (b) Normalised photon count histogram (bars) of many two-atom telegraph signals. The blue, red, and green lines are independently measured histograms for 0, 1, and 2 atoms coupled continuously to the cavity, respectively. The black line is a weighted sum of those three histograms.

To understand the contributions of the transmission levels $\bar{T}_0$, $\bar{T}_1$, and $\bar{T}_2$ we independently measured photon count histograms for 0, 1, and 2 atoms coupled to the resonator at the same position and for the same detuning. These were obtained from signals of continuously coupled atoms, i.e. a sufficiently strong repumper was applied. These three histograms, depicted as coloured solid lines in fig. 2.9 (b), obviously overlap to a high degree. A weighted sum of the three histograms (black line) with two independent weight factors as fit parameters agrees well with the measured two-atom random telegraph histogram. Because of the overlapping photon count histograms it is not possible to determine N_4 from the detected counts within 1 ms, but using statistical methods, it is possible to calculate probabilities for the number of atoms in the $|F = 4\rangle$ state.

2.3.3 Bayesian statistical analysis

Using the notation introduced in section 2.2.4, p_{N_4} is the probability that N_4 atoms are in the state $|F = 4\rangle$. The following statistical analysis allows us to extract $p_0(t)$, $p_1(t)$ and $p_2(t)$ from a measured random telegraph signal. The dynamics of the telegraph signal is described by a set of rate equations similar to (2.7a) and (2.7b):

$$\frac{dp_0}{dt} = -R_{01}p_0(t) + R_{10}p_1(t) \,, \tag{2.20a}$$

$$\frac{dp_1}{dt} = R_{01}p_0(t) - R_{10}p_1(t) - R_{12}p_1(t) + R_{21}p_2(t) \,, \tag{2.20b}$$

$$\frac{dp_2}{dt} = R_{12}p_1(t) - R_{21}p_2(t) \,. \tag{2.20c}$$

A transition of one atom from $|F = 3\rangle$ to $|F = 4\rangle$ is only induced by the repumper at a rate R_{rep} , which is independent of N_4 because the laser is applied from the side of the cavity. Thus $R_{12} = R_{\mathrm{rep}}$ and $R_{01} = 2R_{\mathrm{rep}}$, because for the latter case two atoms both in $|F = 3\rangle$ are present. In contrast, R_{21}, i.e. the rate that one out of two atoms in $|F = 4\rangle$ undergoes a quantum jump to $|F = 3\rangle$, is *not* simply given by $2R_{10}$, because this transition is induced by the probe laser, the intensity of which depends on N_4 [59]. Theoretically, the jump rate depends linearly on the intracavity intensity, therefore I assume that

$$R_{21} = 2\frac{\bar{T}_2}{\bar{T}_1}R_{10} \,. \tag{2.21}$$

For the statistical analysis, the three rates R_{10}, R_{21} and R_{rep} have to be known in advance. A good guess for the rate R_{10} can be obtained from an ensemble average of quantum jumps for a *single* atom placed at the same position Δy

away from the cavity centre, with no repumper applied, similar to the measurement presented in fig. 2.2 (d). The transmission levels $\bar{T}_2$ and $\bar{T}_1$ are measured independently, which yields an estimate for R_{21}. However, the relation (2.21) is not fixed for the algorithm described below, it serves only as a starting value for R_{21}, thus the three rates are considered to be independent for the calculation.

The rate R_{rep} cannot be measured independently, but since the power of the repumping laser is adjusted such that the transition rates from $|F = 4\rangle$ to $|F = 3\rangle$ and vice versa are approximately equal, R_{rep} is set to R_{10} as a starting value for the calculation. The exact value of the three rates is determined by an iterative self-consistent method, see below.

The probabilities $p_{N_4}(t)$ are governed by the rate equations discussed above, and in addition, the detected photon counts provide partial information about the current state. Using Bayes rule, the current value of each probability is updated after each time bin. Let us assume the probabilities $p_{N_4}(t_i)$ at some time t_i are known. The problem to solve is: What are the probabilities $p_{N_4}(t_j)$, where $t_j = t_i + \Delta t_m$ and Δt_m is the binning time step, taking the number of photons $n_{\mathrm{D}}\,(t_j)$ detected during the time interval $[t_i, t_j]$ and a-priori knowledge about our system into account?

Using the usual notation for conditional probabilities, we write

$$p_{N_4}(t_j) \equiv p(N_4|n_{\mathrm{D}}\,)(t_j)\;, N_4 = 0, 1, 2\;. \tag{2.22}$$

Applying Bayes rule and omitting the explicit time-dependence t_j for the sake of clarity, we have

$$p(N_4|n_{\mathrm{D}}\,) = \frac{p(n_{\mathrm{D}}\,|N_4)p(N_4)}{p(n_{\mathrm{D}}\,)}\;, \tag{2.23}$$

where the conditional probability $p(n_{\mathrm{D}}\,|N_4)$ to detect n_{D} photons, given that N_4 atoms are in $|F = 4\rangle$, is indeed time-independent and is extracted from the photon count histograms for 0,1, and 2 atoms, shown in fig. 2.9 (b).

The *unconditional* probability $p(N_4)$ that N_4 atoms are in $|F = 4\rangle$ at $t = t_j$ is obtained by extrapolating from the preceding time step, because $p_{N_4}(t_i)$ is supposed to be known. In a linear approximation for $R_x \Delta t_m \ll 1$, where $R_x = \max(R_{10}, R_{21}, R_{\mathrm{rep}}\,)$, this update according to the rate equations is given by

$$\begin{aligned}
p(0) &= p_0(t_i) + (R_{10}p_1(t_i) - 2R_{\mathrm{rep}}\,p_0(t_i))\Delta t_m && \text{(2.24a)}\\
p(1) &= p_1(t_i) + (2R_{\mathrm{rep}}\,p_0(t_i) + R_{21}p_2(t_i) - (R_{10} + R_{\mathrm{rep}}\,)p_1(t_i))\Delta t_m && \text{(2.24b)}\\
p(2) &= p_2(t_i) + (R_{\mathrm{rep}}\,p_1(t_i) - R_{21}p_2(t_i))\Delta t_m\;. && \text{(2.24c)}
\end{aligned}$$

For the unconditional probability $p(n_{\mathrm{D}}\,)$ to detect n_{D} photons during the

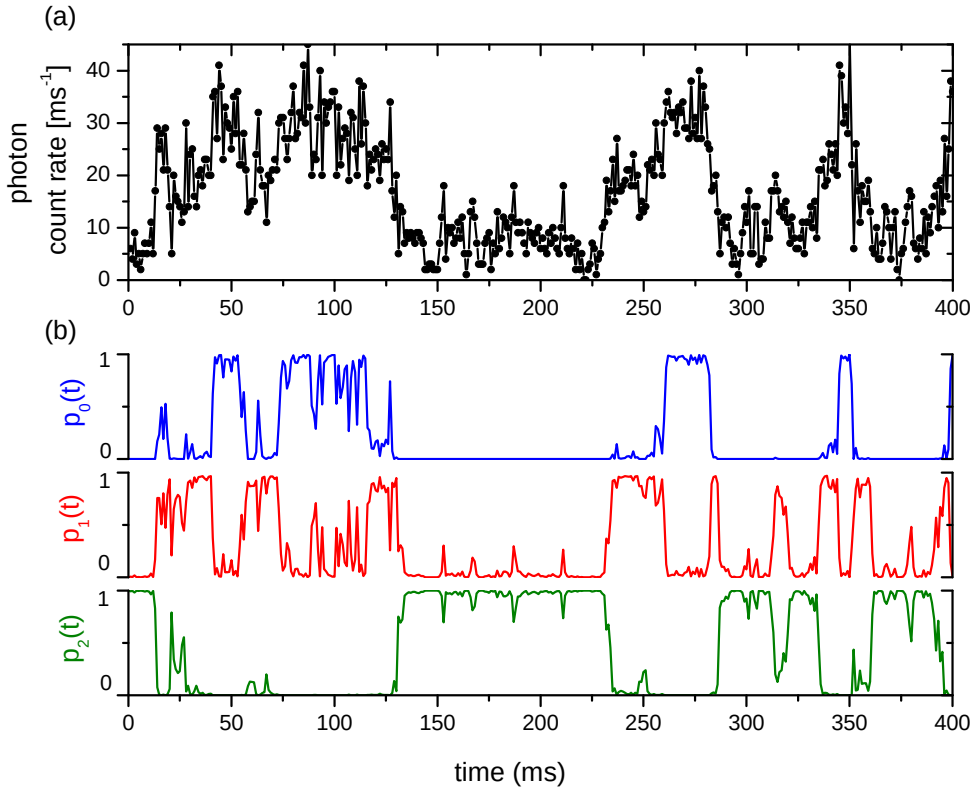

Figure 2.10: (a) Example trace of a random telegraph signal. (b) Probabilities for 0,1, or 2 atoms to be in $|F = 4\rangle$, calculated using the Bayes method.

interval $[t_i, t_j]$, the photon count histograms for 0,1, and 2 atoms are weighted with the state occupation probability, thus yielding

$$p(n_{\mathrm{D}}) = \sum_{N_4=0,1,2} p(N_4)p(n_{\mathrm{D}}\,|N_4)\ . \tag{2.25}$$

Setting the initial probabilities to $p_0(0) = 0$, $p_1(0) = 0$, and $p_2(0) = 1$, because both atoms are prepared in $|F = 4\rangle$ before they are transported towards the cavity, $p_{N_4}(t)$ is then updated stepwise for each time bin. In this way, the time-dependent probabilities are computed successively for the whole transmission trace. The outcome of this algorithm applied to the single trace shown in fig. 2.9 (a) is displayed in fig. 2.10 and shows that, despite the noisy raw data and the overlap of the photon count histograms, it is possible to extract additional information when the available knowledge about the dynamics of the system is

included. The two important characteristics of the Bayesian method are that no additional assumptions going beyond the available a-priori knowledge enter the calculation and that it provides all information that can be extracted from the measurement.

Self-consistent calculation of the quantum jump rates

The rates R_{10}, R_{21} and R_{rep}, entering the algorithm described above, were guessed or indirectly deduced from other measurements. Applying the Bayes method to many single traces permits a self-consistent calculation in the following way: An analytical solution of the rate equations (2.20) for $p_0(t)$, $p_1(t)$ and $p_2(t)$, with the initial conditions $p_0(0) = 0$, $p_1(0) = 0$, and $p_2(0) = 1$, yields the ensemble-averaged probabilities $\langle p_{N_4}\rangle(t)$ with the three jump rates as parameters.

Averaging over the probabilities $p_{N_4}(t)$ obtained from the analysis of many traces provides an *experimental* result for $\langle p_{N_4}\rangle(t)$, which can be fitted with the analytical solution, in which the rates R_{10}, R_{21} and R_{rep} are used as fit parameters. With the rates obtained in this way, the Bayes algorithm is applied again to all experimental traces, yielding an updated set of probabilities $p_{N_4}(t)$, which is again averaged to extract the rates. This process is continued until the difference between the rates obtained from two successive iterations is smaller than a predefined threshold. The set of rates obtained from this analysis is

$$R_{10} = 104\,\mathrm{s}^{-1}\ ,\ R_{21} = 52\,\mathrm{s}^{-1}\ ,\ R_{\mathrm{rep}}\ = 45\,\mathrm{s}^{-1}\ . \tag{2.26}$$

The experimentally averaged probabilities $\langle p_{N_4}\rangle(t)$ and the fitted solution of the rate equations, plotted in fig. 2.11, are in good agreement. However, there is an apparent inconsistency in the ratio of the two rates R_{10} and R_{21}: From the photon count rate histogram, the average transmission levels are obtained to be $\bar{T}_1 = 19.5\,\mathrm{ms}^{-1}$ and $\bar{T}_2 = 9.3\,\mathrm{ms}^{-1}$. Thus according to the assumption (2.21), we would expect that $R_{21} \approx R_{10}$, but the result (2.26) shows that $R_{21} = \frac{1}{2}R_{10}$.

The ratio of the rates can be independently checked by analysing the photon count histogram (fig. 2.9 (b)). The weight factors for the three individual histograms represent an additional information that has not entered the Bayes algorithm described above. They are connected to the rates analogous to the one atom case described by (2.8a) and (2.8b). The steady state probabilities $\bar{p}_{N_4} = \langle p_{N_4}\rangle(t \to \infty)$, obtained by setting $\dot{p}_{N_4}(t) = 0$ in (2.20), are determined

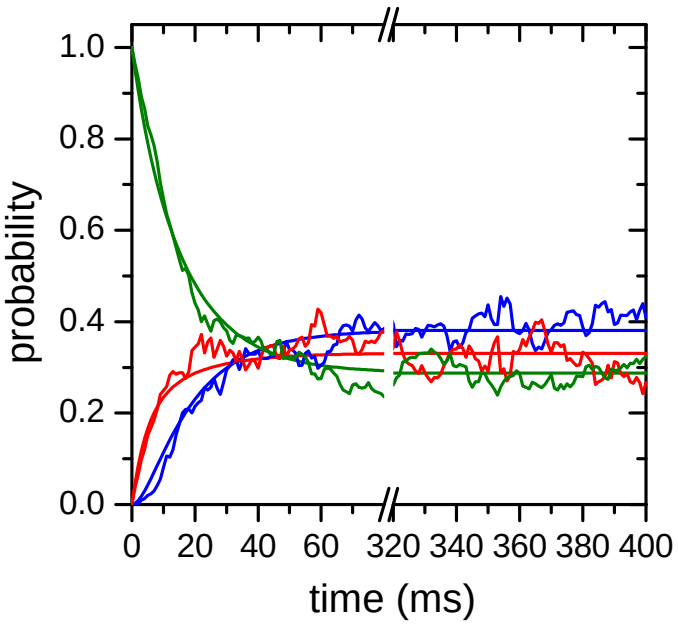

Figure 2.11: Probabilities for 2 atoms (green), 1 atom (red), and 0 atoms (blue) to be in $|F = 4\rangle$ calculated with the Bayes method for all individual traces and then averaged. The solid lines are the best fitting analytical solution of the rate equation.

by the jump rates in the form

$$\bar{p}_0 = \frac{R_{10}R_{21}}{D} = 38\% \tag{2.27a}$$

$$\bar{p}_1 = \frac{2R_{21}R_{\mathrm{rep}}}{D} = 33\% \tag{2.27b}$$

$$\bar{p}_2 = \frac{2R_{\mathrm{rep}}^2}{D} = 29\% \tag{2.27c}$$

$$D = R_{10}R_{21} + 2R_{21}R_{\mathrm{rep}} + 2R_{\mathrm{rep}}^2 \ , \tag{2.27d}$$

where (2.26) was inserted for the rates. These probabilities are almost identical to the independently determined weight factors. Thus the factor of two difference in the rates R_{10} and R_{21} is confirmed. Probably the processes involving two atoms are more complicated than described by the simple relation (2.21).

2.4 Conclusion

The experiments presented in this chapter demonstrate that with the existing setup it is possible to study the internal dynamics of one and two atoms. For the one atom case, a high state detection fidelity of 93% for a binning time of 1 ms was realised. For two atom coupled to the cavity, the signal to noise ratio is not sufficient to deduce the number N_4 of atoms coupled to the cavity from a single time bin, since the corresponding histograms overlap. However, using a-priori knowledge about our system (jump rates and photon count histograms), probabilities can be extracted employing Bayesian statistics. The histograms also show that the width of the $N_4 = 1$ and $N_4 = 2$ peaks is not shot-noise limited, owing to variations in the coupling. In the next chapter, I will discuss how control over the external degrees of freedom can be improved with the goal to achieve a more stable and higher coupling strength.

3 External dynamics – cooling and trapping atoms inside the cavity

The experiments presented so far show that the measured effective coupling strength g_{eff} is lower than the theoretically expected maximum coupling. In section 1.6.3, radial oscillation across the cavity mode was used as a model to explain this discrepancy. Methods to improve the localisation of atoms coupled to the cavity are the focus of this chapter, because a stable coupling strength is vital for all envisioned experiments.

In the first part, I will present results on using a red-detuned lock laser, which acts as an intracavity dipole trap. In the second part, I begin by providing a theoretical background on cavity cooling. Subsequently I discuss experiments which demonstrate a different regime of cavity cooling, where the cavity is *red-detuned* from the atomic resonance, in contrast to all experiments presented in chapter 2.

3.1 Intracavity dipole trap

To study the possible effects of an improved localisation of the atoms, we changed the lock laser wavelength to $\lambda_{\text{lock}} = 857\,\text{nm}$, red detuned by two free spectral ranges. For this wavelength, the beat length between probe and lock laser standing wave is 73 µm, see (1.48), thus the effect of insertion into different trapping sites along the cavity axis is very small. The main difference compared to the blue-detuned lock laser used in the experiments discussed so far is that the atoms are not repelled by the lock laser, but trapped at its anti-nodes axially as well as radially. In the following I will present different measurements to characterise the intracavity trap.

3.1.1 Trapping atoms inside the cavity

In order to verify that the atoms are indeed trapped by the lock laser, we transported a single atom into the cavity centre, switched the conveyor belt off after 5 ms, and observed the cavity transmission continuously. Applying a strong repumper all the time, a rise in transmission thus indicates atom losses. From the ensemble average we can then infer the average survival probability as a function

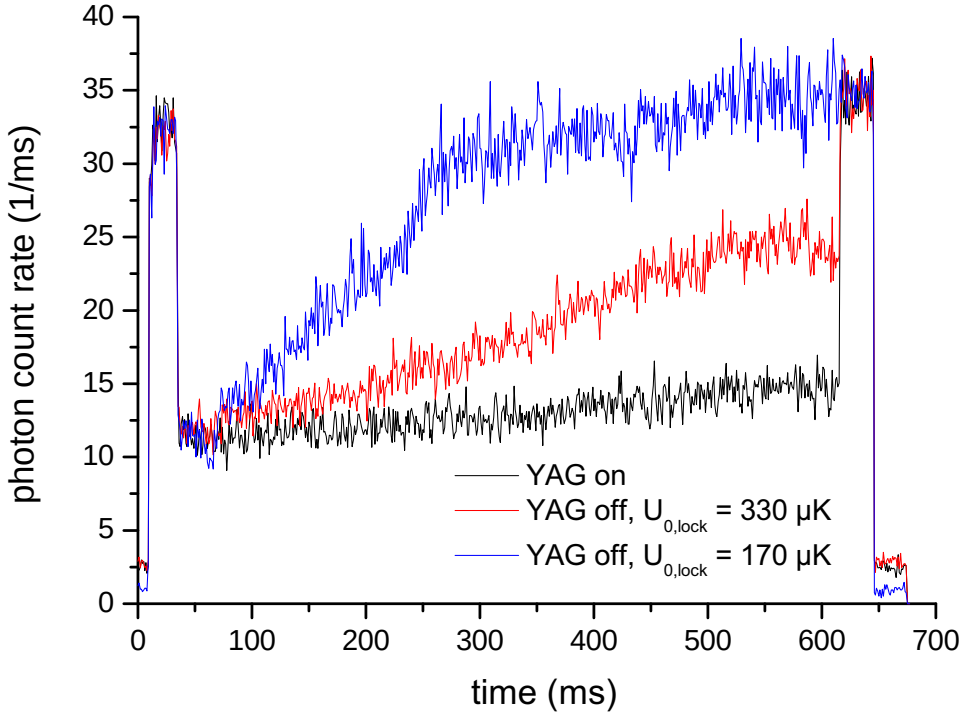

Figure 3.1: Trapping of atoms by the lock laser. The three curves are ensemble averages for the cases with the FORT switched on (black curve) and switched off (blue and red curve). For this measurement, the guiding field was applied along the cavity axis and $\Delta_{ca} = 2\pi \times 196\,\mathrm{MHz}$.

of trapping time. Figure 3.1 shows the result for two different lock laser powers and for comparison the case when the YAG laser is not switched off. For this measurement we chose a detuning of $\Delta_{ca} = 2\pi \times 196\,\mathrm{MHz}$, because in this range we have observed a more stable coupling and thus transmission traces with less variations than close to resonance.

The lock laser potential $U_{0,\mathrm{lock}}$ is obtained from a calibrated avalanche photodiode (APD), as will be explained in the next section. For $U_{0,\mathrm{lock}} = k_B \times 170\,\mu\mathrm{K}$, the trap is obviously so shallow that almost all atoms are lost after approximately 200 ms, whereas for $U_{0,\mathrm{lock}} = k_B \times 330\,\mu\mathrm{K}$ the survival probability is much higher, but still not the same as if the conveyor belt is switched on as well. This result shows that atoms can be trapped inside the cavity by the lock laser alone, which has the advantage that the system is "cleaner" in many ways, e.g. the AC-Stark shift of the conveyor belt does not have to be taken into account.

3.1.2 Lock laser trap depth

To determine the depth of the intracavity dipole trap we measured the axial trap frequency, which in the harmonic approximation is determined by the potential depth $U_{0,\mathrm{lock}}$ according to

$$\Omega_{\mathrm{ax}} = 2\pi\sqrt{\frac{2U_{0,\mathrm{lock}}}{m_{\mathrm{Cs}}\,\lambda_{\mathrm{lock}}^2}}\,. \tag{3.1}$$

The trap frequency was measured using parametric heating of single atoms [26]. This was facilitated by amplitude modulation of the lock laser, which translates into a modulation of the potential depth with the modulation frequency Ω_{mod}. The modulation frequency was swept from 400 to 800 kHz in 40 kHz steps and vice versa, while the cavity transmission was continuously observed. A sufficiently strong repumper was constantly applied so that a rise in transmission indeed indicates loss of atoms and not a change in the hyperfine ground state. Furthermore, the conveyor belt was switched off during the sweep to make sure that only the characteristics of the lock laser trap are measured.

The sweep was done in both directions because from one trace alone, e.g. from 400 to 800 kHz, the trap frequency cannot be derived. Depending on the amplitude of the excitation, the resonant excitation frequency could be at e.g. 30% or 70% *cumulative* atom loss. Employing the symmetry of the situation, an additional reverse sweep determines the resonant excitation frequency to be approximately at the crossing of the two loss curves. In contrast to [26], here the ensemble average is obtained from many realisations of *single atom* loss curves, because with two or more atoms trapped inside the cavity, only the last atom lost from the cavity would cause the transmission to rise to the empty cavity level, rendering the analysis of the data impossible.

Figure 3.2 (a) shows the raw data of an ensemble average for stepping the modulation frequency in both directions. For further analysis, the part of the data containing the sweep was binned in 10 ms time steps, which was the dwell time for each frequency step, and normalised from 0 to 100%, see fig. 3.2 (b). Two sets of data are shown, now as a function of modulation frequency, for different amplitude modulation strengths. The numbers of -10 and -13 dBm, respectively, indicate the setting of a signal generator, the output of which was used for amplitude modulation of the VCO (voltage controlled oscillator) driving the lock laser AOM and thereby modulating its power. The two crossing points are at the same position, thereby verifying the symmetry assumption. From the resonance excitation frequency $\Omega_{\mathrm{mod},0} \approx 2\pi \times 580\,\mathrm{kHz}$, the axial oscillation frequency is obtained to be

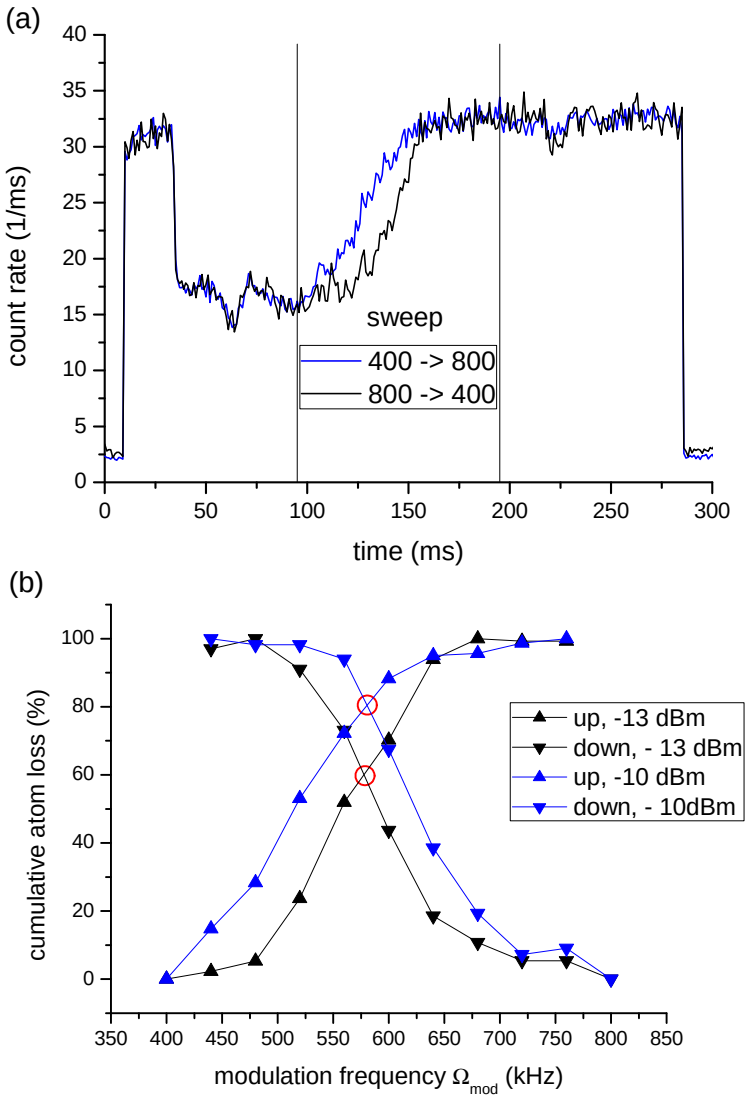

Figure 3.2: Measurement of the axial trap frequency. (a) Ensemble average showing the measured transmission as a function of time while sweeping the lock laser modulation frequency. (b) Cumulative atom loss for ramping the modulation frequency up and down. The black (blue) data points are for an amplitude modulation setting of the signal generator of -13 (-10) dBm. The crossing of the curves is at twice the axial trap frequency. For this measurement, the guiding field was applied along the cavity axis, the detuning was $\Delta_{ca} = 2\pi \times 196\,\mathrm{MHz}$, and the lock laser potential depth extracted from the data is $U_{0,\mathrm{lock}} = k_B \times 0.5\,\mathrm{mK}$.

$$\Omega_{\mathrm{ax}} \approx 2\pi \times 290\,\mathrm{kHz} \Rightarrow U_{0,\mathrm{lock}} = k_B \times 0.5\,\mathrm{mK} = h \times 10\,\mathrm{MHz}\,, \tag{3.2}$$

where $\Omega_{\mathrm{ax}} = \frac{1}{2}\Omega_{\mathrm{mod},0}$ because of *parametric* heating. In this calculation an uncertainty lies in applying the harmonic approximation, because in our measurement the atoms are heated until they escape from the trap. Due to the anharmonicity of the trap potential the oscillation frequency of the atom changes as the atom's energy approaches the potential depth. However, for this context a reasonable estimate of the trap depth is sufficient, thus I neglect the effect of the anharmonicity.

The result for $U_{0,\mathrm{lock}}$ can be used for a calibration based on the transmitted lock laser power, which is measured using an amplified avalanche photodiode (APD) after probe and lock laser are separated using a Glan-Taylor polariser, cf. section 1.3 and [30]. The APD voltage is always recorded along with the SPCM counts by the data acquisition software and is directly proportional to the intracavity lock laser power and therefore also to the lock laser potential. Since the APD voltage for this measurement is known, the potential depth for different laser intensities is directly calculated. However, this calibration is only valid for the specific wavelength of $\lambda_{\mathrm{lock}} = 857\,\mathrm{nm}$ because the cavity transmission and loss coefficients $(\mathcal{T}, \mathcal{A})$ are also wavelength dependent. In addition, it is important to keep the reverse voltage applied to the APD constant (here -230 V), since otherwise the signal voltage of the APD is not a reliable reference.

From the potential depth the intracavity power and intensity of the lock laser can be inferred. $U_{0,\mathrm{lock}}$ is equal to the AC Stark shift of the ground state, which is m_F independent due to the linear polarisation of the lock laser mode. In the appendix of [27], the $S_{1/2}$ ground state shift for π transitions for a red-detuned laser was derived to be

$$\Delta E_{\pi}^{(S)} = -\frac{e^2 I}{12 m_e c \varepsilon_0}\left(\frac{2}{\omega_{3/2}\Delta'_{3/2}} + \frac{1}{\omega_{1/2}\Delta'_{1/2}}\right)\,, \tag{3.3}$$

where $\omega_{3/2}$ and $\omega_{3/2}$ are the transitions frequencies of the D_2 and D_1 line, respectively, and

$$\frac{1}{\Delta'_{J'}} = \frac{1}{\omega_l + \omega_{J'}} + \frac{1}{\omega_l - \omega_{J'}} \tag{3.4}$$

defines the detuning of the laser frequency ω_l from the excited $P_{J'}$ state. With $\Delta E_{\pi}^{(S)} = U_{0,\mathrm{lock}}$, the intracavity lock laser intensity can thus be calculated. From the measured data presented above, one obtains $I_{\mathrm{sw,lock}} = 1.1 \times 10^8\,\mathrm{W\,m^{-2}}$ for the intracavity lock laser intensity and with $I_{\mathrm{sw,lock}} = 8P_{\mathrm{circ,lock}}/(\pi w_{0,\mathrm{cav}}^2)$, the circulating lock laser power is $P_{\mathrm{circ,lock}} = 22\,\mathrm{mW}$.

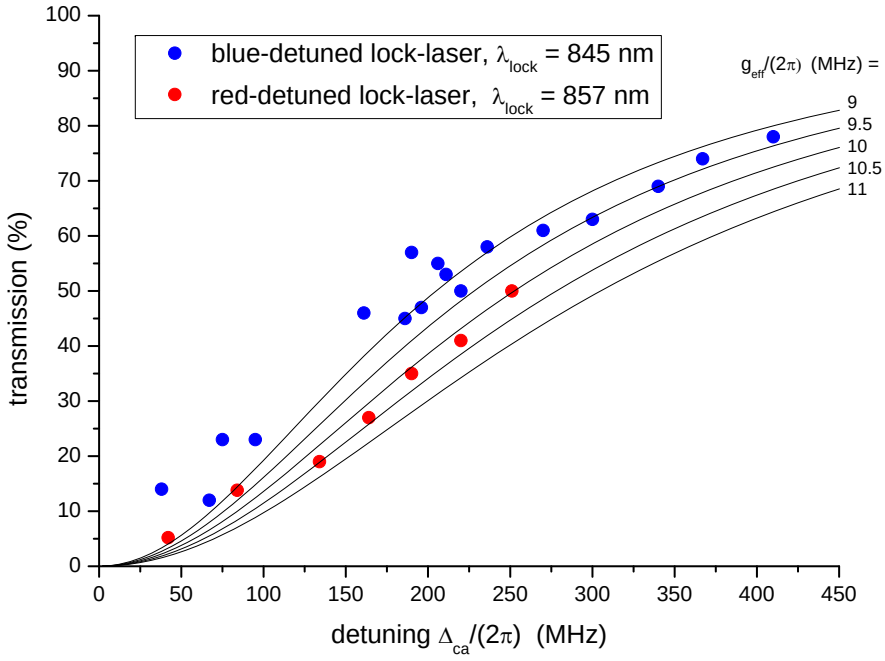

Figure 3.3: Normalised cavity transmission as a function of detuning for the case of a red-detuned and blue-detuned lock laser. The blue data points are taken from fig. 1.13. The solid lines are calculated according to (1.34) for different values of g_{eff} .

Continuously measuring the escape of atoms from the trap as a function of modulation frequency is a fast and reliable technique to measure the trap frequency. In former experiments on measuring the radial trap frequency, the relative atom loss as a function of excitation frequency had to be determined from a whole ensemble average for each frequency [26]. With the method used here, averaging over 20 to 30 single traces directly yields this information.

3.1.3 Improved localisation

An intracavity dipole trap should lead to a better localisation of atoms, detectable by a lower probe laser transmission. The normalised cavity transmission was measured for a range of different detunings Δ_{ca}. Figure 3.3 shows the data for the red lock laser, compared to the data already discussed at the end of chapter 1 in section 1.6.

The transmission was not measured for the same range of detunings because changing Δ_{ca} over such a big range is rather time-consuming due to technical

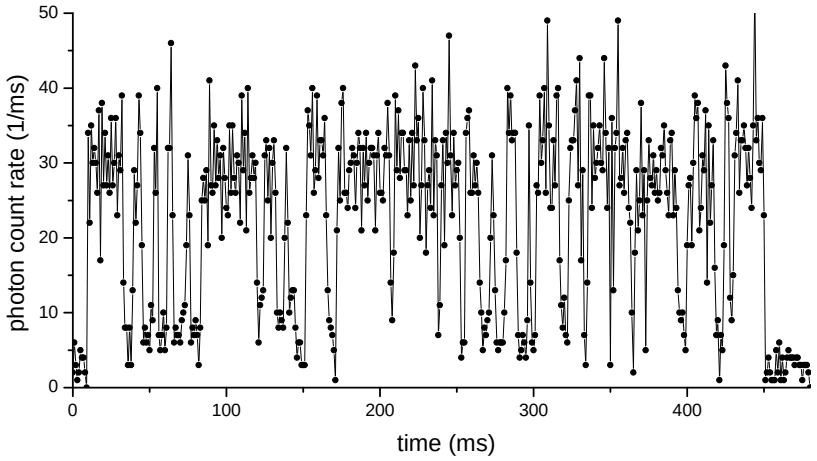

Figure 3.4: Telegraph signal with no external repumper applied. The quantum jumps from $|F = 3\rangle$ (high transmission) to $|F = 4\rangle$ (low transmission) are induced by the lock laser alone. The detuning is $\Delta_{ca} = 2\pi \times 139\,\mathrm{MHz}$, the circulating lock laser power, inferred from the APD voltage, is $P_{\mathrm{circ,lock}} = 14.7\,\mathrm{mW}$.

reasons. Here we were mainly interested in a qualitative result, which is indeed clearly obtained from the measured data points. The normalised transmission is systematically lower for the red-detuned lock laser, indicating a higher g_{eff} and thus a better localisation.

Another interesting observation is that we could also measure the transmission for detunings in the range of 100 to 160 MHz. This had not been possible with the blue-detuned laser, since for these detunings we had repeatedly observed very unstable transmission signals. This measurement shows that an intracavity trap leads to a better localisation of the atoms. However, it also poses a problem in terms of state detection, as I will discuss in the following.

3.1.4 Lock laser induced quantum jumps

Trapping atoms at the intensity maxima will lead to a much higher photon scattering rate compared to the case of a blue-detuned laser. In order to assess how severe this scattering is in the context of the experiments presented in chapter 2, we continuously measured the cavity transmission for one coupled atom without a repumper, see fig. 3.4. As discussed in section 2.2, the probe laser induces transitions from $|F = 4\rangle$ to $|F = 3\rangle$ by virtue of inelastic Raman scattering via excited intermediate states. Since the lock laser detuning of 5 nm is much larger than the hyperfine splitting of 9.2 GHz, it will induce transitions both from $|F = 3\rangle$ to $|F = 4\rangle$ and vice versa at a similar rate.

Analysing the telegraph signal in the same way as presented in section 2.2.4, the rates obtained from dwell time histograms are

$$R_{34} = R_{\text{scatt,lock}} = 41\text{s}^{-1} , \tag{3.5}$$

$$R_{43} = R_{\text{scatt,lock}} + R_{\text{scatt,probe}} = 164\text{s}^{-1} , \tag{3.6}$$

$$\Rightarrow R_{\text{scatt,probe}} = 123\text{s}^{-1} . \tag{3.7}$$

The value of $R^{-1}_{\text{scatt,probe}} = 8\,\text{ms}$ for $\Delta_{ca} = 2\pi \times 139\,\text{MHz}$ is compatible with earlier measurements, cf. fig. 2.3.[1]. The order of magnitude of the rate of hyperfine state changing scattering by the lock laser alone is confirmed by a calculation based on the Kramers-Heisenberg-formula (1.73).

A red-detuned lock laser as an intracavity dipole trap is not compatible with QND measurements of the atomic state – at least not in the configuration presented here, where the lock laser is still rather close to the atomic resonance. A possible solution for future modifications of the experimental setup would be to use a far-detuned laser to better localise the atoms.

This could still be done by a an intracavity trap, but further detuned, similar to the setups in the groups of Prof. Kimble at Caltech [60] and Prof. Rempe at MPQ [61]. If the trapping laser is far detuned, e.g. at the "magic wavelength" of 936 nm as in the case of the Caltech experiment, it can not serve as a lock laser at the same time, because for such a large detuning the cavity finesse is much lower than on resonance and not suitable for precise cavity stabilisation any more. An additional lock laser is necessary for this configuration, which should then be blue detuned and as weak as possible in order to avoid additional competing confinement. Another conceivable solution is to shine in an additional laser from the side of the cavity, along the conveyor belt axis but with a small focus at the position of the cavity centre, creating a "dimple trap".[2]

So far I have treated the geometric localisation by conservative dipole potentials. In the second part of this chapter, I will discuss cavity cooling, which is a cavity-QED effect providing cooling forces within the cavity.

[1] For the measurements presented in fig. 2.3, the empty cavity countrate was $R_{\text{D},0} = 20\,\text{ms}^{-1}$, whereas here it is $30\,\text{ms}^{-1}$, explaining the higher scattering rate

[2] See outlook of [15] for a simulated beam profile which shows that a waist of $w_0 \approx 11\,\mu\text{m}$ is achievable with standard optical elements.

3.2 Cavity cooling

3.2.1 Introduction

The theory of an atom coupled to a cavity presented in chapter 1 describes a point-like atom at rest. Forces on the atom and effects due to motion of the atom were not considered. An exception is section 1.6.3, where radial oscillation was used as an explanation for $g_{\text{eff}} < g_{\max}$. But this treatment only considered the spatial variation $\psi(\mathbf{r})$ and its consequence for the measured transmission $\bar{T}$.

The mechanical effects of the atom-field interaction inside a cavity were studied theoretically by different research groups. The elementary system under consideration is a point-like two-level atom interacting with the standing wave mode of the cavity field, without further trapping potentials [24, 62–67].

In a real experiment, atoms are always trapped by an optical lattice, realised either as an intracavity trap, a lattice perpendicular to the cavity, or a combination of both, see e.g. [23, 60, 68, 69]. Theoretical work taking the effect of an additional optical lattice into account includes [70–75]. The combination of an optical lattice perpendicular to the cavity and an additional pump beam under 45° led to 3D-cooling and long lifetimes [76], which was theoretically investigated in [77]. Cooling to the ground state of axial motion was reported in [19], but in that experiment cavity independent Raman cooling was employed, and no cavity cooling in the sense described in the aforementioned publications was used. An extension of the theory to the scenario of more than one atom interacting with the cavity field can be found in [78–80].

Our system is quite complex, involving two dipole potentials, created by the conveyor belt and the lock laser. I will, nonetheless, only consider the theory developed for a point-like atom interacting with one mode of a driven cavity, because already for this system interesting predictions on different cooling regimes are obtained. One of the main outcomes of [24] is that two cooling regimes exist for different settings of probe-cavity and probe-atom detunings, and this is what is confirmed by our measurements. Although an additional dipole potential is initially not treated by this theory, the confining effect of the lock laser is included in the calculations by incorporating the discrete trapping sites along the cavity axis into the model.

3.2.2 Theoretical description of cavity cooling

For the theory discussed here, only the axial variation of the coupling strength of the form

$$g(z) = g_{\max} \cos\left(\frac{2\pi}{\lambda_{\text{probe}}} z\right) \tag{3.8}$$

is taken into account, radial motion along x like in the 2-D model in section 1.6.3 is not considered. In section 1.2.3, steady-state solutions for operators and operator products were derived from the master equation. Here we are interested in the force acting on the atom, which can be expressed as

$$F(z) = \dot{p} = \frac{i}{\hbar}[H, p] = -\hbar \nabla g(z)(a^\dagger \sigma + \sigma^\dagger a) \,, \tag{3.9}$$

from which the expectation value of the force for the steady state can be obtained by inserting $\langle X_1 \rangle^{(0)}$ (first component of the steady-state vector $\langle \mathbf{X} \rangle^{(0)}$, see (1.31)), which yields

$$F_0(z) = \langle F(z) \rangle^{(0)} = -2\hbar\varepsilon^2 \frac{\Delta_{pa} g(z)}{|\det(\mathbf{A})|^2} \nabla g(z) = -2\hbar \frac{\Delta_{pa} g(z)}{\Delta_{pa}^2 + \gamma^2} n_p \nabla g(z) \,, \tag{3.10}$$

where $|\det(\mathbf{A})|^2 = (\gamma\kappa + g(z)^2 - \Delta_{pa}\Delta_{pc})^2 + (\Delta_{pa}\kappa + \Delta_{pc}\gamma)^2$, and $n_p = \langle a^\dagger a \rangle$. The dipole force F_0 is a conservative force since it is not velocity dependent. The atom is attracted to the antinodes of the cavity field for $\Delta_{pa} < 0$ (high field seeker), whereas the opposite holds for positive detuning, i.e. F_0 describes a probe-laser-induced dipole trap. For typical experimental parameters, detuning $\Delta_{pa} = 2\pi \times 50\,\text{MHz}$ and photon count rate of $R_\text{D} = 10\,\text{ms}^{-1}$, corresponding to $n_p = 0.09$, the potential depth is $U_{\text{dip,probe}} \approx k_B \times 15\,\mu\text{K}$, much smaller than all other potentials.

Dissipative force

The force acting on an atom moving with the velocity v along the cavity axis is expanded in powers of v:

$$F(z) = F_0(z) + vF_1(z) + \ldots \,, \tag{3.11}$$

where F_0 is the conservative part of the force, see (3.10) and F_1 is the *friction coefficient*. In terms of a Taylor expansion,

$$F_1(z) = \frac{\partial F(z)}{\partial z} = -\hbar \nabla g(z) \langle X_1 \rangle^{(1)} \,, \tag{3.12}$$

where $\langle X_1 \rangle^{(1)}$ is the first component of the vector $\langle \mathbf{X} \rangle^{(1)}$, which is part of an expansion in v of the form $\langle \mathbf{X} \rangle = \langle \mathbf{X} \rangle^{(0)} + v\langle \mathbf{X} \rangle^{(1)} + \ldots$. By expanding

the density matrix in powers of v, $\langle \mathbf{X} \rangle^{(1)}$ is calculated from the following set of equations [24]:

$$v \frac{\partial}{\partial z} \langle \mathbf{Y} \rangle^{(0)} = \mathbf{A} \langle \mathbf{Y} \rangle^{(1)} , \tag{3.13}$$

$$v \frac{\partial}{\partial z} \langle \mathbf{X} \rangle^{(0)} = \mathbf{B} \langle \mathbf{X} \rangle^{(1)} + \varepsilon \langle \mathbf{I} \rangle^{(1)} , \tag{3.14}$$

where also for the other vectors $\langle ... \rangle^{(0)}$ and $\langle ... \rangle^{(1)}$ denotes the zeroth and first-order expectation values, respectively, and the matrices $\mathbf{A}$ and $\mathbf{B}$ were defined in section 1.2.3. The friction coefficient can be written as a sum of two contributions,

$$F_1 = F_{\text{at}} + F_{\text{cav}} , \tag{3.15}$$

where F_{at} dominates for a strongly damped cavity, when the cavity relaxation is much faster than the atomic relaxation. In this case the system is governed by the atomic dynamics. In the extreme limit, when the cavity decouples from the system, F_{at} is purely due to Doppler cooling. This regime is a valid approximation if $\kappa \gg g$ and if the *atom* is driven, which is both not the case in our system. For a weakly damped cavity, F_{cav} dominates. Here one assumes that the internal dynamics of the atom is faster than that of the cavity, which is a good approximation for $g, \gamma \gg \kappa$ and driving the *cavity*, which corresponds to our experimental settings.

The complete analytical result for F_1 is rather lengthy, thus I do not state it here. It can be found in the appendix of [24] and is the basis for the numerical simulations presented in the next section.

The physical origin of the cooling force is a retardation effect. If an atom moves along the cavity axis, the coupling strength changes according to the spatial dependence $g(z)$, but the cavity field does not adapt to this situation instantaneously. The cooling force can also be understood as a mechanism similar to Sisyphus cooling in free space, see [24] for a detailed account on this interpretation.

3.2.3 Numerical simulations

Owing to the spatial variation of $g(z)$, also F_1 is position dependent. If confinement by the lock laser is not taken into account, as in the original publication [24], the atom can move freely along z, thus the friction coefficient is averaged over all z. Due to the periodicity of $|g(z)|$ of $\frac{1}{2}\lambda_{\text{probe}}$, it is sufficient to average over one

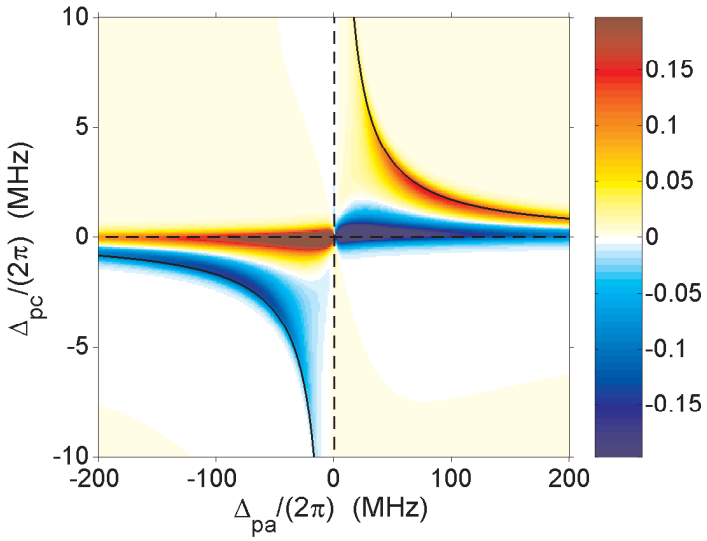

Figure 3.5: Averaged friction coefficient as a function of detunings Δ_{pa} and Δ_{pc}, where blue (red) represent a negative (positive) friction coefficient, i.e. cooling and heating, respectively. The parameters are $(g, \kappa, \gamma) = 2\pi \times (13.1, 0.4, 2.6)$ MHz. The dressed states are plotted as black solid lines, cf. fig. 1.3. The colorbar indicates F_1/m_{Cs} in MHz.

period for the calculation. Fig. 3.5 shows the averaged friction coefficient for our experimental parameters. Two different cooling regimes can be identified. For a blue detuned probe laser, $\Delta_{pa} > 0$, cooling, indicated by negative friction, occurs if the probe laser is resonant with the empty cavity, i.e. $\Delta_{pc} = 0$. For $\Delta_{pa} < 0$, cooling is obtained for a probe laser red-detuned from the cavity, such that it is shifted into resonance once an atom is coupled to the cavity.

In our experiment, the atom is confined by the lock laser along the cavity axis, and it can be inserted into trapping sites not coinciding with a probe laser antinode, see the discussion in section 1.3.2. At $z = z_{\mathrm{min}} = \frac{1}{4}\lambda_{\mathrm{probe}}$, the atom is at a position of zero coupling (see fig. 1.6). The friction coefficient $F_1(\Delta_{pa}, \Delta_{pc})$ for different positions z is plotted in fig. 3.6 (b) to (f). Cooling and heating regions are always next to the dressed states, which "move closer" to $\Delta_{pc} = 0, \Delta_{pa} = 0$ for weaker coupling. The magnitude of the friction coefficient increases as the atomic position approaches z_{min}. For $z = 0$, i.e. at a probe laser antinode, the friction is around three orders of magnitude smaller than for the other positions.

In principle, our experimental data cannot be describes by just *one* of the "cooling maps" presented in fig. 3.6. Regarding the measurement of the averaged transmission as a function of detuning, each data point for one detuning

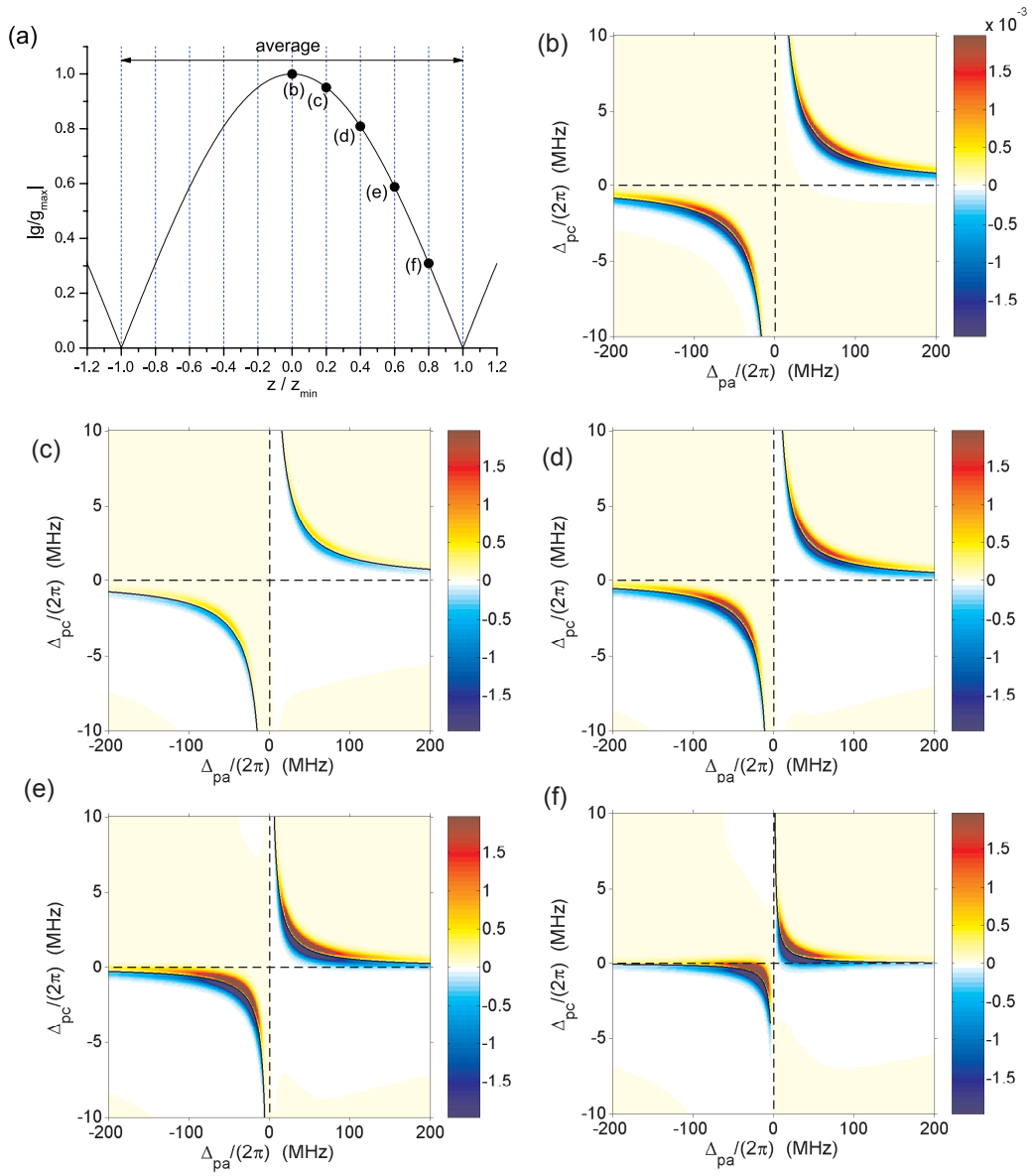

Figure 3.6: (a) Normalised coupling strength $|g(z)/g_{\max}|$ as a function of position z along the cavity axis. The black dots indicate the positions for which the friction coefficient $F_1(\Delta_{pa}, \Delta_{pc})$ is calculated. The positions are $0.2z_{\min}$ (b), $0.4z_{\min}$ (c) etc. Note the factor of 10^{-3} in the color bar (indicating F_1/m_{Cs} in MHz) of (b) compared to (c) to (f). Cooling and heating regions are always close to the dressed states, which are shown as black solid lines.

as presented in fig. 1.13 is obtained from many single shots. It therefore represents an ensemble average over experimental realisations with different trapping sites along the cavity axis. A more realistic description could be obtained by a weighted average over many cooling maps. But also for a single trace, the atom oscillates along the cavity axis between two potential "walls" with a small amplitude (in the case of a blue detuned lock laser) and radially along x.

The data presented in section 1.6 allows us to compare the theoretical predictions for $\Delta_{pa} > 0$ to the experimental results, because long observation times of several hundred milliseconds like the one shown in fig. 1.12 are a consequence of cavity cooling. We verified this assumption by transporting an atom into the cavity and measuring its lifetime without any probe light coupled into the cavity. The lifetime, limited by lock laser induced heating, is around 130 ms, see [15], which is most likely due to parametric excitation of atomic motion, caused by a fluctuating intracavity lock laser intensity.

Continuous transmission traces were measured for $\Delta_{pc} = 0$ and $\Delta_{pa}/(2\pi) \approx 30...450$ MHz, cf. fig. 1.13. From the simulations we see that cooling for $\Delta_{pc} = 0, \Delta_{pa} > 0$ is predicted for a freely moving atom, see fig. 3.5. For a localised atom, the cooling region deviates from the $\Delta_{pc} = 0$ axis, following the dressed states, see fig. 3.6. This is a possible explanation for the fact that we could not observe stable coupling close to resonance.

Although heating and cooling processes in our system are probably more complex than described by the theory outlined above, due to the additional dipole potentials of the conveyor belt and the lock laser, the simulations indicate that cavity cooling should also be possible for $\Delta_{pa} < 0$. In the next section, I will present measurements that demonstrate this red-detuned cooling.

3.2.4 Demonstration of red-detuned cavity cooling

In the experiments presented in chapters 1 and 2, the probe laser was always tuned to resonance with the empty cavity, i.e. $\Delta_{pc} = 0$. For the experiments described in the following, the red-detuned probe laser ($\Delta_{pa} < 0$) is initially off-resonant, such that instead of a transmission drop, a rise in transmission is expected upon an atom transported into the cavity.

Figure 3.7 (a) shows the result of a measurement where the cavity-atom detuning was set to $\Delta_{ca} = -2\pi \times 94\,\mathrm{MHz}$ and the probe-cavity detuning to $\Delta_{pc} = -2\pi \times 1\,\mathrm{MHz}$. In the experimental sequence, firstly we set the probe-atom detuning Δ_{pa} to the desired cavity-atom detuning Δ_{ca} by choosing an appropriate setting of an AOM in the path of the probe laser. Secondly, the cavity is tuned into resonance with the probe laser ($\Delta_{pc} = 0$) by sweeping the lock laser frequency until maximum transmission is observed. On resonance, the empty-cavity transmission is set to a predetermined value. In fig. 3.7, this

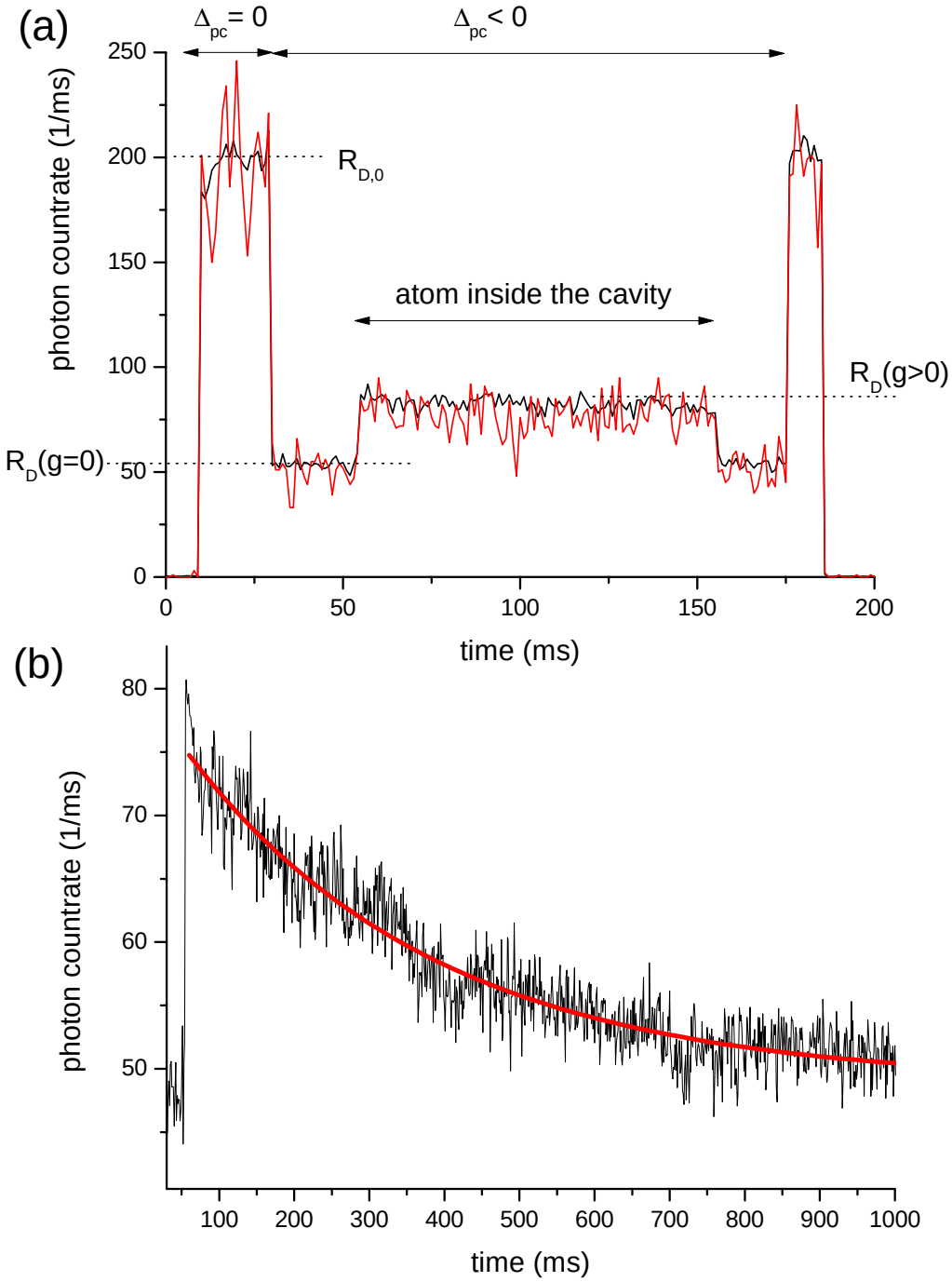

Figure 3.7: (a) Transmission signal for a single measurement (red curve) and averaged over 20 traces (black curve). (b) Longer observation to measure the lifetime, which is extracted from an exponential fit to be 330 ms. The detunings were set to $\Delta_{ca} = -2\pi \times 94\,\mathrm{MHz}$ and $\Delta_{pc} = -2\pi \times 1\,\mathrm{MHz}$. for both measurements.

count rate of $R_{\mathrm{D},0}\,(\Delta_{pc}=0)=200\,\mathrm{ms}^{-1}$ is observed for 20 ms. In a third step, the probe laser frequency is changed to $\Delta_{pc}/(2\pi)=-1\,\mathrm{MHz}$ at $t=30\,\mathrm{ms}$ while the cavity is still empty, causing the drop in transmission to $R_{\mathrm{D}}\,(g=0)$. In the trace presented here, $R_{\mathrm{D}}\,(g=0)\approx 55\,\mathrm{ms}^{-1}$. The transmission does not drop to zero because the detuning of 1 MHz is only slightly larger than the FWHM cavity-linewidth of 2κ. After measuring the empty cavity transmission for 25 ms, a single atom is inserted into the cavity. At that point in time, the transmission rises to $R_{\mathrm{D}}\,(g\neq 0)$.

The averaged transmission signal (black curve) is almost flat within the noise, which shows that no atoms are lost on this timescale. A strong repumper was applied during the whole sequence, so that a loss of atoms would be visible by a decreasing transmission for this settings. Measuring the transmission for one second and performing an ensemble average over many traces, see fig. 3.7 (b), yields a lifetime of (330 ± 10) ms from an exponential fit.

To measure the lineshift caused by the atom-cavity coupling, the same measurement, here again with the short observation time, was repeated for different probe-cavity detunings Δ_{pc}, see fig. 3.8 (a). For each detuning Δ_{pc}, the three count rates introduced above can be determined, yielding the normalised transmission levels

$$\bar{T}_0(\Delta_{pc})=\frac{R_{\mathrm{D}}\,(g=0)}{R_{\mathrm{D},0}}\ ,\ \bar{T}_g(\Delta_{pc})=\frac{R_{\mathrm{D}}\,(g\neq 0)}{R_{\mathrm{D},0}} \tag{3.16}$$

for the empty cavity and the case of a coupled atom, respectively.

A Lorentz-fit to $\bar{T}_0(\Delta_{pc})$ yields a frequency offset of 0.17 MHz and a HWHM linewidth of $\kappa'=0.49\,\mathrm{MHz}$. The frequency offset is probably due to a small error in the second step of the experimental sequence, at which the cavity is set to be resonant with the probe laser, i.e. we obtain $\Delta_{pc}\approx 0$, but not exactly. The discrepancy between the linewidth obtained from the fit and $\kappa=0.4\,\mathrm{MHz}$ is similar to an observation made by Igor Dotsenko [29], where the linewidth obtained by sweeping the cavity resonance and measuring the Lorentz profile was also larger than the result of the cavity ringdown measurement. The suggested explanation was that both the finite bandwidth of the probe laser and the limited relative frequency stability between cavity resonance and probe laser could cause this effect.

The lineshift, obtained by fitting the one-atom transmission data $\bar{T}_g(\Delta_{pc})$ with a Lorentz profile using the width κ', is $\Delta_s=2\pi\times 0.22\,\mathrm{MHz}$. For the two-level model and in the dispersive regime, the resonance shift is given by $\Delta_s=g^2/\Delta_{ca}$, cf. (1.35), which yields a coupling strength of $g=2\pi\times 4.5\,\mathrm{MHz}$ for $\Delta_{ca}=-2\pi\times 94\,\mathrm{MHz}$.

It is not yet understood why the coupling should be so low. Using data from a broader range of detunings would be beneficial, but it was not possible to

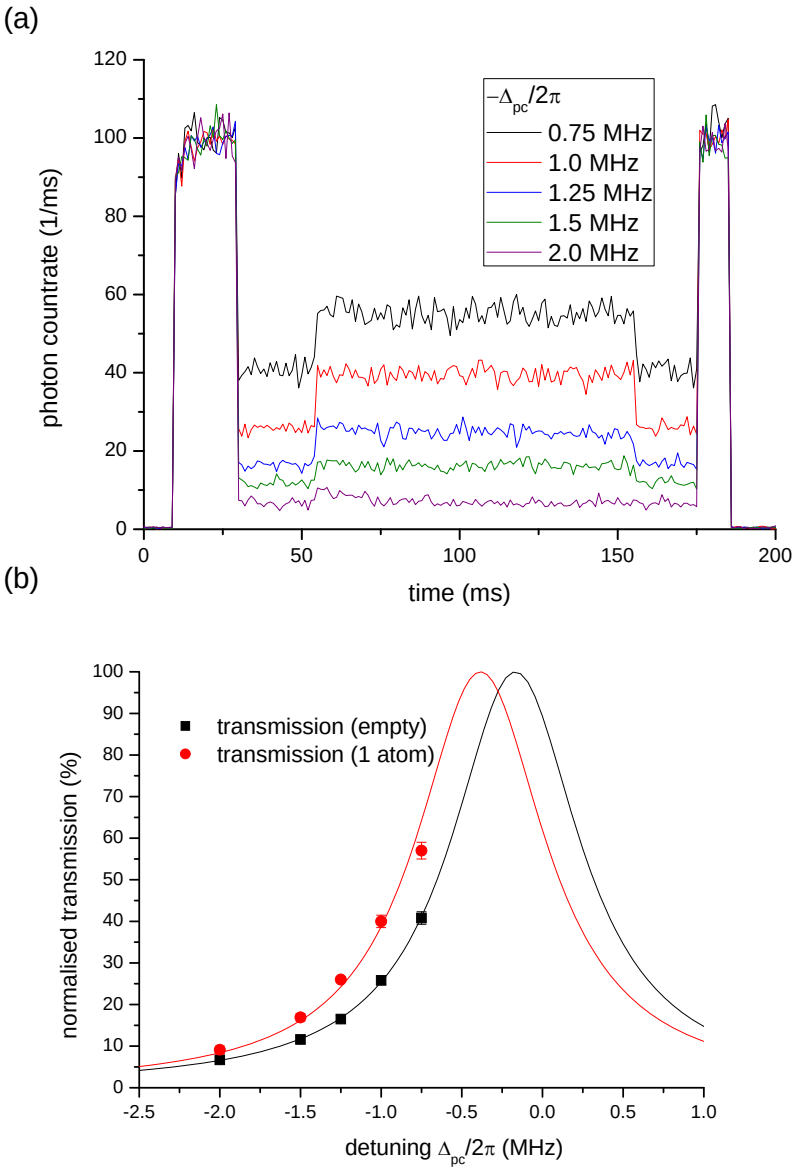

Figure 3.8: (a) Averaged transmission traces for a fixed cavity-atom detuning of $\Delta_{ca} = -2\pi \times 94\,\mathrm{MHz}$ and a varying probe-cavity detuning Δ_{pc}. (b) Normalised transmission levels for the empty cavity (black dots) and with one atom coupled to the cavity (red dots), extracted from the transmission levels in (a). The solid lines are fit results.

measure stable transmission signals closer to resonance, since the atoms were lost after a very short time. This is why we could not measure the complete transmission profile. This almost abrupt transition from cooling to heating is compatible with fig. 3.6, where the two regions of positive and negative friction are close together near the dressed states.

One possible explanation for the low value of g is that the two-level model is not appropriate to interpret the measured lineshift, because for $\Delta_{ca} = -94\,\mathrm{MHz}$ the influence of the $|F' = 4\rangle$ state should be taken into account. All detunings referred to are defined with respect to the $|F = 4\rangle \rightarrow |F' = 5\rangle$ transition, thus when the laser is *red-detuned* by $\approx 100\,\mathrm{MHz}$ from this transition, it is $\approx 150\,\mathrm{MHz}$ *blue-detuned* from $|F = 4\rangle \rightarrow |F' = 4\rangle$. The combined effect of two competing dispersive shifts acting in opposite directions could explain why the measured lineshift is lower than expected. For a theoretical investigation of this phenomenon, the master equation must be extended to contain multiple excited states [46, 47].

3.2.5 Conclusion

The numerical simulations discussed in this section provide a qualitative explanation for our observations, especially that stable coupling close to resonance could not be achieved. Future experiments on cavity cooling require a more extensive study of the underlying theory, including the influence of additional optical lattices and cooling mechanisms for two or more atoms coupled simultaneously to the cavity.

A conceptual problem remains with all cooling schemes for which the cavity is shifted *into* resonance. They can hardly be combined with the state-measurement technique described in chapter 2, because instead of causing a transmission drop, an atom coupled to the cavity increases the intracavity probe laser intensity, leading to a higher inelastic Raman scattering rate.

If it turns out that with the right setting of detunings the red-detuned and off-resonant cooling is preferable in terms of localising the atom to reach a higher g_{eff} , it would be necessary to alternatively switch between stages of cooling and performing the actual measurement, similar to procedures used by other research groups [81, 82]. In conjunction with measuring the vacuum-Rabi-splitting [15], we showed that with our existing setup it is indeed possible to change both detunings and keep the cavity stabilised within one experimental sequence.

Summarising, cavity-cooling provides an interesting perspective and is an important mechanism that we have already taken advantage of. For most planned experiments, a stable and high coupling strength g is vital, justifying further research in this direction.

4 Conclusion and Outlook

In this thesis I have investigated the internal state dynamics of one and two atoms coupled to a high-finesse cavity and have studied mechanisms to control the atomic motion. My findings show both the capabilities and the limits of the current setup, and they provide a basis to asses and plan future experiments and modifications of the experimental setup. In the following I address two issues currently imposing constraints on our experiment and present an extended measurement method allowing us to gain more information about the dynamics in our system.

4.1 Optical pumping and birefringent splitting

Because of the mirror birefringence, our cavity supports only linear polarisation, which has the effect that we cannot use the closed cycling transition $|F = 4, m_F = 4\rangle \rightarrow |F' = 5, m'_F = 5\rangle$. Instead, the atomic population is distributed over the whole ground state manifold. This is a disadvantage for our experiments in several ways:

First of all, instead of the theoretically achievable maximum coupling of $g_{4,4\rightarrow 5',5'} = 2\pi \times 18\,\mathrm{MHz}$ we expect an ideal maximum coupling strength of $2\pi \times 13.1\,\mathrm{MHz}$. In terms of the single atom cooperativity parameter C_1, this amounts almost to a factor of two. A high cooperativity is desirable because it is a universal figure of merit entering e.g. the fidelity of entanglement schemes.

Secondly, a distribution over all m_F states increases the complexity for theoretical considerations and experimental studies alike. In [27] it was calculated that the AC-Stark shift of the excited states is m_F dependent, therefore also the detunings Δ_{pa} and Δ_{ca}, which always refer to the Stark-shifted atomic resonance frequency, are m_F dependent. This effect can be neglected in the dispersive regime since the AC-Stark shift is only on the order of 10 to 20 MHz, but closer to resonance it means that the detuning varies on the timescale of redistribution over the m_F states.

Thirdly, one result of the numerical simulations is that, starting from equal populations, it takes a few ms until optical pumping by the probe laser leads to the steady state m_F distribution. Thus for the telegraph signals studied in chapter 2 a quantum jump from $|F = 4\rangle$ to $|F = 3\rangle$ can occur during this optical pumping process, followed by redistribution by virtue of photon scattering while

the atom is in $|F = 3\rangle$. A jump back to $|F = 4\rangle$ causes the process of probe-laser induced m_F redistribution to start again etc. Therefore also the effective coupling strength, even for a perfectly localised atom, is constantly changing during the observation of random telegraph signals. This effect could only be neglected if the average dwell time in $|F = 4\rangle$ would be much larger than the timescale of optical pumping.

Finally, for a perfectly circularly polarised probe laser inducing only σ_+ (or σ_-) transitions, inelastic Raman scattering to $|F = 3\rangle$, i.e. the state-changing effect of our measurement, would be strongly reduced. This means the projective QND measurement discussed in chapter 2 would be almost perfect. For measurements where elastic scattering is not an issue, the probe laser intensity or the integration time could be increased to a level where the signal to noise ratio is sufficient to distinguish 0, 1, and 2 atoms in $|F = 4\rangle$, before pumping to $|F = 3\rangle$ takes place.

All these considerations show that for a next generation of this cavity-QED experiment it would be very beneficial if birefringent splitting of the cavity resonance could be reduced to a negligible level. This could be possible by either engineering the process of mirror assembly such that the stress induced birefringent splitting $\Delta\omega_{br}$ is much smaller than for the current setup, or to use a more open configuration with a higher cavity linewidth $2\kappa \gg \Delta\omega_{br}$. For the latter case, obviously the coupling strength g has then also to be higher to still obtain a good cooperativity, which can be realised by a smaller mode volume. However, a shorter distance between the two mirrors is difficult to combine with the current experimental setup, because the high-power YAG laser beams traverse the cavity laterally and already now we observe heating of the glass substrates.

4.2 Controlling the coupling strength

The magnitude and variation of g is influenced by both the internal and external atomic degrees of freedom, since $g \propto d(m_F) \cdot E(\mathbf{r})$. Increasing $d(m_F)$ is possible by working with the strongest cycling transition as just discussed, whereas controlling $E(\mathbf{r})$ requires that the thermal motion of the atom is limited.

As reported in section 3.1.3, the intracavity dipole trap generated by a red-detuned lock laser gives rise to an improved coupling strength due to better three-dimensional confinement. In the configuration used here the lock laser was close to the atomic resonance, causing a high photon scattering rate. A further red-detuned off-resonant trap, either intracavity or from the side, superimposed with the existing conveyor belt, would allow us to benefit from the improved confinement while keeping the scattering rate low.

The model of thermal motion which I have applied to analyse the averaged transmission yields high temperatures of around 150 to 200 µK, compatible with

earlier estimates [14]. These values are upper limits since they subsume all other possible effects leading to a lower g. But to effectively localise the atom by a trapping potential of reasonable low depth, AC Stark shift, and scattering rate, the temperature has to be reduced. To this end heating of the atom by the lock laser must be minimised and effective cooling procedures should be applied.

Regarding the first point, much effort has already gone into improving the electronics of the control loop stabilising the cavity to the lock laser, so in terms of active stabilisation we have almost reached a limit. A better passive stability of the whole cavity setup would permit using a much lower lock laser power, but this is only feasible in conjunction with a major overhaul of the experiment.

In terms of cooling procedures, we already employ cavity cooling, which is evident by the long observation times, exceeding the lifetime of atoms subject to the lock laser alone. A theoretical investigation and numerical simulations based on a more complete picture than studied in section 3.2, taking additional optical lattices into account, could hint at more effective ways to exploit cavity cooling. Another approach is to use cavity-independent schemes like Raman sideband and molasses cooling [19, 60].

4.3 Photon click analysis of the spin dynamics

The analysis of two-atom telegraph signals demonstrate that it is possible to extract additional information about the spin dynamics by exploiting all available knowledge about the system and applying Bayesian statistics. For the results presented in this thesis, some information about the spin dynamics was hidden by the limited resolution of 1 ms given by the binning time. Using another data acquisition hardware it is possible to record a list of all individual photon arrival times. A modified version of the Bayesian algorithm discussed in section 2.3.3 could then be applied to this single-photon record, possibly yielding extended information about the dynamical processes in our system.

This hardware, a special timer card, was not used for the experiments presented in this thesis, but it has recently been implemented. Figure 4.1 (a) shows a trace of a one-atom telegraph signal with the usual binning time of 1 ms. The photon arrival times are plotted for a 10 ms window, where the quantum jump is clearly visible as a transition to a reduced density of lines. Currently the data is analysed after a whole series of traces is stored and the data acquisition is finished. Recording the photon clicks and streaming them “live” to some analysis software, it might become feasible to apply quantum feedback to steer the atom towards a desired state [83, 84].

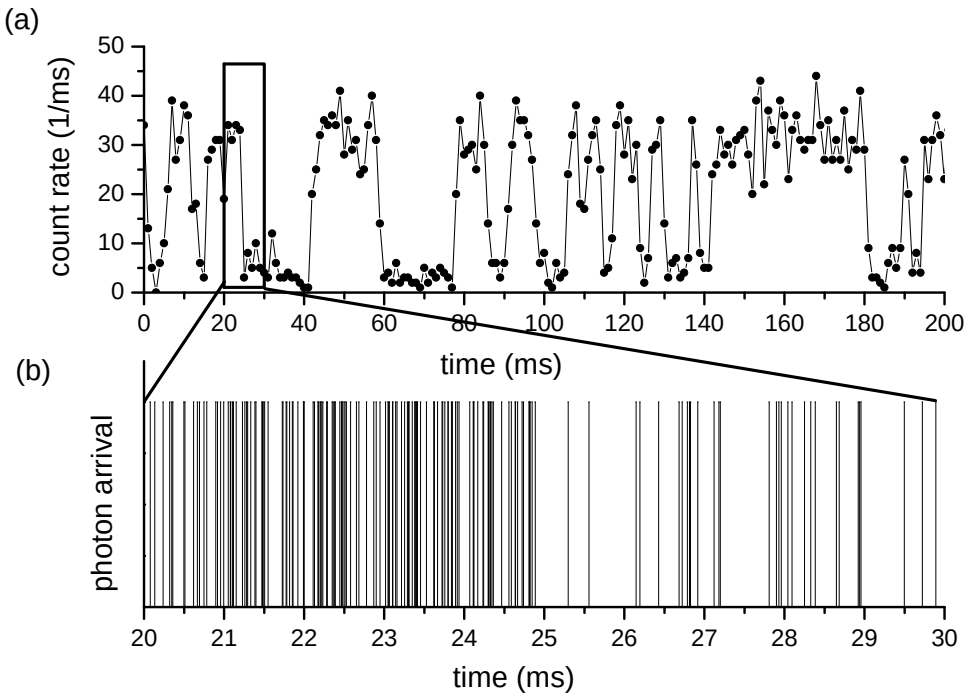

Figure 4.1: (a) Single-atom telegraph signal recorded with a resolution of 1 ms. (b) Photon arrival times of the same signal for a 10 ms window, exhibiting a quantum jump at $t \approx 24.9\,\mathrm{ms}$.

Bibliography

[1] E. T. Jaynes and F. W. Cummings, *Comparison of quantum and semiclassical radiation theories with application to the beam maser*, Proceedings of the IEEE **51**, 89 (1963)

[2] H. Carmichael, *An Open Systems Approach to Quantum Optics*, Springer, Berlin (1993)

[3] H. J. Metcalf and P. van der Straten, *Laser Cooling and Trapping*, Springer (1999)

[4] G. Raithel, C. Wagner, H. Walter, L. M. Narducci, and M. O. Scully, *The micromaser: Providing ground for quantum physics*, in P. Berman, ed., *Cavity Quantum Electrodynamics*, p. 57, Academic Press, New York (1994)

[5] J. M. Raimond, M. Brune, and S. Haroche, *Manipulating quantum entanglement with atoms and photons in a cavity*, Review of Modern Physics **73**, 565 (2001)

[6] R. Miller, T. E. Northup, K. M. Birnbaum, A. Boca, A. D. Boozer, and H. J. Kimble, *Trapped atoms in cavity QED: coupling quantized light and matter*, Journal of Physics B: Atomic, Molecular and Optical Physics **38**, S551 (2005)

[7] G. Rempe, R. J. Thompson, R. J. Brecha, W. D. Lee, and H. J. Kimble, *Optical Bistability and Photon Statistics in Cavity Quantum Electrodynamics*, Physical Review Letters **67**, 1727 (1991)

[8] R. J. Thompson, G. Rempe, and H. J. Kimble, *Observation of normal mode Splitting for an Atom in a Optical Cavity*, Physical Review Letters **68**, 1132 (1992)

[9] S. L. Mielke, G. T. Foster, and L. A. Orozco, *Nonclassical Intensity Correlations in Cavity QED*, Phys. Rev. Lett. **80**, 3948 (1998)

[10] C. J. Hood, M. S. Chapman, T.W. Lynn, and H. J. Kimble, *Real-Time Cavity QED with Single Atoms*, Physical Review Letters **80**, 4157 (1998)

[11] P. Münstermann, T. Fischer, P. W. H. Pinkse, and G. Rempe, *Single slow atoms from an atomic fountain observed in a high-finesse optical cavity*, Opt. Commun. **159**, 63 (1999)

[12] S. Nußmann, M. Hijlkema, B. Weber, F. Rohde, G. Rempe, and A. Kuhn, *Submicron Positioning of Single Atoms in a Microcavity*, Physical Review Letters **95**, 173602 (2005)

[13] J. A. Sauer, K. M. Fortier, M. S. Chang, C. D. Hamley, and M. S. Chapman, *Cavity QED with optically transported atoms*, Physical Review A **69**, 051804 (2004)

[14] M. Khudaverdyan, W. Alt, I. Dotsenko, T. Kampschulte, K. Lenhard, A. Rauschenbeutel, S. Reick, K. Schörner, A. Widera, and D. Meschede, *Controlled insertion and retrieval of atoms coupled to a high-finesse optical resonator*, New Journal of Physics **10**, 073023 (2008)

[15] Mkrtych Khudaverdyan, *A controlled one and two atom-cavity system*, Ph.D. thesis, Institute for Applied Physics, University of Bonn (2009), available at `http://hss.ulb.uni-bonn.de/diss_online/`

[16] Anders S. Sørensen and Klaus Mølmer, *Probabilistic Generation of Entanglement in Optical Cavities*, Physical Review Letters **90**, 127903 (2003)

[17] Anders S. Sørensen and Klaus Mølmer, *Measurement Induced Entanglement and Quantum Computation with Atoms in Optical Cavities*, Physical Review Letters **91**, 097905 (2003)

[18] L. You, X. X. Yi, and X. H. Su, *Quantum logic between atoms inside a high-Q optical cavity*, Physical Review A **67**, 032308 (2003)

[19] A. D. Boozer, A. Boca, R. Miller, T. E. Northup, and H. J. Kimble, *Cooling to the Ground State of Axial Motion for One Atom Strongly Coupled to an Optical Cavity*, Physical Review Letters **97**, 083602 (2006)

[20] J. C. Berquist, Randall G. Hulet, W. Itano, and D. J. Wineland, *Observation of Quantum Jumps in a Single Atom*, Physical Review Letters **57**, 1669 (1986)

[21] Th. Sauter, W. Neuhauser, R. Blatt, and P. E. Toschek, *Observation of Quantum Jumps*, Physical Review Letters **57**, 1696 (1986)

[22] Warren Nagourney, Jon Sandberg, and Hans Dehmelt, *Shelved Optical Electron Amplifier: Observation of Quantum Jumps*, Physical Review Letters **56**, 2797 (1986)

[23] J. Ye, D. W. Vernooy, and H. J. Kimble, *Trapping of Single Atoms in Cavity QED*, Physical Review Letters **83**, 4987 (1999)

[24] Gerald Hechenblaikner, Markus Gangl, Peter Horak, and Helmut Ritsch, *Cooling an atom in a weakly driven high-Q cavity*, Physical Review A **58**, 3030 (1998)

[25] Stefan Kuhr, *A controlled quantum system of individual neutral atoms*, Ph.D. thesis, Institute for Applied Physics, University of Bonn (2003), available at `http://hss.ulb.uni-bonn.de/diss_online/`

[26] Wolfgang Alt, *Optical Control of Single Neutral Atoms*, Ph.D. thesis, Institute for Applied Physics, University of Bonn (2004), available at `http://hss.ulb.uni-bonn.de/diss_online/`

[27] Dominik Schrader, *A Neutral Atom Quantum Register*, Ph.D. thesis, Institute for Applied Physics, University of Bonn (2004), available at `http://hss.ulb.uni-bonn.de/diss_online/`

[28] Yevhen Miroshnychenko, *An atom-sorting machine*, Ph.D. thesis, Institute for Applied Physics, University of Bonn (2006), available at `http://hss.ulb.uni-bonn.de/diss_online/`

[29] Igor Dotsenko, *Single atoms on demand for cavity QED experiments*, Ph.D. thesis, Institute for Applied Physics, University of Bonn (2007), available at `http://hss.ulb.uni-bonn.de/diss_online/`

[30] Alexander Thobe, *Quantum Jumps of One and Two Atoms in a Strongly Coupled Atom-Cavity System*, Diplomarbeit, Institute for Applied Physics, University of Bonn (2009), available at `http://agmeschede.iap.uni-bonn.de/`

[31] L. Förster, W. Alt, I. Dotsenko, M. Khudaverdyan, D. Meschede, Y. Miroshnychenko, S. Reick, and A. Rauschenbeutel, *Number-triggered loading and collisional redistribution of neutral atoms in a standing wave dipole trap*, New J. Phys. **8**, 259 (2006)

[32] R. Grimm, M. Weidemüller, and Y. B. Ovchinnikov, *Optical dipole traps for neutral atoms*, Advances in Atomic, Molecular, and Optical Physics **42**, 95 (2000)

[33] S. Kuhr, W. Alt, D. Schrader, M. Müller, V. Gomer, and D. Meschede, *Deterministic delivery of a single atom*, Science **293**, 278 (2001)

[34] I. Dotsenko, W. Alt, M. Khudaverdyan, S. Kuhr, D. Meschede, Y. Miroshnychenko, D. Schrader, and A. Rauschenbeutel, *Submicrometer position control of single trapped neutral atoms*, Physical Review Letters **95**, 033002 (2005)

[35] S. Haroche and J.-M. Raimond, *Exploring the Quantum*, Oxford University Press (2006)

[36] Christina J. Hood and H. J. Kimble, *Characterization of high-finesse mirrors: Loss, phase shifts, and mode structure in an optical cavity*, Physical Review A **64**, 033804 (2001)

[37] P. R. Berman, ed., *Cavity Quantum Electrodynamics*, Advances in Atomic, Molecular, and Optical Physics, Academic Press, San Diego (1994)

[38] M. O. Scully and M. S. Zubairy, *Quantum Optics*, Cambridge University Press, Cambridge (1997)

[39] P. Meystre and M. Sargent, *Elements of Quantum Optics*, Springer (1990)

[40] R. W. P. Drever, J. L. Hall, F. V. Kowalski, J. Hough, G. M. Ford, A. J. Munley, and H. Ward, *Laser phase and frequency stabilization using an optical resonator*, Applied Physics B: Lasers and Optics **31**, 97 (1983)

[41] Bo Gao, *Effects of Zeeman degeneracy on the steady-state properties of an atom interacting with a near-resonant laser field: Analytic results*, Physical Review A **48**, 2443 (1993)

[42] Bo Gao, *Effects of Zeeman degeneracy on the steady-state properties of an atom interacting with a near-resonant laser field: Probe spectra*, Physical Review A **49**, 3391 (1994)

[43] Bo Gao, *Effects of Zeeman degeneracy on the steady-state properties of an atom interacting with a near-resonant laser field: Resonance fluorescence*, Physical Review A **50**, 4139 (1994)

[44] A. R. Edmonds, *Angular momentum in quantum mechanics*, Princeton University Press, Princeton, 3rd edition (1974)

[45] Sze M. Tan, *A computational toolbox for quantum and atomic optics*, Journal of Optics B: Quantum and Semiclassical Optics **1**, 424 (1999)

[46] Kevin M. Birnbaum, *Cavity QED with Multilevel Atoms*, Ph.D. thesis, California Institute of Technology, Pasadena, California (2005), available at `http://etd.caltech.edu`

[47] K. M. Birnbaum, A. S. Parkins, and H. J. Kimble, *Cavity QED with multiple hyperfine levels*, Physical Review A **74**, 063802 (2006)

[48] Vladimir B. Braginsky, Yuri I. Vorontsov, and Kip S. Thorne, *Quantum Nondemolition Measurements*, Science **209**, 547 (1980)

[49] Souma Chaudhury, Greg A. Smith, Kevin Schulz, and Poul S. Jessen, *Continuous Nondemolition Measurement of the Cs Clock Transition Pseudospin*, Physical Review Letters **96**, 043001 (2006)

[50] P. J. Windpassinger, D. Oblak, P. G. Petrov, M. Kubasik, M. Saffman, C. L. Garrido Alzar, J. Appel, J. H. Müller, N. Jærgaard, and E. S. Polzik, *Nondestructive Probing of Rabi Oscillations on the Cesium Clock Transition near the Standard Quantum Limit*, Physical Review Letters **100**, 103601 (2008)

[51] R. Loudon, *The Quantum Theory of Light*, Clarendon, Oxford (1983)

[52] R. Ozeri, C. Langer, J.D. Jost, B. DeMarco, A. Ben-Kish, B. R. Blakestad, J. Britton, J. Chiaverini, W. M. Itano, D. B. Hume, D. Leibfried, T. Rosenband, P. O. Schmidt, and D. J. Wineland, *Hyperfine Coherence in the Presence of Spontaneous Photon Scattering*, Physical Review Letters **95**, 030403 (2005)

[53] R. A. Cline, J. D. Miller, M. R. Matthews, and D .J. Heinzen, *Spin relaxation of optically trapped atoms by light scattering*, Optics Letters **19**, 207 (1994)

[54] D. A. Steck, *Cesium D Line Data* (23 January 1998, Revision 1.5, 21 November 2002), `http://steck.us/alkalidata/`

[55] D. Schrader, I. Dotsenko, M. Khudaverdyan, Y. Miroshnychenko, A. Rauschenbeutel, and D. Meschede, *Neutral atom quantum register*, Physical Review Letters **93**, 150501 (2004)

[56] Richard J. Cook and H. J. Kimble, *Possibility of Direct Observation of Quantum Jumps*, Physical Review Letters **54**, 1023 (1985)

[57] Wayne M. Itano, J.C. Berquist, Randall G. Hulet, and D.J. Wineland, *Radiative Decay Rates in Hg^+ from Observations of Quantum Jumps in a Single Ion*, Physical Review Letters **59**, 2732 (1987)

[58] Sebastien Gleyzes, Stefan Kuhr, Christine Guerlin, Julien Bernu, Samuel Deleglise, Ulrich Busk Hoff, Michel Brune, Jean-Michel Raimond, and Serge

Haroche, *Quantum jumps of light recording the birth and death of a photon in a cavity*, Nature **446**, 297 (2007)

[59] M. Khudaverdyan, W. Alt, T. Kampschulte, S. Reick, A. Thobe, A. Widera, and D. Meschede, *Quantum Jumps and Spin Dynamics of Interacting Atoms in a Strongly Coupled Atom-Cavity System*, Physical Review Letters **103**, 123006 (2009)

[60] J. McKeever, J. R. Buck, A. D. Boozer, A. Kuzmich, H.-C. Nägerl, D.M. Stamper-Kurn, and H. J. Kimble, *State-Insensitive Cooling and Trapping of Single Atoms in an Optical Cavity*, Physical Review Letters **90**, 133602 (2003)

[61] P. W. H. Pinkse, T. Fischer, P. Maunz, and G. Rempe, *Trapping an atom with single photons*, Nature **404**, 365 (2000)

[62] A. C. Doherty, A. S. Parkins, S. M. Tan, and D. F. Walls, *Motion of a two-level atom in an optical cavity*, Physical Review A **56**, 833 (1997)

[63] P. Horak, G. Hechenblaikner, K. M. Gheri, H. Stecher, and H. Ritsch, *Cavity-Induced Atom Cooling in the Strong Coupling Regime*, Physical Review Letters **79**, 4974 (1997)

[64] Peter Domokos, Peter Horak, and Helmut Ritsch, *Semiclassical theory of cavity-assisted atom cooling*, J. Phys. B: At. Mol. Opt. Phys. **34**, 187 (2001)

[65] Peter Domokos and Helmut Ritsch, *Mechanical effects of light in optical resonators*, J. Opt. Soc. Am. B **20**, 1098 (2003)

[66] Karim Murr, *On the suppression of the diffusion and the quantum nature of a cavity mode. Optical bistability: forces and friction in driven cavities*, J. Phys. B: At. Mol. Opt. Phys. **36**, 2515 (2003)

[67] Peter Domokos, Andras Vukics, and Helmut Ritsch, *Anomalous Doppler-Effect and Polariton-Mediated Cooling of Two-Level Atoms*, Physical Review Letters **92**, 103601 (2004)

[68] P. Maunz, T. Puppe, I. Schuster, N. Syassen, P. W. H. Pinkse, and G. Rempe, *Cavity cooling of a single atom*, Nature **428**, 50 (2004)

[69] Peter Maunz, *Cavity cooling and spectroscopy of a bound atom-cavity system*, Ph.D. thesis, Technische Universität München, Max-Planck-Institut für Quantenoptik (2005)

[70] S. J. van Enk, J. McKeever, H. J. Kimble, and J. Ye, *Cooling of a single atom in an optical trap inside a resonator*, Physical Review A **64**, 013407 (2001)

[71] Vladan Vuletic, Hilton W. Chan, and Adam T. Black, *Three-dimensional cavity Doppler cooling and cavity sideband cooling by coherent scattering*, Physical Review A **64**, 033405 (2001)

[72] Stefano Zippilli and Giovanna Morigi, *Cooling Trapped Atoms in Optical Resonators*, Physical Review Letters **95**, 143001 (2005)

[73] Stefano Zippilli and Giovanna Morigi, *Mechanical effects of optical resonators on driven trapped atoms: Ground-state cooling in a high-finesse cavity*, Physical Review A **72**, 053408 (2005)

[74] A. Griessner, D. Jaksch, and P. Zoller, *Cavity-assisted nondestructive laser cooling of atomic qubits*, J. Phys. B: At. Mol. Opt. Phys. **37**, 1419 (2004)

[75] K. Murr, P. Maunz, P. W. H. Pinkse, T. Puppe, I. Schuster, D. Vitali, and G. Rempe, *Momentum diffusion for coupled atom-cavity oscillators*, Physical Review A **74**, 043412 (2006)

[76] S. Nußmann, K. Murr, M. Hijlkema, B. Weber, A. Kuhn, and G. Rempe, *Vacuum-stimulated cooling of single atoms in three dimensions*, Nature Physics **1**, 122 (2005)

[77] K. Murr, S. Nußmann, T. Puppe, M. Hijlkema, B. Weber, S. C. Webster, A. Kuhn, and G. Rempe, *Three-dimensional cavity cooling and trapping in an optical lattice*, Physical Review A **73**, 063415 (2006)

[78] T. Fischer, P. Maunz, T. Puppe, P. W. H Pinkse, and G. Rempe, *Collective light forces on atoms in a high-finesse cavity*, New Journal of Physics **3**, 11 (2001)

[79] Peter Horak and Helmut Ritsch, *Scaling properties of cavity-enhanced atom cooling*, Physical Review A **64**, 033422 (2001)

[80] András Vukics, Christoph Maschler, and Helmut Ritsch, *Microscopic physics of quantum self-organization of optical lattices in cavities*, New Journal of Physics **9**, 255 (2007)

[81] A. Boca, R. Miller, K. M. Birnbaum, A. D. Boozer, J. McKeever, and H. J. Kimble, *Observation of theVacuum Rabi Spectrum for One Trapped Atom*, Physical Review Letters **93**, 233603 (2004)

[82] P. Maunz, T. Puppe, I. Schuster, N. Syassen, P. W. H. Pinkse, and G. Rempe, *Normal-Mode Spectroscopy of a Single-Bound-Atom-Cavity System*, Physical Review Letters **94**, 033022 (2005)

[83] A. R. R. Carvalho and J. J. Hope, *Stabilizing entanglement by quantum-jump-based feedback*, Physical Review A **76**, 010301 (2007)

[84] A. R. R. Carvalho, A. J. S. Reid, and J. J. Hope, *Controlling entanglement by direct quantum feedback*, Physical Review A **78**, 012334 (2008)